Paragenesis and geochemistry of the Miocene Milestone sinter, Silver City District, ID: Implications for sinter-hosted epithermal Au-Ag deposits

by

Emily Ruth Fenner

B.S., State University of New York College at Oswego, 2018

A THESIS

submitted in partial fulfillment of the requirements for the degree

MASTER OF SCIENCE

Department of Geology
College of Arts and Sciences

KANSAS STATE UNIVERSITY
Manhattan, Kansas

2020

Approved by:

Major Professor
Matthew Brueseke

Abstract

The Milestone sinter is a mid-Miocene epithermal paleosurface that is spatially associated with the DeLamar silver-gold deposit in the Silver City District, Idaho. The exact connection between Milestone and DeLamar, along with other deposits across the northern Great Basin, remains unknown. Additionally, the economic potential of Milestone has not been evaluated since Barrett (1985), where it was found to host Au and Ag. Geologic mapping of the Main Knob of Milestone reveals five lithofacies in the paleosurface: Matrix-supported breccia, clast-supported breccia, sinter, geyserite, and bioformations. The facies are indicative of a paleohotspring, typical of modern hot spring environments. Reflective light imagery and traditional microscopy show multiple quartz textures, electrum microparticles, pyrite relicts, and pyragyrite crystals. LA-ICP-MS data of trace elements show up to 2.84 wt % Ag and 153 ppm Au in sinter samples. The occurrence of precious metals in the sinter may be indicative of metal-rich veins at depth. Across the flow path from vent to distal apron, there is no relationship between precious metal deposition and flow path location (i.e. temperature variations). The fluids of the epithermal system took advantage of the faults and other structural weaknesses in the Silver City District much modern systems in Yellowstone National Park and the Taupo Volcanic Zone. The underlying Silver City rhyolite has an age of about 16.1 Ma (Brueseke and Hames, unpublished), and the mineralized veins in other Silver City District locations (e.g. War Eagle Mountain, Florida Mountain) have ages of ~15.5 to 15.8 Ma (Aseto, 2012; Mason et al., 2015). It is likely that Milestone formed in the same ~15.5 to 15.8 Ma age time interval.

Table of Contents

List of Figures

List of Tables

Acknowledgements

The author would like to thank the University of Arkansas for allowing us to use their lab to analyze our samples using LA-ICP-MS. I would also like to thank the Topeka Gem and Mineral Society, the Geological Society of America, and the Society of Economic Geologists for funding this project.

Dedication

This thesis is dedicated to my family who supported me through this entire journey from afar. Without their encouragement and patience, I would not be where I am today.

Chapter 1 - Introduction and Background

Sinter deposits are the surficial expression of epithermal ore-forming systems where superheated fluids (~150-300°C) and vapors rise through the earth's crust and discharge at the surface. Silica, along with other minerals and mineraloids, are precipitated out of solution upon cooling, and can form deposits up to tens of meters thick (Bonnichsen, 1983; Fournier, 1989; Guido and Campbell, 2011; Lynne, 2012). Siliceous sinters form above or adjacent to epithermal Au-Ag deposits and can therefore be an indicator of an economic deposit at depth. Recent studies, such as Vikre (2007), have focused on the presence of economic minerals and metal(loid)s in sinters that form in low sulfidation Au-Ag epithermal deposits. These studies confirmed the presence of ore minerals (e.g., selenides, sulfides, tellurides, Ag-Au minerals, etc.) in sinter and associated epithermal veins through crystallization and/or transport and deposition of nanoparticles (Saunders et al., 2015). Furthermore, Saunders and Brueseke (2012) also concluded that the degassing and devolatilization of fertile mantle greatly contributes to the formation of economic ores in epithermal systems, much like those in the Silver City District where the Milestone paleosurface is located.

The Miocene Silver City District (SCD) in the Owyhee Mountains in southwestern Idaho is considered the "birthplace" for modern ideas of epithermal precious metal deposits (Lindgren, 1900). The SCD hosts three primary epithermal Au-Ag deposits: Florida Mountain, War Eagle Mountain, and DeLamar, where ~16-15.5 Ma ores are hosted in quartz-adularia-dominated veins or disseminated through porous rhyolite lavas (Fig. 1). Milestone, the focus of this study, may be another epithermal deposit in the SCD. It is a hot spring sinter paleosurface and associated breccia deposit located ~1.2 km northwest of the DeLamar Silver Mine, in a northwest-trending fault zone associated with other mineral prospects (Fig. 1). The goal of this study is to provide geological constraints on how the Milestone deposit formed to assess whether the Milestone sinter is ore-bearing, and document the concentrations of trace elements (including Au and Ag), across the different sinter beds within the deposit.

This study presents new evidence for the economic potential of sinters and is a case study in how a small hydrothermal system can form and preserve depositional facies. We examine the preserved textures, mineralogy, and in-situ sinter elemental concentrations of the Milestone "Main Knob". These data are used to reconstruct the paleoenvironment of its formation, and assess the hot spring's role as a fluid pathway for trace metal(loid)/element mineralization in the Silver City District.

Background

Geothermal systems that result in hydrothermal surface features and epithermal mineralization are typically characterized by alkali chloride waters that are relatively reduced and have a neutral pH (Sillitoe, 2015). These are sites that have a high convective heat energy that is dissipated into fluids which discharge at the surface, creating a variety of depositional products. Such features are preserved in precious metal deposits, including sinter (Sillitoe, 2015). A magmatic component is commonly associated with such systems, but the compositional nature and physical dimensions of any associated magmatic body are debated across different epithermal deposits. Ratios of magmatic influence to hydrothermal influence vary with each system (Taylor, 1979; Norton, 1982; John, 2001; Saunders et al., 2008; Saunders et al., 2014). Tectonic settings also play a role in the development of epithermal deposits both in content and structural control by normal faults.

Epithermal deposits are commonly divided into three end-member types based on their mineralogical characteristics and alteration facies: high sulfidation (HS), intermediate-sulfidation, and low sulfidation (LS). HS environments contain 10-80% sulfides by volume, including minerals such as alunite, enargite, luzonite, and famatinite, and have metal(loid) signatures of Au-Ag-Cu±Te±Bi; other minerals such as quartz and barite may be common. LS environments are 1-5% sulfides by volume, contain minerals such as quartz, adularia, chalcedony, pyrrhotite, arsenopyrite, and high-Fe sphalerite, and metal(loid) signatures of Au±Ag±Se±Te±Hg±Cu (Sillitoe, 2015). Low sulfidation environments are most commonly associated with rift and/or hotspot settings, which are usually characterized by compositionally bimodal, basalt-rhyolite volcanism (Richards, 2009; Sillitoe, 2015) and are also found in volcanic arcs, associated with porphyry deposits at depth. Magmatic fluids are a primary source of several components in hydrothermal ore deposits in volcanic environments, such as metals, ligands, and vapors (Hedenquist and Lowenstern, 1994; John, 2001; Kamenov, 2007). The metal(loid)s and other ligands become concentrated in vapor and hypersaline fluids from various sources (e.g., subducted oceanic crust, leaching of country rock, partial melting of the asthenospheric wedge above a slab, partial melting of lithospheric mantle, etc.; Richards, 2009). The flux of metals measured from a volcano holds evidence that degassing magmas can exsolve metals to create an ore deposit given enough time and mechanisms to concentrate the metals (Hedenquist and Lowenstern, 1994). William-Jones and Heinrich (2005) suggested that significant amounts of ore metals and sulfur can be transported by low-density magmatic fluids via vapor-phase transport from a deeper magmatic setting to a shallow epithermal system. Transportation of minerals and metal(loid)s through epithermal fluids results in the aggregation and deposition of colloids (or nanoparticles) by boiling and can form high-grade ores, as is shown in detailed textural studies of bonanza epithermal ores (Saunders 1990, 1994; Saunders et al., 2011b, 2012, 2019).

A variety of tectonic settings that have been found to host LS environments have provided structural pathways for rising fluids by rifting (Sillitoe and Hedenquist, 2003). Rifting could occur in intra-, near-, and back-arc settings, postarc settings, and postcollisional settings (Sillitoe and Hedenquist, 2003). In the case of Milestone, postcollisional rifting allowed for bimodal rhyolite-basalt volcanism and hot spring development (Bonnichsen, 1983; Brueseke, 2010). Structural control often comes from localized faults due to such rifting. Commonly, rift basins with normal fault systems or fault-bounded caldera margins provide increased permeability in basement rocks that allow hydrothermal fluids to easily rise through the crust (Rowland and Sibson, 2001; John, 2003; Rowland and Simmons, 2005). Multiple locations with such tectonic controls are centers for hydrothermal activity and epithermal deposits. Notable present-day active locations include Yellowstone National Park (Hames et al., 2009) and the Taupo Volcanic Zone in New Zealand (Rowland and Simmons, 2005).

Paleosurface features are the result of fluids from an epithermal system interacting with surface landforms. These fluids also create hydrothermal alteration zones near the water table (Sillitoe, 2015). These features occur above underlying fracture systems which can, in some cases, host economically significant mineralization in the form of a LS epithermal deposit. Paleosurface features, including sinters and hydrothermal breccias, can thus be used to locate underling mineral resources (Nelson, 1988; Chang et al., 2011; Lynne, 2012; Hamilton et al., 2016). The breccias can be interbedded with sinter, as is the case for Milestone (Barrett, 1985). Hydrothermal systems carry trace metal(loid)s via fluid or vapor-phase transport up to the surface, where they can be discharged along with the silica-supersaturated fluid. As the fluid cools and silica precipitates upon boiling, the metal(loid)s precipitate and are deposited in the silica. As a result, if boiling occurs at the surface, paleosurfaces have the potential to be another economic resource. In sinters, the multicolored laminations have the potential to hold different amounts of metal(loid)s that could represent changes in fluid composition and/or temperature (Vikre, 2007).

Features commonly found in preserved paleosurfaces include bedded sinter (sometimes recrystallized into chalcedony), irregular/lenticular cavities (bubble-mat texture), geyserite (specular, nodular, columnar), silicified plant material, and hydrothermal breccia (Lynne, 2012; Sillitoe 2015; Hamilton et al., 2019). Better preserved paleosurfaces can be distinguished as having formed in different depositional environments based on their proximity to the hot spring vent (Hamilton et al., 2019). The features found in low-sulfidation epithermal deposits with paleosurfaces depend on the temperature of formation and their locations relative to the vent. From the vent, there is the proximal slope, mid-slope apron, distal slope/apron, and a marsh. The association of paleosurface features with their respective formation temperatures and slope location is depicted in Figure 1.1. The temperatures these features form from range from ~100° C at the vent, to the distal and marsh-type areas, which occur further away under temperatures below 35° C, also known as ambient temperatures (Fig. 1.1) (Sillitoe, 2015; Hamilton et al., 2019). Distinctive textures are unique to these different environments, yet are consistent across modern sinters and paleo-deposits (e.g., Belhadi et al., 2002; Vikre, 2007; Lynne, 2012, 2013; Sillitoe, 2015).

Geologic Setting

The geology of the Owyhee Mountains has been described and summarized by Lindgren and Drake (1904), Piper and Laney (1926), Asher (1968), Ekren et al. (1981), Ekren et al. (1982), Bonnichsen (1983), Halsor et al. (1988), Hasten (2012), and Mason et al. (2015). Prior to 19 Ma, magmatic activity was dominated by Cretaceous to Oligocene calc-alkaline volcanism due to subduction of the Farallon plate. At ~17 Ma, regionally, volcanism became primarily compositionally bimodal (Fig. 1.2), with the eruption of regional flood basalt volcanism (e.g., Columbia River Basalt group; Steens Basalt in the Oregon Plateau study area) and coeval rhyolite centers (John, 2001; Camp and Ross, 2004; Brueseke et al., 2007; Brueseke at al., 2008; Streck, 2014). This phase of magmatism lasted for ~3 myr and also coincided both spatially and temporally with [1] extensional tectonism that was primarily focused in the northern Nevada rift and Oregon-Idaho graben (Brueseke and Hart, 2008); and [2] deposition of abundant epithermal Au-Ag mineralization in locations such as National, Midas, Sleeper, Buckskin-National, and DeLamar (Saunders, 1994; John, 2001; John et al., 2003; Hames et al., 2009; Brueseke, 2010; Saunders et al, 2010; Saunders et al, 2013) (Fig. 1.2).

The SCD extends from War Eagle Mountain and Florida Mountain in the east to the DeLamar in the west. The DeLamar deposit itself is slightly < 5 km-wide and the Milestone sinter lies just to the north (Figs. 1.2, 1.3). The SCD was a mid-Miocene eruptive center and contains locally erupted mid-Miocene flood basalts, andesite-dacite lavas, rhyolite lavas, rhyolite tuffs, and abundant domes/eruptive loci (Fig. 1.2; Halsor et al., 1988; Hasten, 2012; Hasten et al., 2012). These Miocene volcanic units stratigraphically overlie Eocene-Oligocene volcanics and basement composed of Cretaceous granitoid rocks (e.g., Silver City batholith, which is an extension of the Idaho batholith) and Triassic metasedimentary strata (Pansze, 1975; Norman and Leeman, 1989;

Hasten, 2012). In the vicinity of the DeLamar mine and the Milestone deposit, the Miocene stratigraphic sequence consists of overlapping porphyritic and banded rhyolite lavas and domes that overlie rhyolite pyroclastic deposits and an older mafic-intermediate lava package (Barrett, 1985; Hasten, 2012). In the vicinity of Milestone, northwest trending normal faults apparently focused rhyolite eruptions, dome emplacement, fluid flow, and mineralization (Halsor et al., 1988; Hasten, 2012). Saunders et al. (2015) report Cu isotope data from electrum, chalcopyrite, and naumannite in Miocene northern Great Basin epithermal ores, including some data from the SCD. These data, along with Pb isotope studies of SCD ores (Aseto, 2012; Mason, 2015), demonstrate that the ores were likely derived from spatially and temporally associated mafic magmas, thus reflecting a mantle origin for the metal(loid)s.

In the northwest SCD, sinter, low-sulfidation mineralization, and rhyolite domes are located along a series of northwest-trending normal faults (Fig. 1.2). The tectonism responsible was active in the Early to Middle Miocene (Pansze, 1975). Several rhyolite domes, basalt dikes, and mineralized veins are localized along the fault zone (Asher, 1968; Pansze, 1975; Hasten, 2012). Argillic alteration is present along mineralized zones within the host rock (Asher, 1968; Pansze, 1975; Bonnichsen 1983; Barret, 1985). Epithermal deposits such as Milestone, DeLamar, Lucky Day, Twin Peaks, and Georgiana occur along these faults (Fig. 1.2) and most of the mineralization occurs in veins, based on reconnaissance exploration drilling (Gustin et al., 2019).

The Milestone deposit is referred to as a “fossil” geothermal system as it has characteristics of an hot spring, such as mineralized breccia and overlying sinter, and is comparable to other active geothermal systems in Nevada and New Zealand (Barrett, 1985) and at Yellowstone. The paleosurface at Milestone is characterized by its mineralized breccia and overlying hot spring layered sinter (Fig. 1.4). Lindgren (1900) was the first to briefly describe the primary Milestone sinter deposit (hereafter named the “Main Knob”) as a “spring deposit” with grayish to brownish quartz. Reconnaissance samples of bulk sinter show Au and Ag grades of 7.09 g/ton Ag and 2.83 g/ton Au (Barrett, 1985), which at the time of sampling, was not considered to be economical. This is in contrast to SCD veins and rhyolite-hosted Au-Ag grades that range from 0-40 g Au/ton and 0-1325.0 g Ag/ton (Gustin et al., 2019). Barrett (1985) broadly mapped the Milestone deposit and created cross-sections of the geology and subsurface alteration from core logs, in an effort to provide more detail on the geological setting and mineralogy of the deposit. Barrett (1985) reported minor argillic hydrothermal alteration (traces of cacoxenite, hematite, and silicification) in the country rock hypogene zone, as well as hypogene ore-minerals (naummanite, pyrargyrite, tetrahedrite, and possible micron-sized native gold), and gangue minerals (e.g., kaolinite, pyrite, jarosite, cocoxenite, illite, marcasite, and quartz).

This study aims to recharacterize the Milestone deposit using geological mapping; new microscopy; and in-situ, microanalytical trace element analysis by laser ablation-inductively couple plasma-mass spectrometer (LA-ICP-MS). Additionally, we aim to connect the site to other deposits in the SCD and analogous present-day hot springs in regard to location, mineralogy, and known surface features. We provide detailed facies descriptions and LA-ICP-MS analysis on minerals and trace metal(loid)s of the Main Knob sinter at Milestone and link the identified facies and geometry to record the history of the paleo-hot spring.

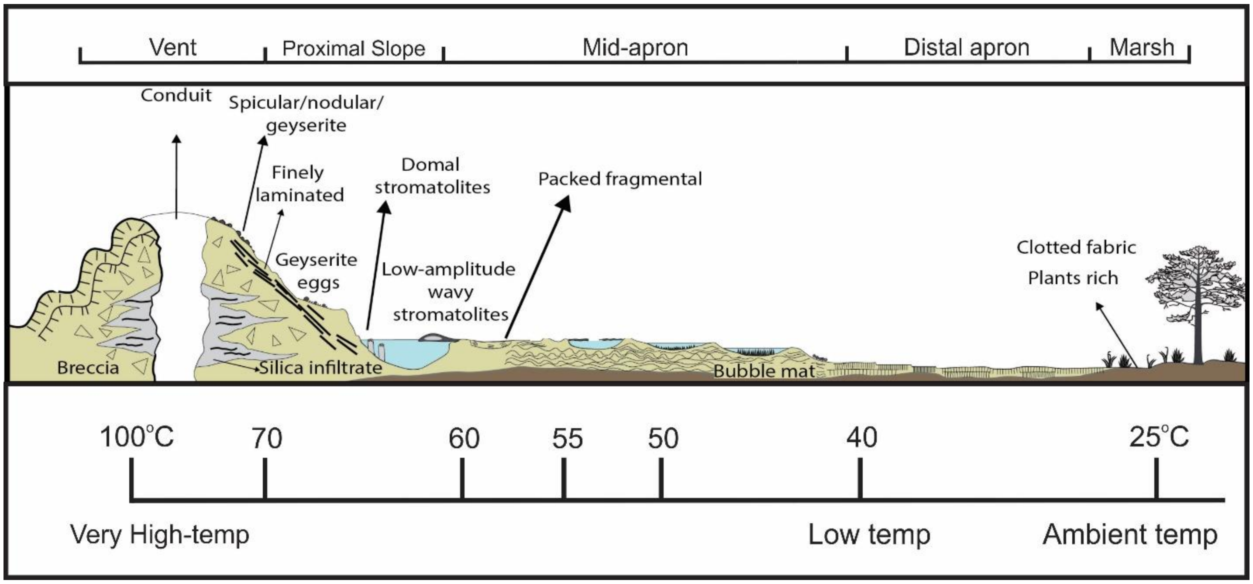

Figure 1.1: Simplified schematic of surficial features commonly found around silica-rich hot spring vents associated with low sulfidation epithermal deposits. The features are sectioned into different areas along the slope starting from the vent onward and are also associated with specific temperatures. Dimensions of the environment vary across locations. Modified from Hamilton et al. (2019).

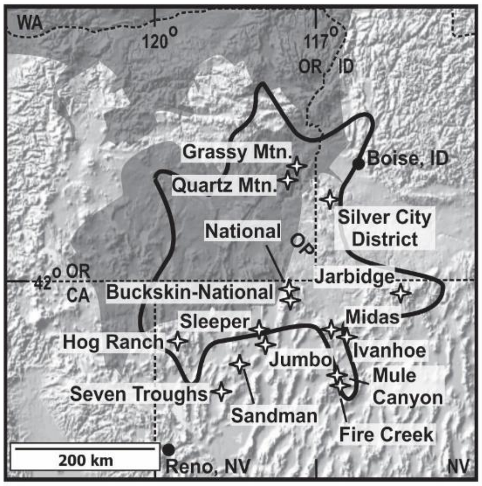

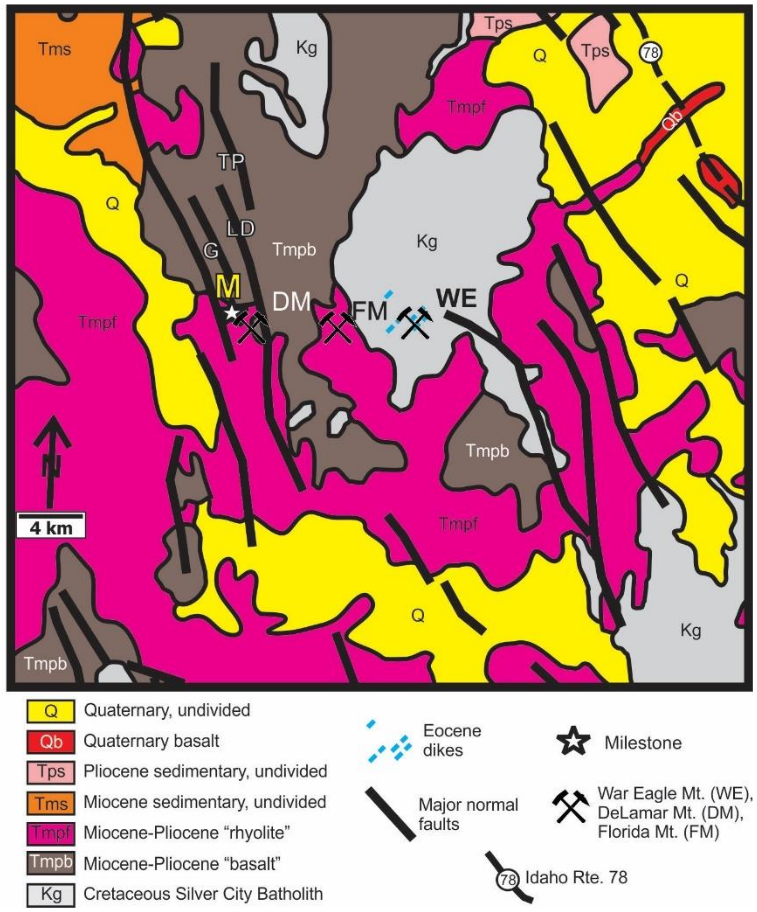

Figure 1.2: (A) Map of northern Great Basin (U.S.A) showing ~17-14 Ma epithermal Au-Ag deposits/districts, extent of Columbia River Basalt group volcanism (gray shading), and coeval rhyolite volcanism (encompassed by thick black line). Owyhee Mountains study area (Silver City district) is labeled. Abbreviation: OP, Owyhee Plateau. (B) General geological map of Owyhee Mountains, ID (after Ekren, et al., 1981; Bonnichsen, 1983; Bonnichsen and Godchaux, 2006; Mason et al., 2015). Silver City encompasses War Eagle (WE), DeLamar (DM), and Florida (FM) Mountains. Milestone deposit is marked by yellow "M" along with other deposits Georgiana (G), Lucky Day (LD), and Twin Peaks (TP) along the faults. Wagonwheel sinter lies between Milestone and Georgiana.

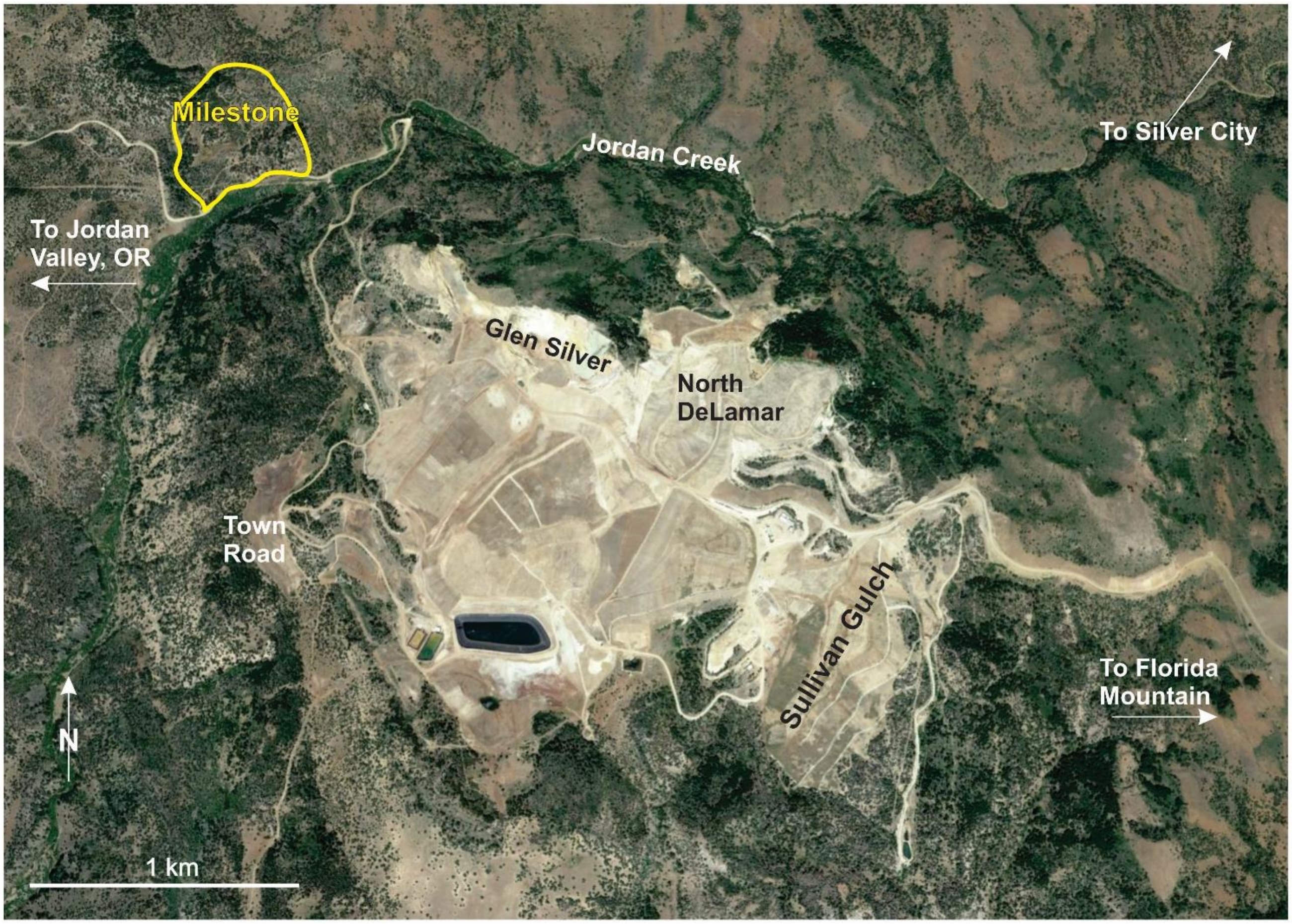

Figure 1.3: Map of the Milestone deposit and the DeLamar mine in Owyhee County, Idaho. Source: Gustin and Weiss (2017)

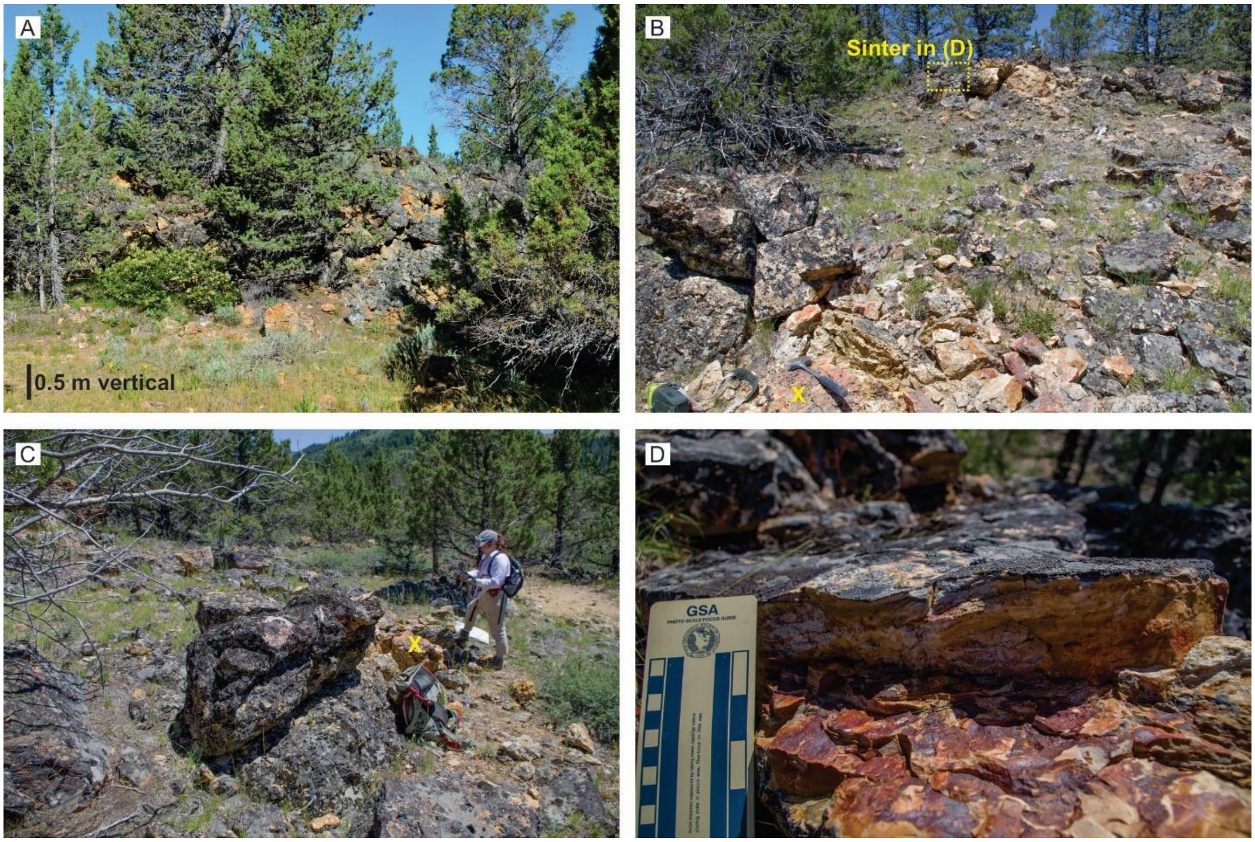

Figure 1.4: Field photos of the Main Knob at Milestone. A) View of the Main Knob from the road. B) View from the bottom of the Main Knob pointed up-slope. Rock marked with yellow "X" is matrix-supported breccia in (C) marked with same yellow "X". C) Matrix-supported breccia at the bottom of the Main Knob with road behind author E. Fenner. D) Broken laminated sinter resulting in a relatively flat surface covered in both lichen and oxidation staining.

Chapter 2 - Methods

Samples were collected to determine the trace metal content and ultimately the economic potential of the deposit. Sampling was also focused on determining whether the breccia type across the deposit is homogenous, as suggested by Barrett (1985), and also to provide constraints on the sinter facies present. In partially preserved and ancient paleosurfaces, such as Milestone, these facies are crucial for uncovering the history and environment of the hydrothermal system.

Sampling locations were determined based on geological mapping (Barret, 1985; this study) and our field observations centered on deposit stratigraphy. The observations made at the Main Knob of Milestone were documented to create a detailed geologic map of the site. Most samples were collected on the Main Knob. Different sinter and breccia types on the Main Knob were grouped into five main lithofacies: Laminated sinter, massive plant-rich sinter, matrix-supported breccia, clast-supported breccia, and geyserite along with notable features such as bubble mat and stromatolite bioformations (Table 1 in Chapter 3). Sampling criteria for the sinter included colorful, defined bedding that would be suitable for point and line analysis by LA-ICP-MS. Any sinter that lacked consistent bedding was noted and also sampled for its fossil content, distance from vent location, and/or phreatic/hydrothermal textures immobilized within. Matrix-supported breccias that exemplified the variety in textures such as gradation, fluvial action, and/or interbedding with sinter were chosen for sampling. Clast-supported breccia was sampled to represent the variation in clast-size around the area. Away from the Main Knob, samples were collected based on color, bedding, and plant fossil content to help identify the farthest reaches of the paleosurface. Another sinter deposit, located about 3 km north-northwest of Milestone known as Wagonwheel, was sampled for comparison.

Overall, twenty-six samples were collected from the Milestone Main Knob and the surrounding area, including Wagonwheel. Fourteen traditional thin sections and twelve double-thick sections (for laser ablation analysis) were cut from sinter samples. Traditional thin sections were used to characterize the mineralogy and hydrothermal textures of the paleo-hot spring that comprises Milestone. In order to obtain quantitative high-precision measurements of our chosen suite of trace elements, LA-ICP-MS was used to analyze as many individual beds as possible. The twelve thick sections, along with six slabs of sinter, were chosen for LA-ICP-MS analysis. All thin sections were observed and described using traditional petrographic methods and reflective-light microscopy imaging. Imaging was performed using a Zeiss Axioscope reflective light microscope attached with a Zeiss Axiocam. Mineral identification was completed using references from Marshall et al. (2011).

Quantitative and spatial relationships of trace metal(loid)s were investigated using laser ablation-inductively coupled-mass spectrometry. Nine samples were analyzed using transects to cut perpendicularly across the laminated sinter beds, and six samples were analyzed with spots on areas of interest. The majority of elements are reported in parts per million (ppm), while Si, S, Se, Te, and Hg are reported in counts per second (cps) as there was no standard for these elements. Possible minor interferences for Se include Ar, K, and Ca, but are generally <10 ppb. Se concentrations mimic Au, Ag, and other geochemically similar elements, thus we interpret any possible interference to be low. In total, 27 elements were analyzed: eight major elements (Si, S, Na, Al, K, Mg, Ti, Fe) and 19 trace elements (Au, Ag, Cu, Zn, As, Cd, Sn, Sb, Se, Te, Hg, Tl, Ge, Pb, Pt, Pd, Bi, Th, U). The element Ge was only analyzed in the slab transects, and Pt and Pd were only analyzed in the spot analyses. All elements were detected in the chosen samples. Six slabs and five double-thickness sections were analyzed by transects perpendicular to sinter bedding or transects that crossed the most beds. Four of the remaining thick sections were chosen for spot analyses where bedding was not as defined. Following Vikre (2007), the transects and spot analyses were used to observe the variations and spatial relationships between individual sinter beds.

LA-ICP-MS trace element analyses were acquired using a New Wave Research/ESI 193nm excimer laser ablation system coupled with a Thermo Scientific iCapQ quadrupole mass spectrometer housed at the Trace Element and Radiogenic Isotope Lab (TRaIL) at the University of Arkansas. For each sample, a line was drawn from left to right across the sample and then expanded for individual spot analyses along the line. Ablation spots were spaced at 350 μm. Each analysis utilized a 100 μm laser spot, a repetition rate of 10Hz with a burst of 200 shots, a fluence of ~9.5 J/cm^2. The elements analyzed were: ^{23}Na, ^{27}Al, ^{29}Si, ^{31}P, ^{32}S, ^{35}Cl, ^{39}K, ^{43}Ca, ^{47}Ti, ^{57}Fe, ^{63}Cu, ^{66}Zn, ^{75}As, ^{77}Se, ^{107}Ag, ^{111}Cd, ^{118}Sn, ^{121}Sb, ^{125}Te, ^{197}Au, ^{202}Hg, ^{205}Tl, ^{208}Pb, ^{209}Bi, ^{232}Th, ^{238}U. NIST standard glass 612 (Jochum et. al, 2011) was used as the primary standard with NIST610 glass as a secondary standard. Data reduction was performed using the Iolite Software Program (Paton et al., 2011). ^{29}Si (99% for unknowns) was used for standardization. The RSD for all elements were <5% except for S whose RSD was ~8%.

Chapter 3 - Results

Main Knob Outcrop Description:

The “Main Knob” is the discharge site of the paleo-hot spring. Its areal extent is ~0.8 km^2, with much of the deposit exposed at the surface. A geologic map (Fig. 3.1) and cross-section (Fig. 3.2) show the spatial relationships of mappable units on the Main Knob. Two types of breccia are present: a matrix-supported breccia and a clast-supported breccia. Clast-supported breccia is found within the center, while the matrix-supported breccia is most common along the outer edges of the knob. The clast-size of the matrix-supported breccia varies from fine pebbles (~0.1 cm) up to large boulders (12 cm) (Fig. 3.3), while the clast-supported breccia has a smaller clast range of 2.5 cm to about 10 cm (Fig. 3.4). The clast-size of these breccias increase with distance from the vent location. The clast-supported breccia is located on the northeast side of the knob, surrounded by the sinter on all sides (Fig. 3.1). Laminated sinter is located in the center of the knob that laterally extends farther than the clast-supported breccia, and massive black sinter exists out to the far edges of the site. The black sinter is found on the outer flanks of the discharge site and contains abundant plant fossils. Petrified wood (twigs, small logs, etc.) is fairly common across the center of the knob in both the sinter and matrix-supported breccia (Fig. 3.5). Geyserite covers most of the central outcrop and can be found as nodular, spicular, ripple, and geyserite eggs (Fig 3.6). Microbial formations such as bubble mat and spherical stromatolites (Fig. 3.7) were found in a large boulder of sinter on the side of the road thought to be moved by previous mining operations. Descriptions of these facies are summarized in Table 1.

Lithofacies

Matrix-supported breccia:

Description: The breccia clasts are primarily unsorted argillically-altered Silver City rhyolite that have been rounded, likely through milling in an eruption column. Clast sizes range from small pebbles (<~0.1cm) to medium-large boulders up to ~92 cm. The outer portions of some samples are moderately oxidized and other breccia contains a layer of injected black sinter (Fig. 3.3). The matrix comprises of a whitish tan to a light/dark gray sinter. Thin layers of sinter (~2 mm) are interbedded in the breccia, but these bands are sparse. All samples have both rounded to angular clasts. However, matrix-supported breccias with a predominantly gray sinter tend to have a higher abundance of rounded clasts (~80% of clasts) than those with tan, black, or white sinter (~60-70% of clasts). All clasts are pervasively altered sinter or rhyolite.

Interpretation: This lithofacies formed from the result of a violent eruption of the hot spring system at a temperature of over 100°C based on measurements at present day hot spring environments (Hamilton et al., 2019). The sinter matrix and lateral extent of this facies suggest a high-volume eruption. The rhyolite and existing sinter were ripped up through the hot spring conduits and erupted to the surface. The high population of rounded clasts suggest milling in the conduit before erupting, entraining more angular clasts in the process. The higher population of angular clasts in the tan, white, or black matrix-supported breccias suggests an advanced degree of fracturing or a more violent eruption (Tămaş and Milési, 2003).

Clast-supported breccia:

Description: Angular sinter and argillically-altered rhyolite clasts that are more homogeneous in size compared to the matrix-supported breccia. Clast size ranges from very coarse sand to small cobbles (Fig. 3.4 A-D) and are loosely to moderately packed. Individual clasts are coated in a thin (~1-2 mm) deposit of silica with little to no matrix, leaving open space between clasts (Fig. 3.4 A-D). Fallout of this breccia sometimes rests on a bed of curved sinter, forming bomb sags (Fig. 3.4 A). Silica infiltrate is also present and becomes more common with depth (Fig. 3.4 E, F). The infiltrate is comprised of primarily white and tan silica that fills in the open spaces between clasts of the clast-supported breccia, cracks in the country rock, and between sinter beds. The infiltrate is more localized in the clast-supported breccia on the northeast side of the Main Knob. Petrified wood is preserved in this facies and includes smaller branches to twigs.

Interpretation: The angular clasts and lack of matrix, plus areal extent of this deposit, are consistent with a vent conduit. This likely formed via a phreatic explosion that resulted in a collapse of the vent with minor amounts of fluid. Superheated fluid (~70-100°C) broke up laminated sinter and as pressure built up in the vent, a violent explosion ejected the material to the surface. This discharge coated the breccia clasts in silica and ultimately cemented the clasts together. Clast-supported breccias similar to this are a result of a slow decrease in the amount of fluid discharged, precipitation, or a change in groundwater flow direction (Tămaş and Milési, 2003). Other possible causes are joint/fracture development or erosion. The curved sinter bed that some portions of this breccia rest upon suggest that the newest sinter in the area was not yet hardened and still existed as a silica gel at the time of vent collapse. Infiltrate is fed through shallow hydrothermal feeders that are positioned immediately under geyser vents; thus, the presence of infiltrate is consistent with a vent (Campbell et al. 2019). The silica infiltrate was found to most commonly fill in open spaces of the clast-supported breccia and nearby country rock at depths of about one meter below the current topographic surface (Fig. 3.4 E,F).

Sinter:

Description: Multi-colored laminated sinter beds form the proximal apron over the Main Knob. Individual beds are ~1 mm thick and envelop epiclastic deposits in some areas. Sinter colors include white, tan, dark-gray, black, red, and brownish (Fig. 3.5). Quartz-after-calcite (QAC) textures are somewhat common between sinter beds and vary in size (Fig. 3.5 G-I). Fossils of petrified wood, from small twigs to logs, are also found within this facies (Fig. 3.5 J-L).

Interpretation: The variation of color in the sinter samples suggest multiple changes in chemical composition in the discharging hot spring fluid. In several samples, the original horizontal bedding is disturbed through an influx of fluid that either fractures the beds or plastically deforms them (Fig. 3.5 A,D,G). Thin beds (>1cm) of sediment in between sinter beds are interpreted to be the result of changing drainage paths over the surface or smaller eruptions of material (Fig. 3.5 B,D,G,J). As the sinter overlies the matrix-supported breccia, the hydrothermal system likely lowered in temperature following the former eruption. The existence of QAC textures is evidence of boiling fluids.

Geyserite:

Description: Nodular geyserite forms small (~3 mm in height) stalagmite-like features along with botryoidal geyserite proximal to the vent and overlying sinter beds (Fig. 3.6 A-F). Rounded pebbles and spheroids (up to ~4 mm) of geyserite eggs are collected together with a distinct coating of sinter over the eggs, cementing them to the surface on which they were deposited (Fig.

3.6 G). An oxidized crust covers the surface of all geyserite samples. All geyserite was found to be overlying the bedded sinter and exposed to the atmosphere.

Interpretation: The geyserite eggs initially formed in extremely shallow pools in the splash-zone around the vent (>~75 °C) and were pushed away by the flow of discharged fluid to be gathered further down-slope. As these eggs are delicate in nature, their preservation suggests their formation occurred after the vent explosion and collapse. Additionally, their collection down-slope of the vent suggests their formation occurred before the formation of the nodular and botryoidal geyserite. The nodular and botryoidal geyserite formed in the splash-zone of the discharged fluid as the fluid was most likely erupting up and out of the vent after the final phreatic eruption that collapsed the vent during a period of relative quiescence.

Microbiological Facies:

Description: Microbiological textures include wavy laminated sinter, rare warm pool-related stromatolites, and flattened bubbles between sinter beds (Fig. 3.7 A,B). The stromatolite features were concentrically built up layers of sinter that formed into a circle in cross section (Fig. 3.7 A). Bubbles in the sinter were overlain by the continuous buildup of sinter, which became too thick to rise through (assuming a silica gel at the time of bubble formation) and spread out laterally to form its oval shape. The highest population of these textures was found in a displaced boulder located on the road surrounding the Main Knob that was most likely moved by drilling operations around the area (Fig. 3.7 C).

Interpretation: Concentric features and small, oval-shaped gas bubbles that deformed horizontally-bedded sinter point in the direction of the existence of thermophilic microbes in the flanks of the hot spring vent (Fig. 3.7 D). The circular sphere-like formations in the sinter could be a type of low-amplitude stromatolite. Oxygen gas bubbles respired by these microbes through photosynthesis were trapped and deformed with the sinter beds (Hamilton et. al, 2019). Thermophiles such as these can be similar to the microbial mats found around hot springs in Yellowstone National Park and their existence requires a temperature of ~45-55°C (Hamilton et. al, 2019) to thrive, thus suggesting the microbes exist in the distal apron. As described earlier, the formation of the older matrix-supported breccia would require temperatures higher than 100°C and extended to about the same distance as the overlying microbial formations. We suggest that the temperature of the hot spring fluid rose to the surface at a significantly lower temperature than its previous eruptions.

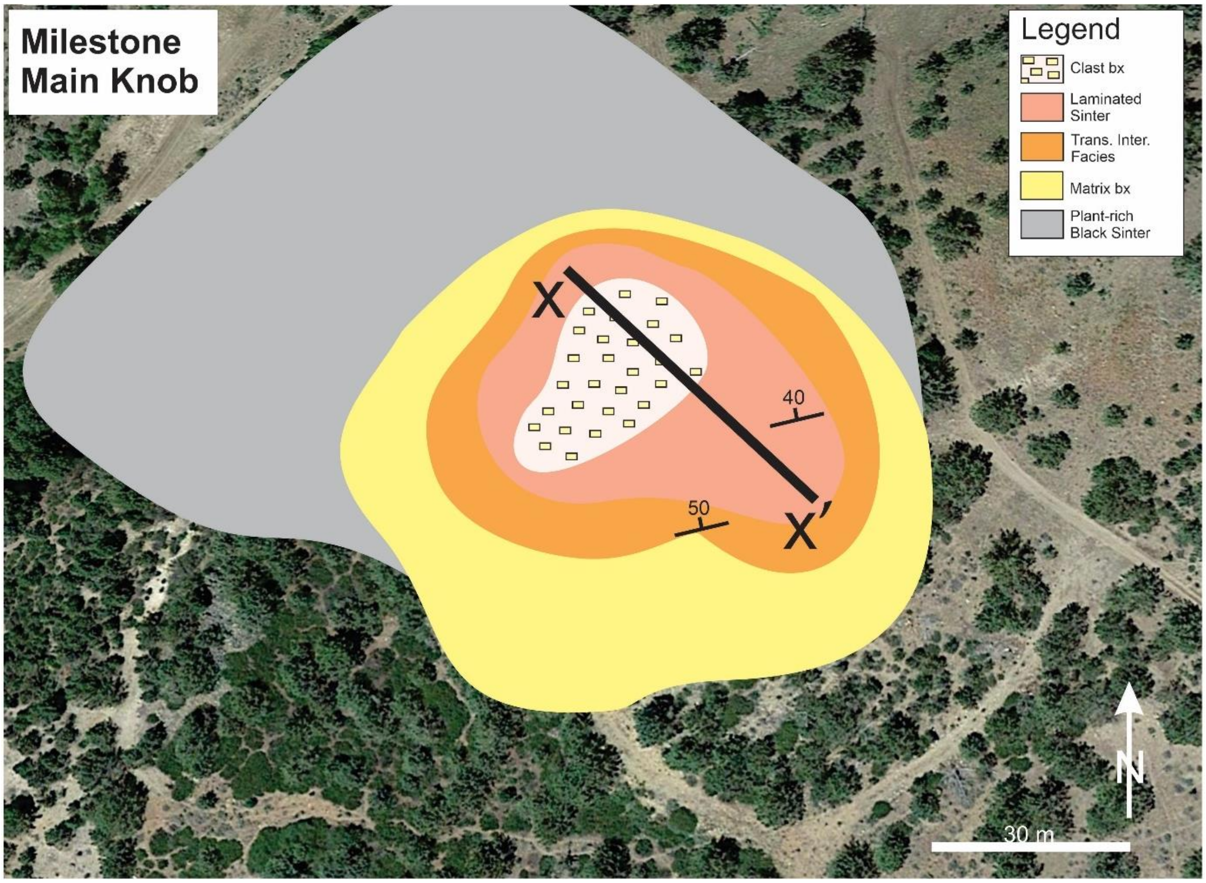

Figure 3.1: Geologic map of the Milestone Main Knob. Bx = breccia. Cross-section along line X-X' in Figure 3.2

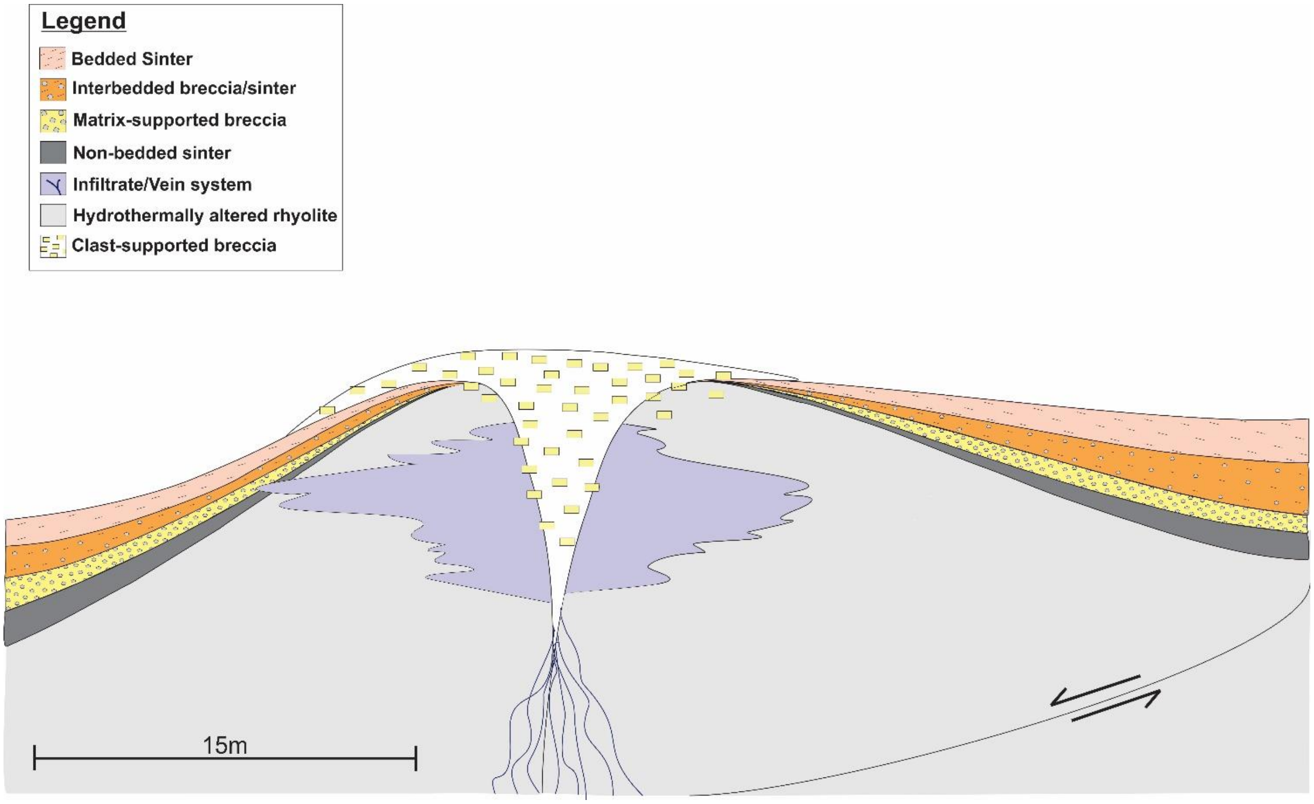

Figure 3.2: Cross-section of the Main Knob across X-X' (left to right) as shown in Figure 3.1. Fault depicted is representative of the Northwest Fault.

Figure 3.3: Matrix-supported breccia found on the Main Knob at Milestone. Unsorted grain sizes range from ~0.1-8 cm. Matrix consists of white, gray, tan, or black sinter, with fine (~0.3 cm) interbedded layers of laminated sinter. A) Matrix supported breccia consisting of gray-colored sinter matrix with white argillically-altered rhyolite clasts (up to ~2 cm) and a single layer of interbedded black sinter. B) Light-tan matrix breccia with an oxidized surface containing large clasts (~8 cm) of argillically-altered country rhyolite. C) Matrix-supported breccia with overlying dark-gray/black sinter. D) Gray matrix breccia with unsorted clasts and interbedded black sinter overlying the breccia.

Figure 3.4: Rock sample images of clast-supported breccia and field images of silica infiltrate. A) Portion of clast-supported breccia that has fallen onto the sinter bed that at the time existed as a silica gel, thus deforming it upon impact. B-D) Clast-supported breccia with varying clast sizes cemented together by a final coating of sinter. E-F) Silica infiltrate (highlighted by yellow line and arrow) taking advantage of pre-existing cracks in the underlying host rock. Image E is rotated 90° from horizontal.

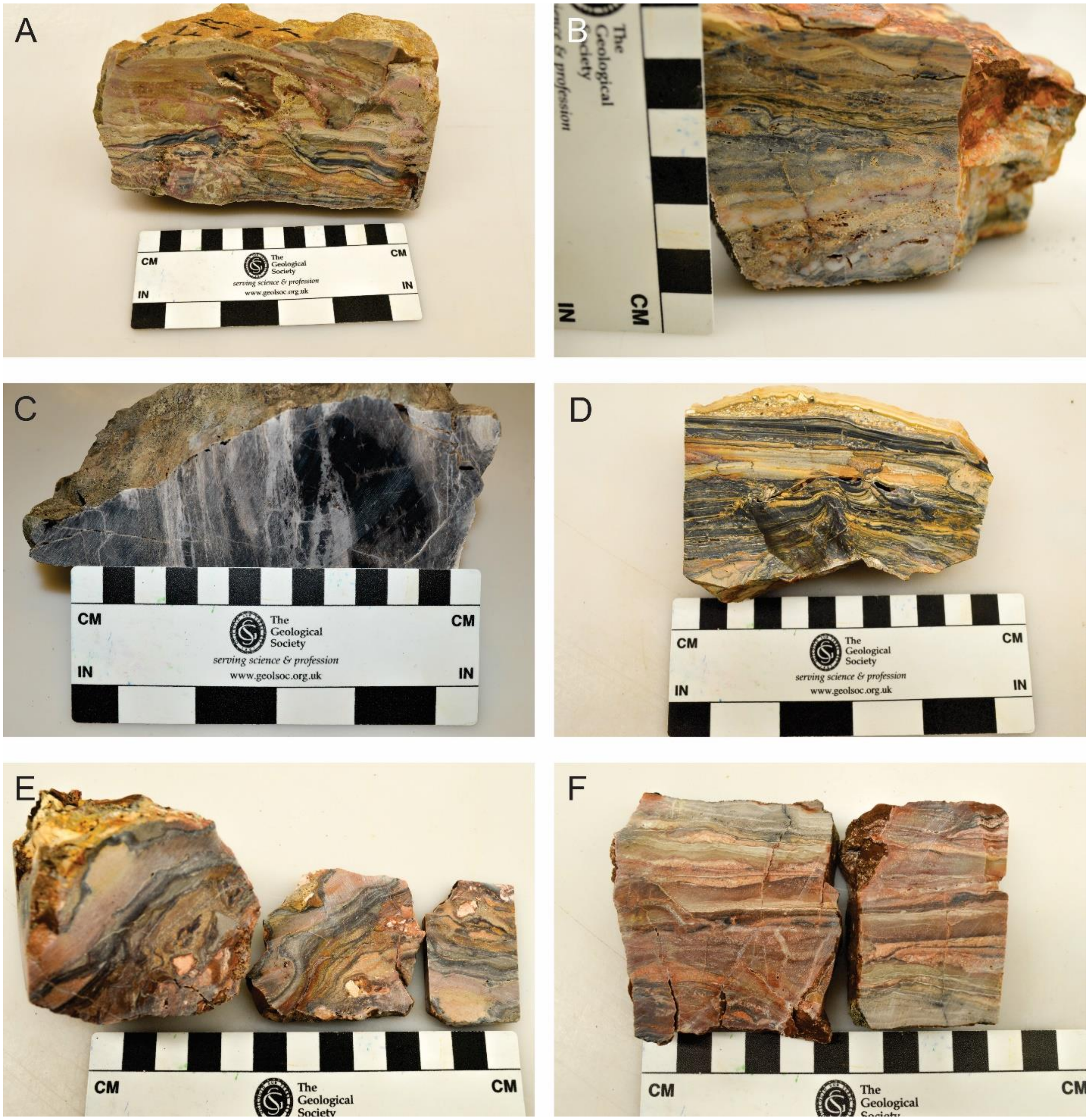

Figure 3.5: Hand samples of colorful laminated sinter found on the Main Knob of Milestone. A) Beds of sinter deformed by fluid injection while existing as a silica gel. B) Laminated sinter interbedded with sediments. C) Massive black sinter with irregular light gray bedding. D) Defined silica bedding with slight deformation, fracturing, and interbedded sediments. E) Irregular sinter layers deformed by and interbedded with angular sinter clasts. F) Defined silica bedding oxidized from Fe-content, based on LA-ICP-MS chemical analyses.

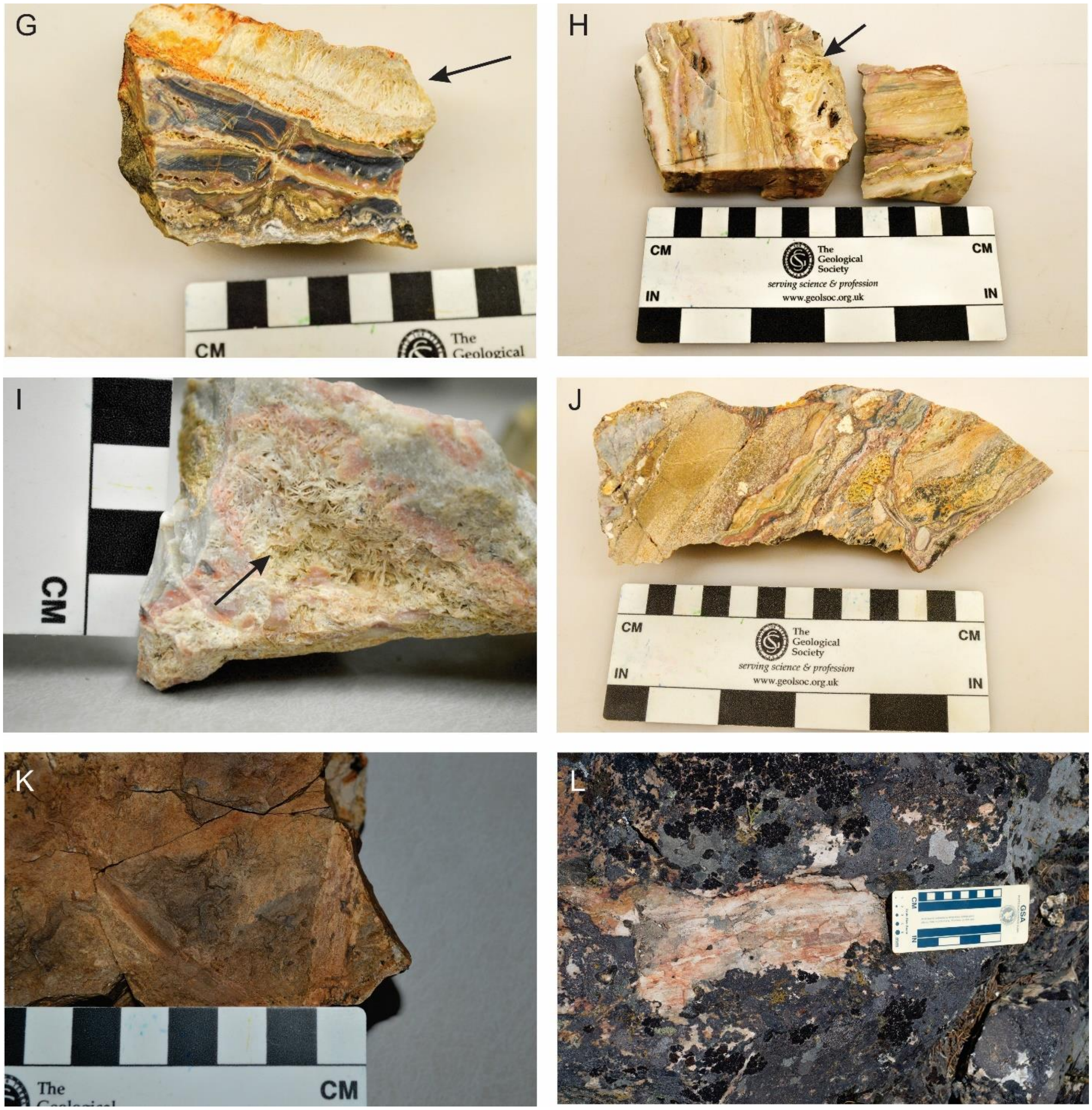

Figure 3.5 (cont.): G-I) Slightly deformed sinter beds incorporating sinter clasts and contain quartz after calcite pseudomorphs (highlighted by arrows). J) Transitional sinter layering dominated by interbedding of sinter and hydrothermally-altered rhyolite clasts. K & L) Fossilized wood fragments ranging from small twigs to medium-sized logs.

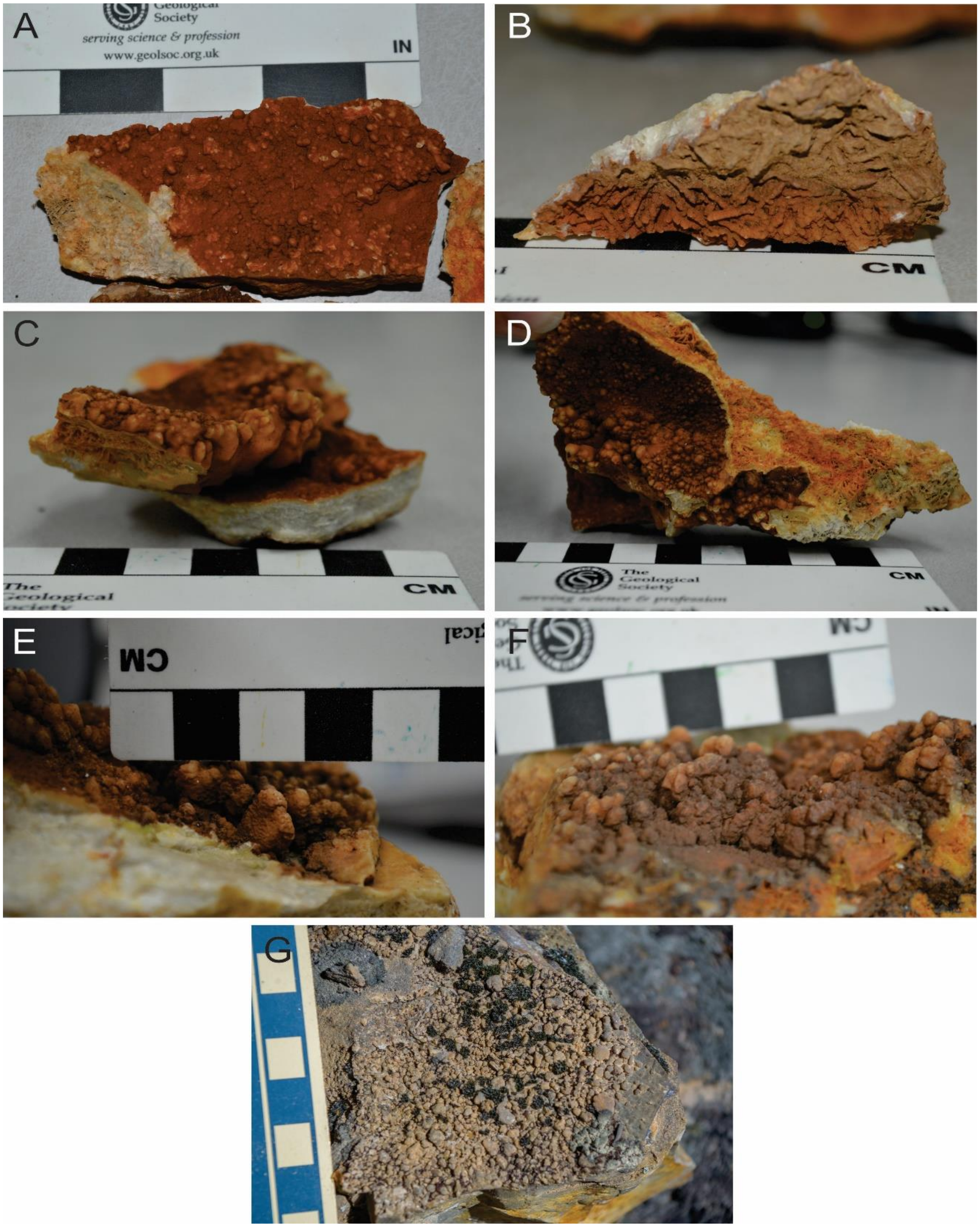

Figure 3.6: Geyserite from the Main Knob of Milestone. A-C) Botryoidal geyserite covering quartz after calcite textures. D-F) Nodular geyserite forming column-like pillars or stalagmites. G) Geyserite eggs collected and cemented together by silica.

Figure 3.7: Microbial features at Milestone. Field book, camera lens cap, and boardwalk included for scale. A) Cross-section of stromatolites (yellow circle) growing off of and with sinter beds. B) Low-amplitude wavy sinter laminations encompassing flattened, oval-like gas bubbles. C) Boulder that shows sinter with microbial textures. D) Microbial mat thermophiles growing in the outflow of discharge in Porcelain Basin at Yellowstone, WY

Table 1: Descriptions and interpretations of the different facies at the Milestone Main Knob.

Facies	Description	Interpretation
Sinter	Multi-colored laminated sinter beds form the proximal apron over the Main Knob (Fig. 3). Individual beds are ~1mm thick and envelop epiclastic deposits in some areas. Colors of the sinter beds include white, tan, dark-gray, black, pink, red, and brownish. Quartz-after-calcite (QAC) textures are somewhat common between sinter beds and vary in size. In several samples, the original horizontal bedding is disturbed through an influx of fluid that either fractures the beds or plastically deforms it. Plant-rich sinter is dark-gray to black and contains silicified remnants of reed and grass-like plants.	The variation of color in the sinter samples suggest multiple changes in trace element composition in the hot spring fluid. Thin beds (>1cm) of sediment in between sinter beds are interpreted to be the result of fluvial action over the surface or smaller eruptions of material. As the sinter overlies the matrix-supported breccia, the hydrothermal system might have lowered in temperature following the former eruption of matrix-supported breccia. The existence of QAC textures is evidence of boiling fluids and deposition of trace elements. Laminated facies form in the proximal slope in fluid temperatures of ~60-75˚ C. Plant-rich sinter is located in the marsh, furthest away from the vent, and is usually an ambient environment (~25˚ C) (Hamilton et al., 2019). Silicified branches, logs, and other plant debris were also found near the vent.
Geyserite	Nodular geyserite forms small (~3mm in height) stalagmite-like features along with botryoidal geyserite. Overlies sinter beds and are proximal to the vent. Geyserite eggs are subrounded (~3.5mm) spheroids and are found further from the vent than other geyserite features	This facies formed in the “splash zone” of the eruptive vent. Falling water from eruptive episodes of fluids flowing upwards and outwards build up and form various features. The temperature of these formations is >75˚ C (Hamilton et al., 2019 and references within)
Matrix-supported Breccia	The breccia clasts are primarily unsorted argilically-altered Silver City rhyolite that have been rounded through milling. Clast sizes range from small pebbles to medium-large boulders spanning up to ~92 cm. Moderate oxidation covers parts of samples in a layer-like fashion and contain a layer of injected black sinter. The matrix comprises of a whiteish tan to a light/dark gray sinter. Thin layers of sinter (~2 mm) are interbedded in the breccia, but these bands are sparse.	The result of more violent eruption of the hot spring system at a temperature of over 100˚ C (Hamilton et. al, 2019). The host rhyolite was ripped up through the hot spring conduits and erupted out in an apron that ends distal from the conduit (~50m).
Clast-supported Breccia	Angular sinter and argilically-altered Silver City rhyolite clasts that are more homogeneous in size compared to the matrix-supported breccia. Clast size ranges from very coarse sand to small cobbles. Individual clasts are coated in a thin (~1-2 mm) deposit of silica with little to no matrix. Fallout of this breccia rests on a bed of curved sinter (Fig. 5). Silica infiltrate is present and becomes more common with depth.	The angular state of the clasts paired with the severe lack of matrix suggest a phreatomagmatic explosion which resulted in a collapse of the vent with minor amounts of fluid. Superheated fluid broke up laminated sinter and as pressure built up in the vent, a violent explosion ejected the material to the surface. This discharge coated the breccia clasts in silica and ultimately cemented the clasts together. The curved sinter bed that some portions of this breccia rest upon suggest that the newest sinter in the area was not yet hardened and still existed as a silica gel. Silica infiltrate in this facies suggests underground temperatures up to 180˚ C, proximal to the vent (Hamilton et al., 2019).
Stromatolite Formations	Rare warm pool-related stromatolites up to ~10 cm in diameter. Stromatolites consist of concentric layers of sinter appearing to grow off the existing laminated sinter beds. Colors range from a light tan to a darker grayish-tan.	The circular sphere-like formations in the sinter are a type of cyanobacteria (e.g., stromatolites). The existence of these bacteria requires a temperature of ~60˚ C (Hamilton et al., 2019) to thrive, and was located in either a proximal slope channel or a mid-apron pool (Fig. 4). This suggests the temperature of the hot spring fluid rose to the surface at a significantly lower temperature than its previous eruptions.
Microbial Mat Formations	This facies is characterized by wavy laminated sinter with bubble mat characteristics, i.e. flattened gas bubbles about 1 mm in length trapped between sinter beds that become wavy to accommodate the gas bubbles. The layers range from light tan to a darker gray-tan in color.	Concentric features and small, oval-shaped gas bubbles that deformed horizontally-bedded sinter point to thermophilic microbes in the flanks of the hot spring vent. Oxygen gas bubbles respired by these bacterium through photosynthesis were trapped and deformed with the sinter beds. Thermophiles that create microbial mats such as these require a temperature of ~45-60˚ C (Hamilton et al., 2019) and can be located in mid-apron pools/channels, or in the distal slope apron. Since the bubble mat exists with the stromatolite facies, we therefore conclude it formed within a mid-apron pool.

Reflected Light Microscopy:

Reflected Light Microscopy (RFL) was primarily used for mineral and quartz identification and description. Here, the minerals and quartz textures found at Milestone are described. Descriptions of all thin sections can be found in Appendix A.

Pyrite:

This phase occurs as both disseminated euhedral pyrite and as clusters. Euhedral cubes and anhedral grains of pyrite exist within the fracture infill of several samples, which could be both crystallized as the infill set and transported from a different source. Clusters include cubic and octahedral crystals up to ~3μm in size (Fig. 3.8). Larger crystals (about 100μm), or relict grains, are thought to be transported from a deeper source due to their rounded and oxidized state (Fig. 3.9). The relict grains and sinter beds with finely disseminated to no visible pyrite are partially oxidized to hematite.

Pyrargrite:

This sulfosalt also known as “ruby silver” was identified in only one sample where it formed as an anhedral crystal about 1 mm in size amongst jigsaw quartz (Fig. 3.10).

Electrum microparticles:

When visible, these grains can appear disseminated or as an accumulation that reflects the flow direction of the hydrothermal fluids. The deposition and accumulation of particles accumulate on the side of the ripples (Fig. 3.11 C & D); this is inferred to be analogous to nanoparticle accumulation on the leeward side of ripples in epithermal veins, creating a sluice-box texture (Saunders et al., 2011b; Saunders, 2012). The particles are more disseminated in the sinter directly beneath (Fig. 3.11 A & B), which could be the aggregations of colloids or nanoparticles forming dendrites (Saunders et al., 2011b; Saunders, 2012; Saunders and Burke, 2017). Disseminated electrum occurs predominantly within the dark gray/black layers of Milestone sinter (Figs. 3.18, 19, 23, 24, 26). The disseminated grains occur as either small globules or as flecks reaching to about 30 μm in size (Fig. 11 E-F).

Quartz textures:

Quartz is the primary and most abundant gangue mineral in the Milestone Main Knob deposit and occurs in several different textures. The sinter itself is layered amorphous silica characterized by massive, laminated or jigsaw quartz. Jigsaw quartz is the most common texture after amorphous sinter. Late-phase veinlets of silica fluid host colloform, comb, and pseudo-acicular quartz.

Massive/jigsaw quartz:

Massive and jigsaw quartz is what comprises the majority of the Milestone sinter. This texture is characterized by aggregates of microcrystalline to crystalline quartz with interpenetrating grain boundaries that can be recognized under cross-polarization. Jigsaw quartz is a recrystallization texture of (usually) chalcedony that requires a temperature of about 180°C (Fournier, 1989; Saunders, 1995; Moncada et al., 2012). In thin section, this texture contains fine anhedral quartz grains that are, on average, less than 3 μm in size, but some grains are up to ~5 μm in size (Fig. 3.10).

Quartz after calcite:

In epithermal formations, bladed calcite is a common formation in veins. The calcite is then replaced by late-stage silica-rich fluids. In Milestone, quartz-after-calcite textures appear as both bladed and lattice-bladed, with the latter being more common. Bladed or platy quartz-after-calciteis where calcite blades are stacked on top of each other in thin, parallel to subparallel arrangements. Lattice-bladed QAC is characterized by blades of calcite that grow in clusters and cross over one another, leaving polygonal voids between blades. Silica-rich fluids will then infiltrate these formations and replace all calcite with quartz. The blades will often have overgrowths of comb quartz growing towards the center of the void space (Fig. 3.12).

Comb quartz:

Comb quartz is a vein texture where subparallel rows of subhedral quartz grow towards each other in the voidspace of a vein, or open space within sinter. These quartz prisms grow off of and perpendicular to the vein wall and occasionally meet in the center. This texture is most common within QAC textures as empty space is needed to form the subhedral nature of the crystals (Fig. 3.13).

Colloform quartz:

Quartz can form a colloform habit as a secondary fluid phase infiltrates any fractures/voids in the sinter. Colloform quartz forms parallel to subparallel layers with a rounded or botryoidal upper surface. It is a primarily depositional phase in fractures as siliceous fluids move in to fill those voids and area a result of cooling and pressure decreases (Moncada et al., 2012; Sillitoe, 2015). Impurities in the fluids create differentially colored layers from gray to transparent, as is seen at Milestone.

Pseudo-acicular quartz:

Plumose-textured quartz forms as subparallel layers alternating with jigsaw and chalcedony. Plumose quartz is characterized by small fibrous crystals radiating out from a singular nucleation point. Under cross-polars, this texture exhibits undulatory extinction. Impurities are arranged across the growth direction in plumose textures (Fig. 3.14).

Chalcedony:

Chalcedony is a form of banded, fibrous, and radially-oriented quartz. Chalcedony forms in a colloform texture and fills up fractures/voids as a secondary texture in most samples. Due to the radial growth of chalcedony, the fibers of the crystal create a plumose extinction. Impurities are common with the chalcedony and form slightly different colored bands and, in one sample, contain inclusions of pyrite (Fig. 3.15).

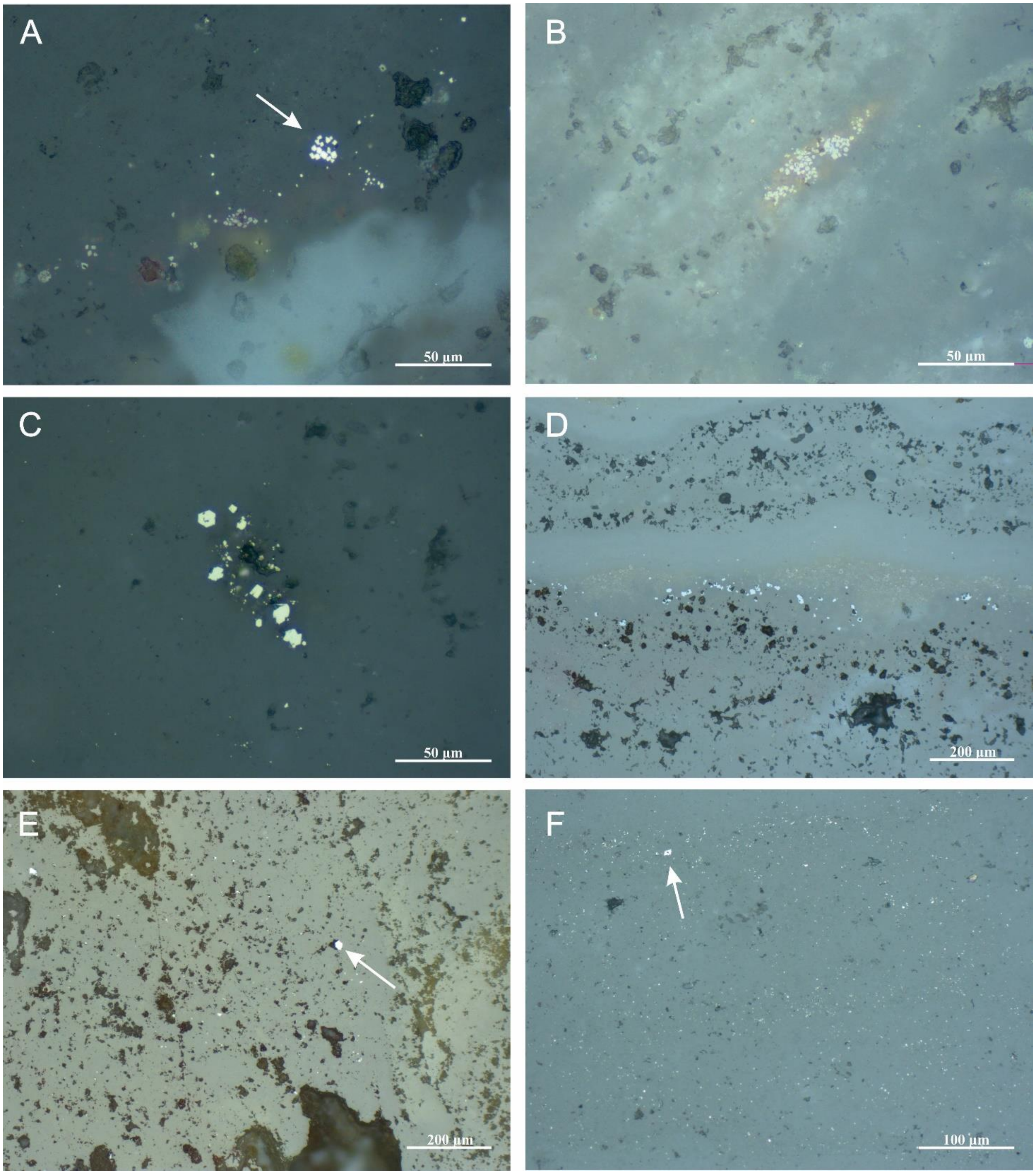

Figure 3.8: Reflected light (RFL) images of clustered and disseminated pyrite from several samples of Milestone Sinter. A-C) Clusters of sub- to euhedral pyrite interbedded with sinter with slight oxidation; arrow points to cluster of pyrite. D) Pyrite deposited on the lower surface of a silica veinlet. E-F) Disseminated an- to euhedral pyrite grains across multiple sinter beds with arrows pointing to larger grains.

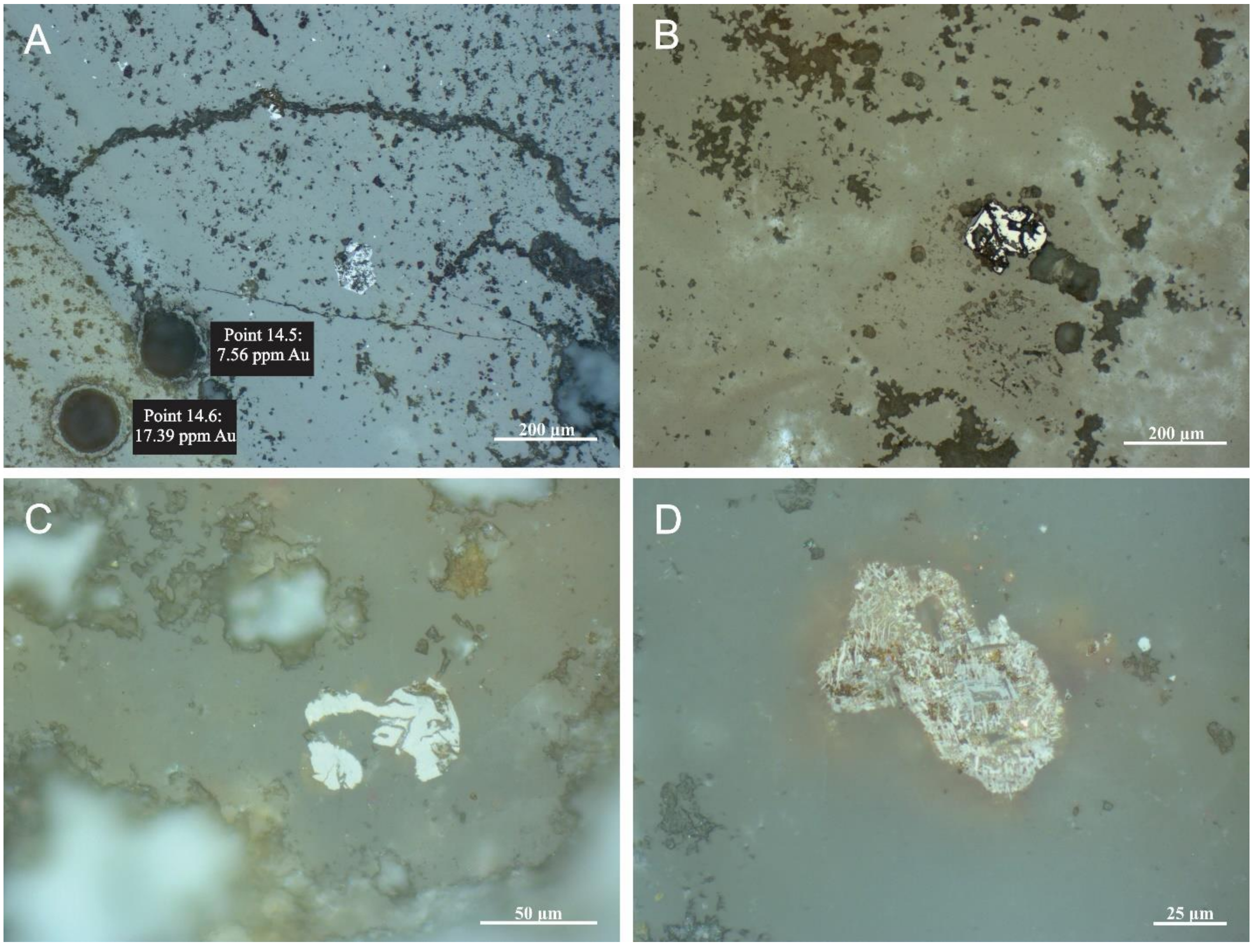

Figure 3.9: RFL images of anhedral pyrite relict grains that have been partially fractured and/or oxidized as a result of their transportation into a water-rich environment and deposited in a silica gel. A) Euhedral pyrite relict just beyond a different sinter bed. Two LA-ICP-MS spots are present in both beds. B) Anhedral pyrite relict in massive sinter. C) Broken pyrite relict fragmented by emplacement within massive sinter. D) Oxidized anhedral pyrite relict in massive sinter.

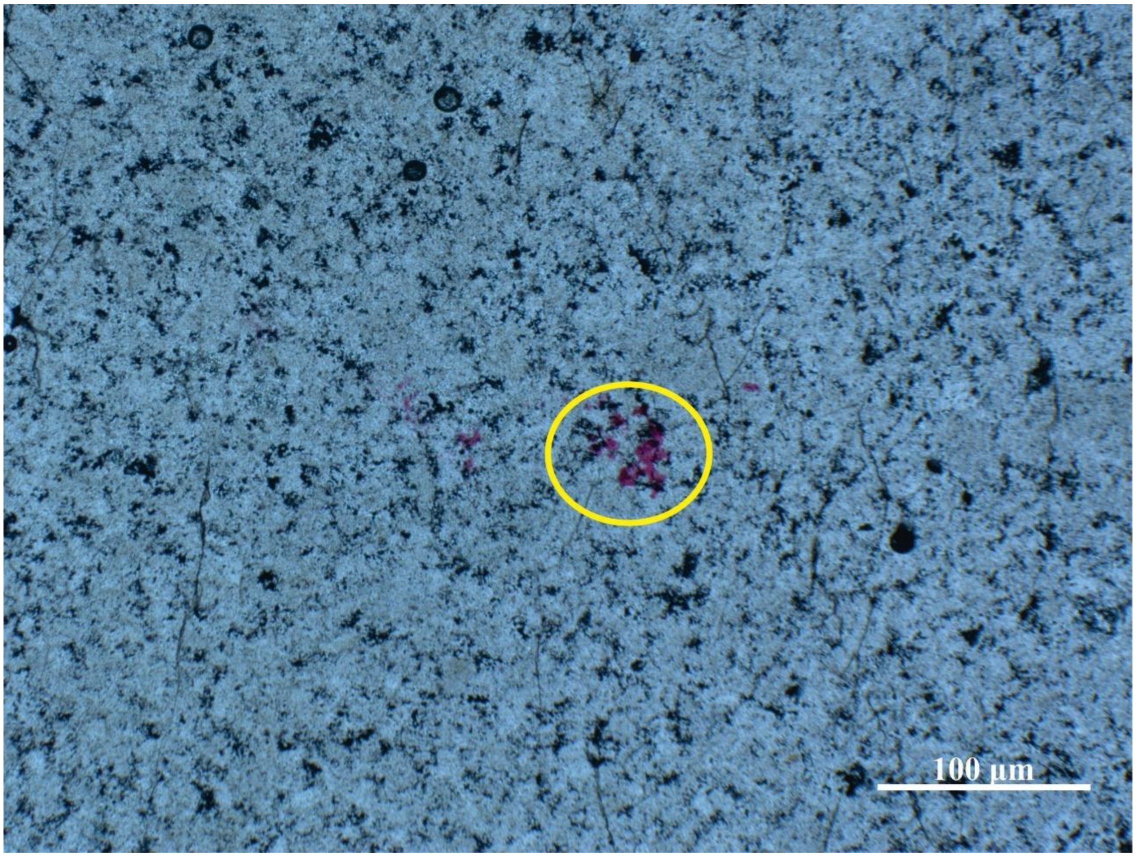

Figure 3.10: Photomicrograph on a double-thick fluid inclusion slide of red anhedral pyrargyrite in massive/jigsaw quartz.

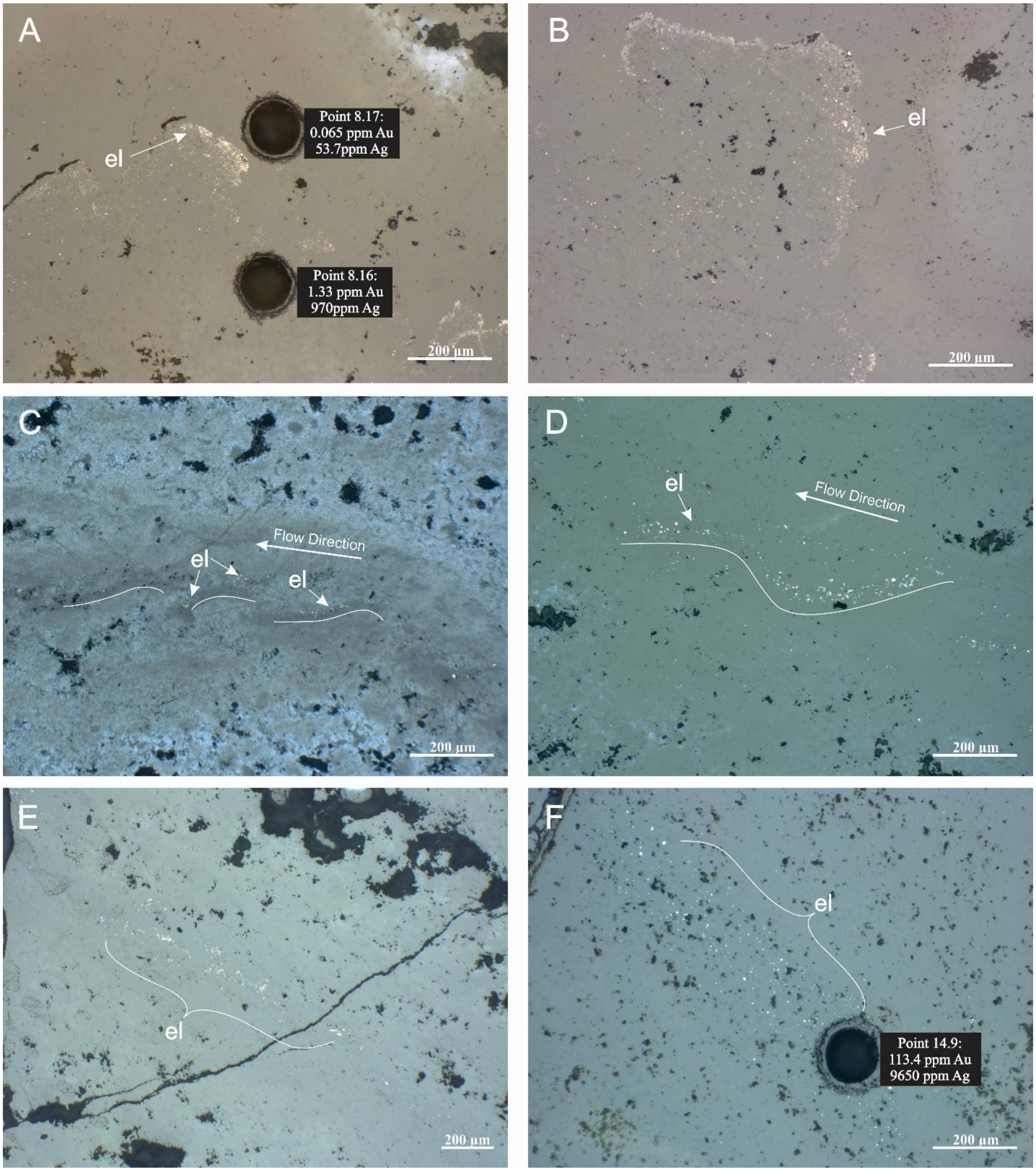

Figure 3.11: RFL photomicrographs of electrum across several samples. A-B) Dendritic crystals of electrum enveloped by silica with deposition of electrum on the leeward side of these formations. C) An RFL image on low power of chalcedony veinlet and D) the same veinlet on high power showcasing flecks of sluice-box textured electrum. Fluid flow is from right to left. E-F) RFL image of disseminated electrum colloids/nanoparticles in sinter beds.

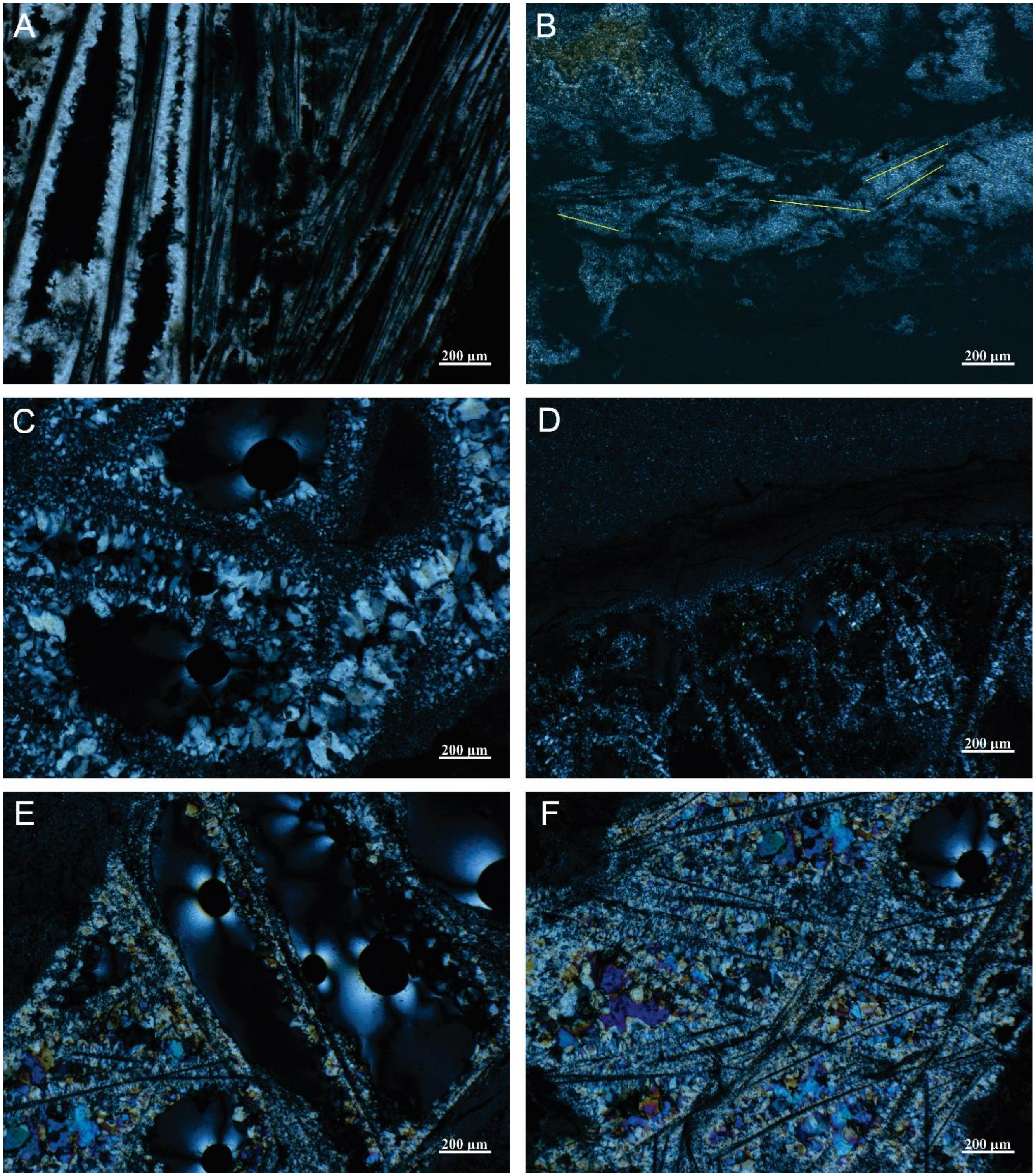

Figure 3.12: Cross-polarized images of quartz after calcite (QAC) formations. A&B) Closely packed bladed QAC with finer comb quartz (A) and microcrystalline quartz (B) replacing and growing off of the yellow highlighted silica-replaced calcite blades. C-F) Lattice bladed QAC with overgrowths of comb quartz and voids in between the blades.

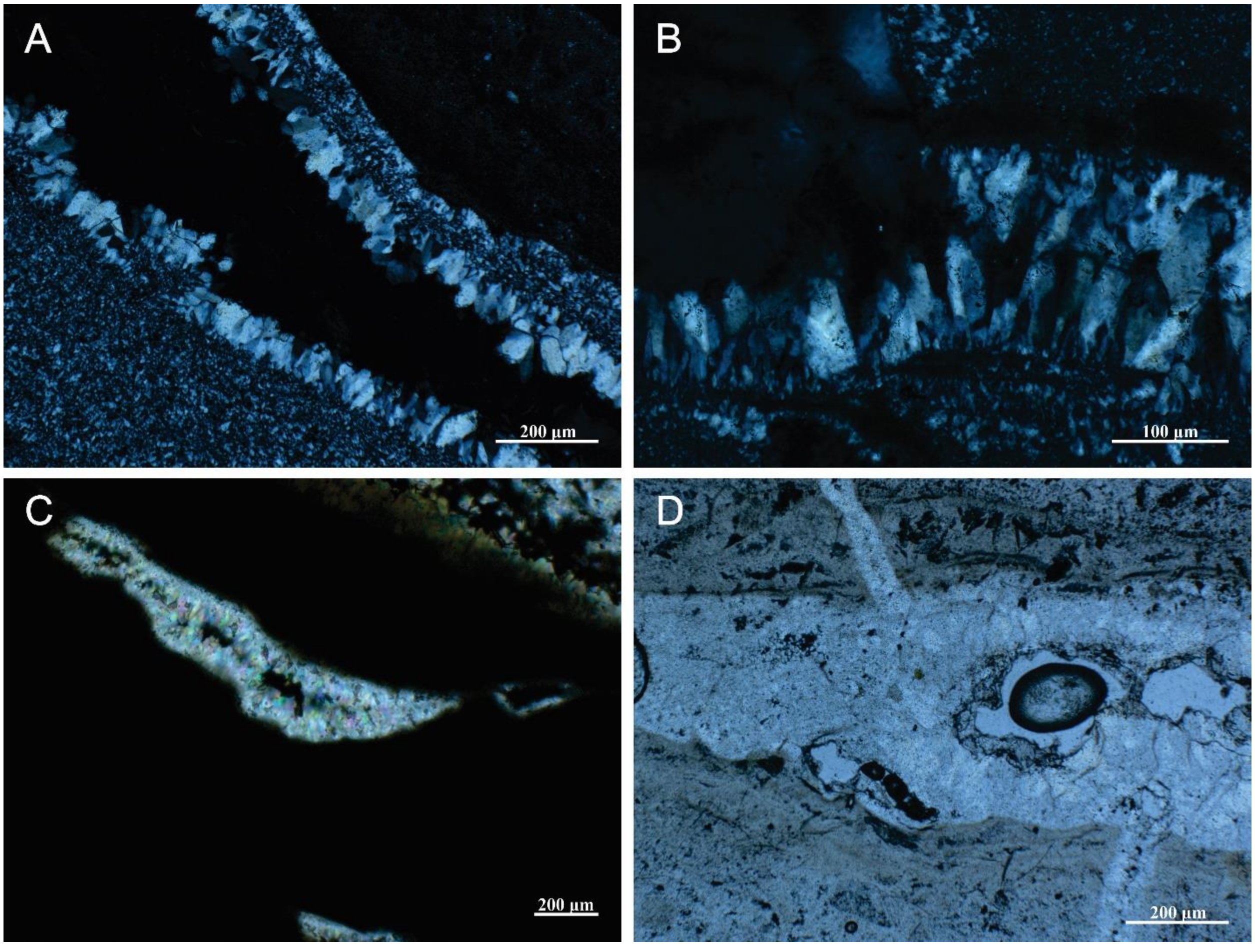

Figure 3.13: Transmitted light images of comb quartz in cross-polars. A-D) Siliceous fluid flowed into the fractures and voids of the rock and crystallized into subhedral prisms where space allows.

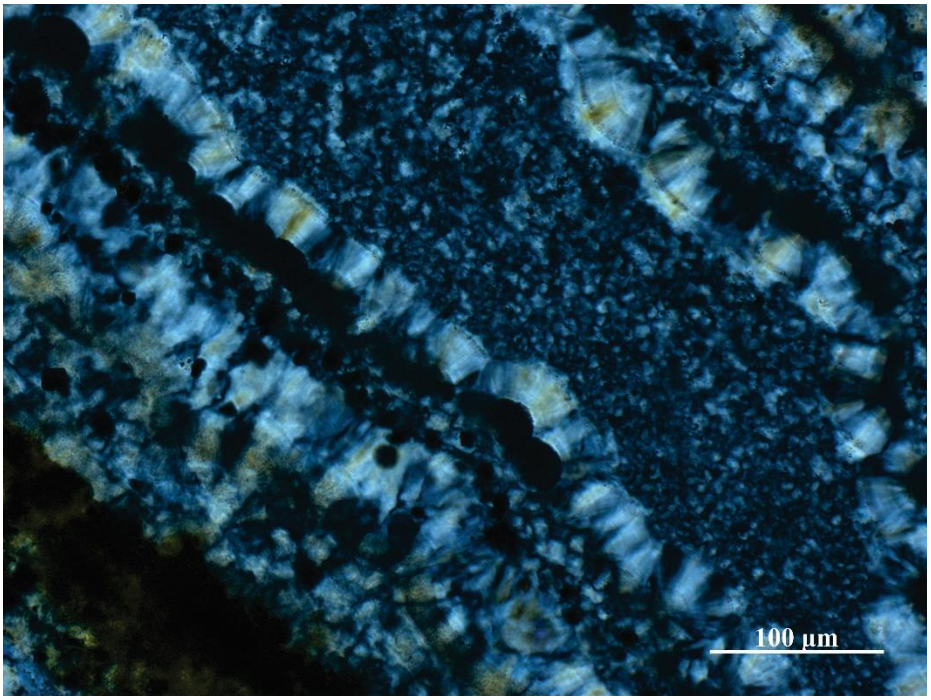

Figure 3.14: Cross polarized photomicrograph of pseudo-acicular quartz crystallization with undulatory extinction in bands of sinter.

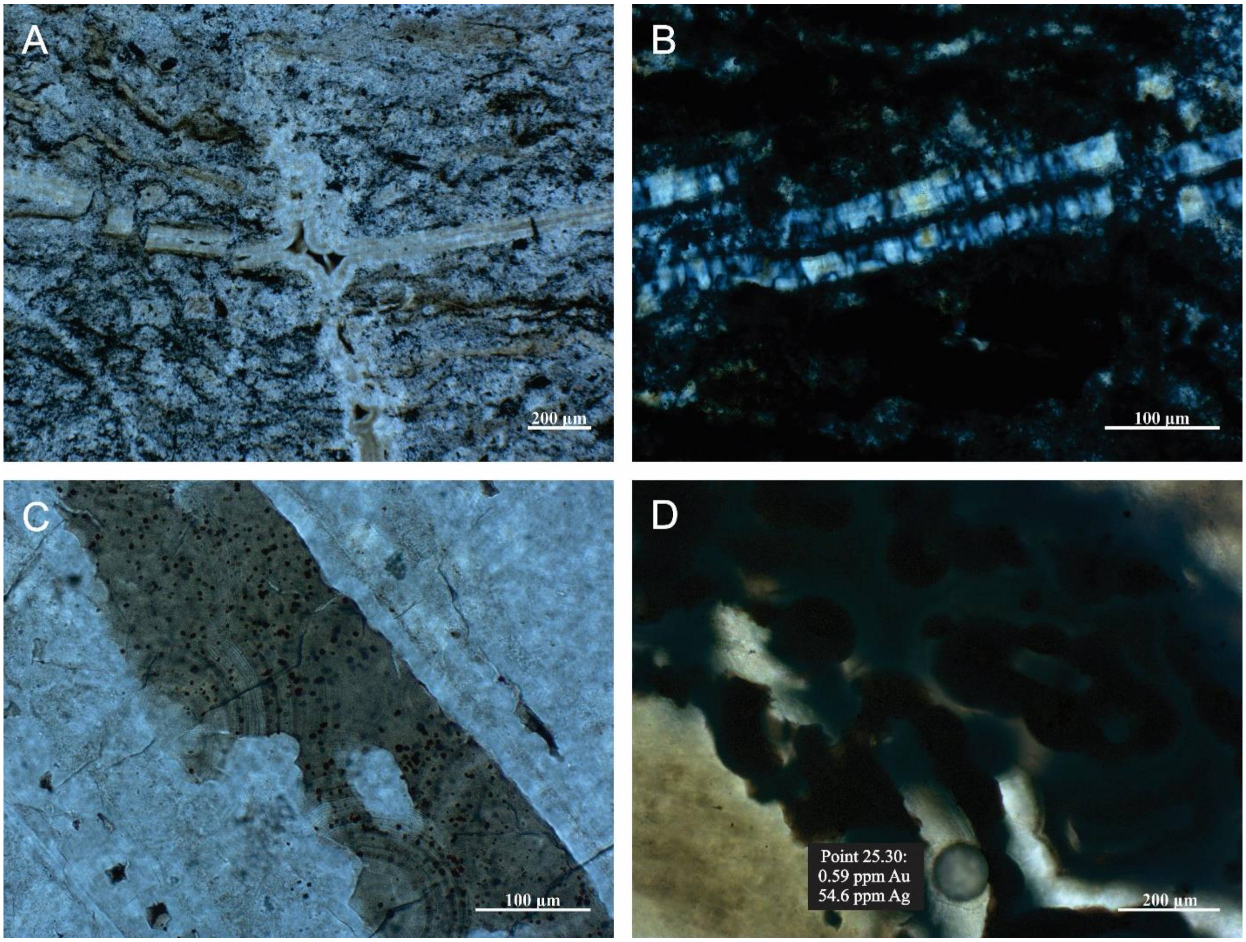

Figure 3.15: Images of chalcedony crystallization as a result of secondary silica-rich fluid injection. A) Low-powered RFL image of vein walls coated in chalcedony which display differential layers and a botryoidal habit. B) Cross-polarized transmissive light image of a chalcedony vein showing pseudo-acicular plumose texture and undulose extinction. C) Chalcedony-filled void that contains differentially colored banding and transported cubed pyrite. The chalcedony is discolored due to the oxidation of the pyrite. D) Transmissive-light image of chalcedony displaying its botryoidal habit and transport of precious metals.

LA-ICP-MS Analysis:

The concentrations of the trace elements vary widely and change between sinter beds. Here, the plots of each sample with measured Au, Ag, Cu, As, Se, Te, and Hg are displayed for simplicity (Figs. 3.16-30). The plots of all measured elements are displayed in Appendix B. Five of the nine transect samples confirmed the presence of electrum by showing significant levels of Au and Ag in the black or dark gray bands of the laminated sinter (Figs. 3.18, 19, 23, 24, 27). White, light gray, and light tan zones have the most consistent and lowest levels of all measured elements (displayed in this section and in Appendix B). Samples that consist of predominantly red sinter (Figs. 3.16, 17, 25, Appendix B) contain elevated levels of Fe and Hg by at least one order of magnitude when compared to the other samples. Spots and transects that go across clasts show elevated levels of Si, Al, and K, confirming the entrainment of the basement rhyolite (Appendix B). The plant-rich black sinters show the lowest ranges of concentrations of Au, Ag, and Cu at 0.26-4.42 ppm, 0.239-30.3 ppm, and 0.39-461 ppm, respectively (Figs. 3.28, 30). The sample from Wagonwheel contained higher levels of Hg (up to 247000 cps) which most likely contributed to the pink and dark red color of the sample (Fig. 3.29). The sinter from Wagonwheel otherwise contained lower concentrations of displayed elements (Au, Ag, Cu, As, Se, and Te) than those at Milestone.

Ranges of Si, S, Se, Te, Hg, Na, Al, Cl, K, Ti, Fe, Au, Ag, Cu, As, Pt, and Pd across all samples analyzed are as follows: Si: 173000-86900000 cps, S: 0-27940000 cps, Se: 0-1580000 cps, Te: 0-445000 cps, Hg: 0-594000 cps, Na: 13.8-357000 ppm, Al: 450-15900000 ppm, Cl: 35.9-5120 ppm, K: 8.6-850000 ppm, Ti: 3.27-78000 ppm, Fe: 2.4-367000 ppm, Au: 0.027-153 ppm, Ag: 0.19-28400 ppm, Cu: 0.11-2590 ppm, As: 0.165-13160 ppm, Pt: 0-0.55 ppm, Pd: 0-1.43 ppm. These specific elements are listed for the sinter's primary constituent (SiO_2), common major elements and rhyolite inclusions (Na, Al, Cl, K, Ti, and Fe), sulfur content in the low-sulfidation epithermal system (S), and accepted pathfinder and economic mineral-forming elements (Se, Te, Hg, Au, Ag, Cu, As, Pt, and Pd). These pathfinder elements behave similarly in epithermal systems and are useful for elements that may not be as easily identified (Saunders et al., 2010).

Despite the great variations of the measured elements, there does not appear to be a clear correlation between element concentrations (Au, Ag, Cu, Se, Te, Hg) and distance from the vent (Fig. 3.31). Increasing distance from the vent corresponds to decreasing temperatures. Each sample collected was categorized into different sections of the hot spring slope: Vent, proximal slope, mid-slope apron, and the distal apron/marsh. The sample from Wagonwheel was included as well for comparison. Some sections, such as the mid-slope apron, contain a high population of samples, thereby providing a wider range of chemical data, in some cases. Only one sample from the vent was analyzed, and consequently, a narrower range of elemental concentrations are associated with the vent. What is clear, is that the distal slope and marsh samples (the black plant-rich sinter) have little to no variation in Au, Ag, or Cu concentrations. These black deposits also host the lowest concentrations of metal(loid)s (Au: 0.26-4.42 ppm, Ag: 0.239-30.3 ppm, and Cu: 0.39-461 ppm).

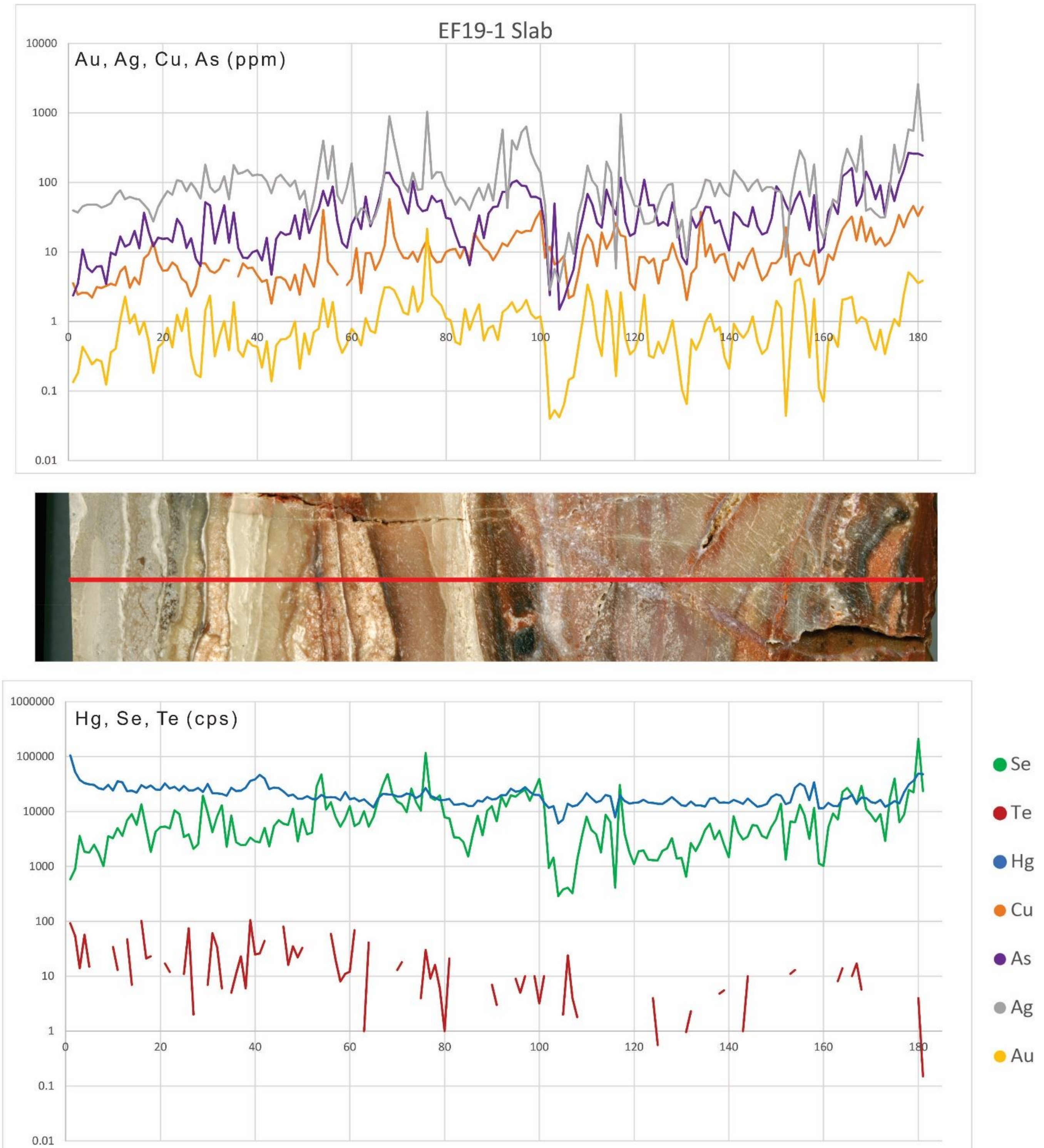

Figure 3.16: LA-ICP-MS transect of proximal slope sample EF19-1 (middle) and data in ppm (above) and cps (below).

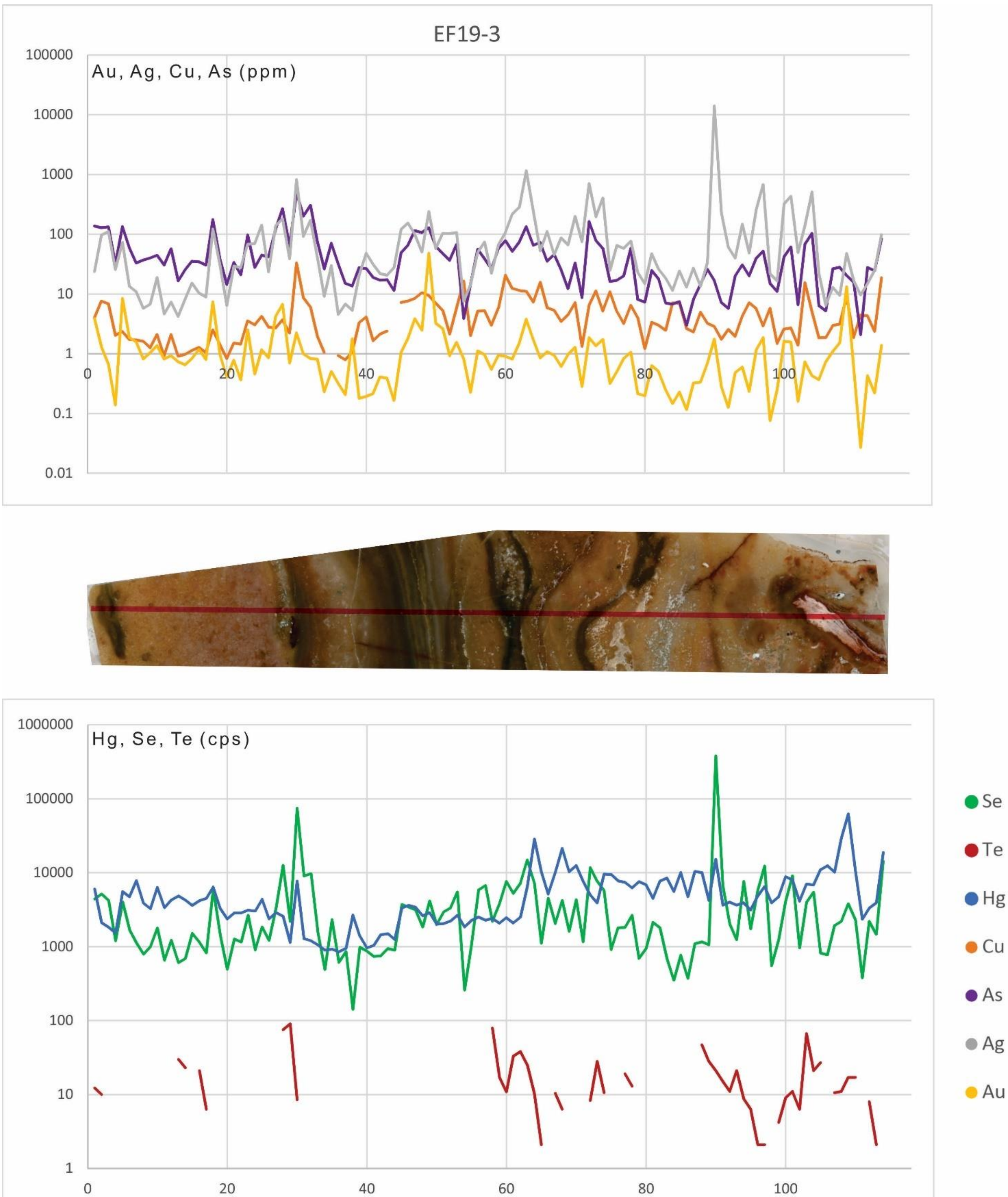

Figure 3.17: LA-ICP-MS transect of proximal slope sample EF19-3 (middle) and data in ppm (above) and cps (below).

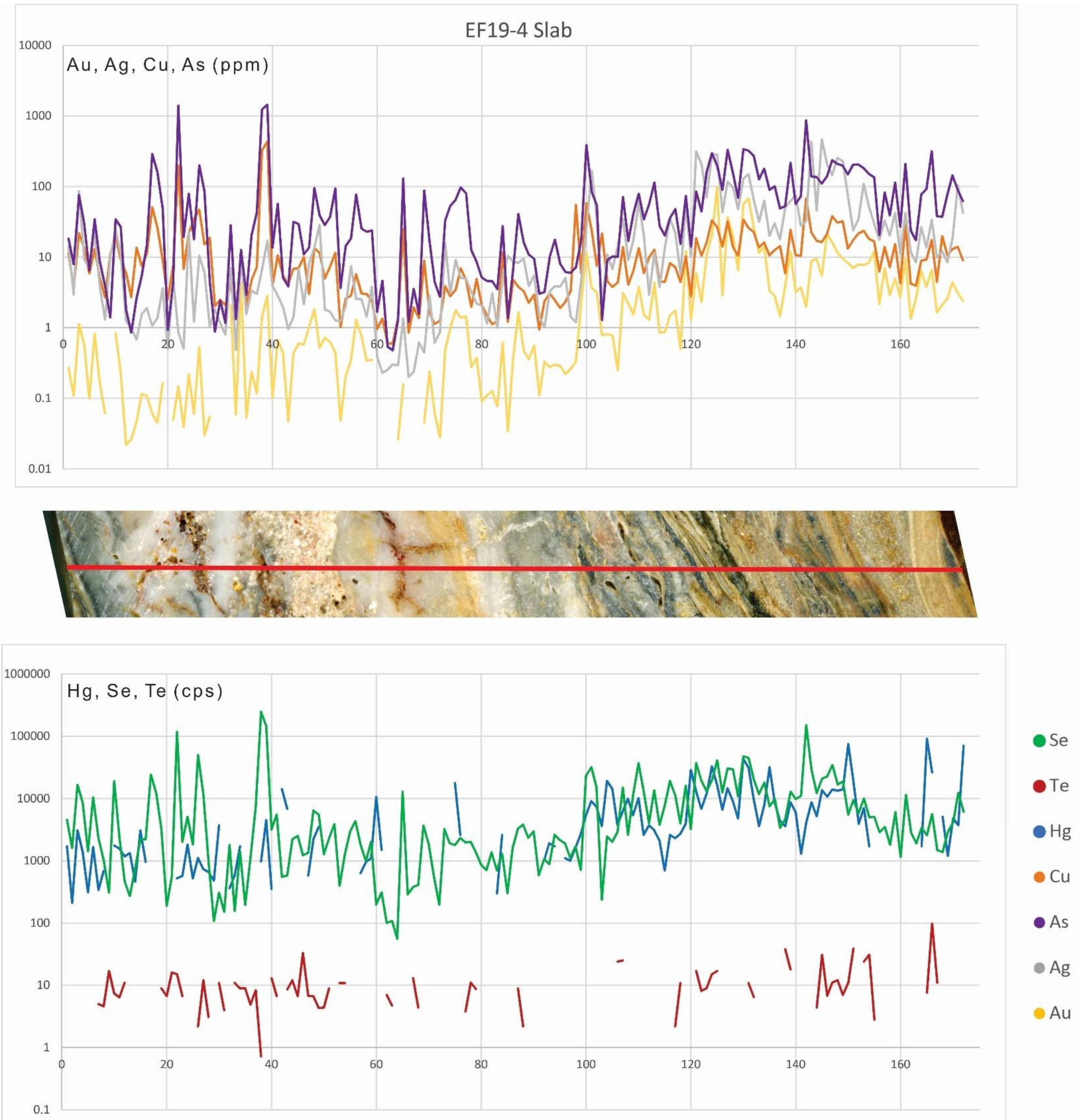

Figure 3.18: LA-ICP-MS transect of mid-slope apron sample EF19-4 (middle) and data in ppm (above) and cps (below).

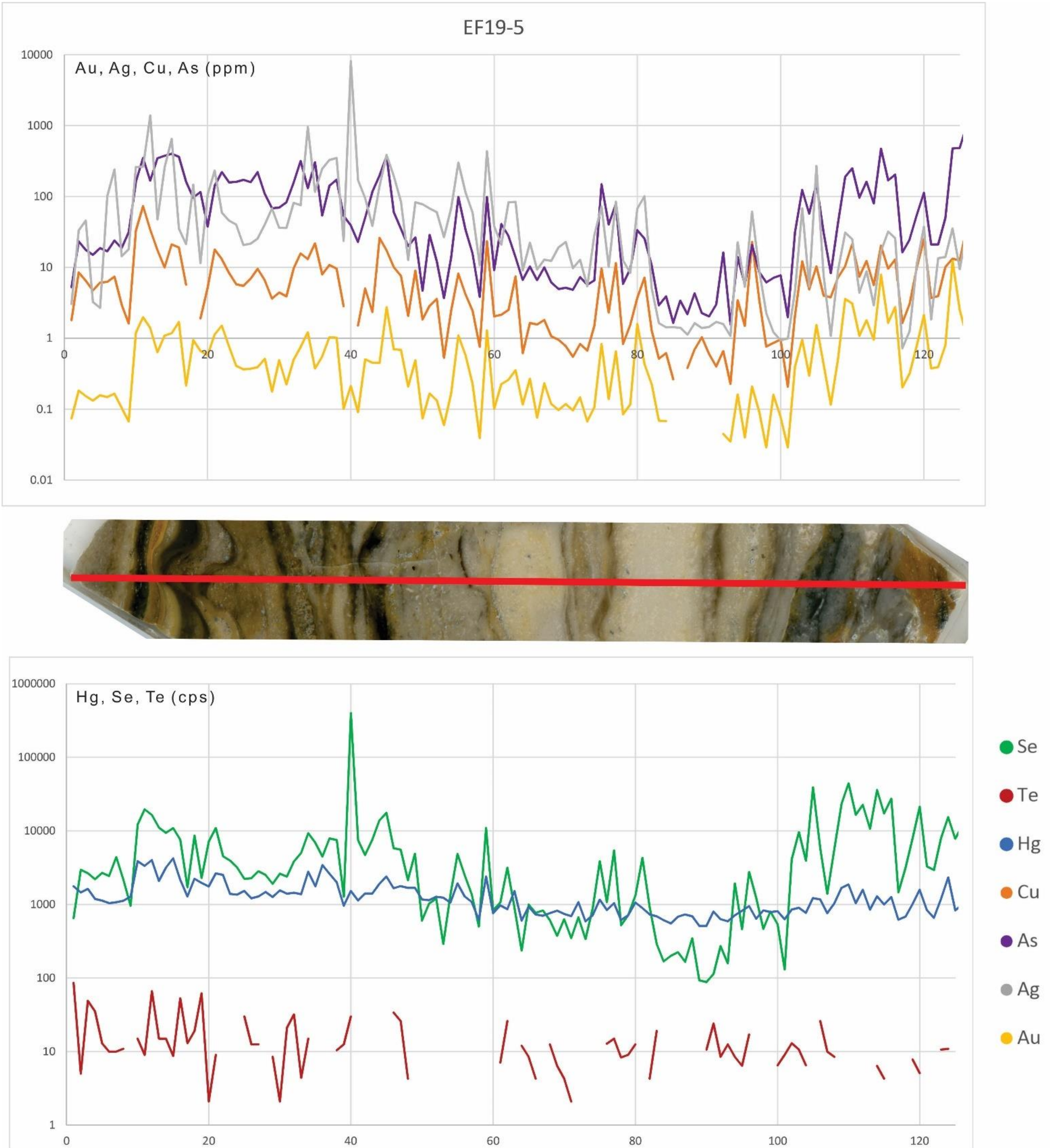

Figure 3.19: LA-ICP-MS transect of mid-slope apron sample EF19-5 (middle) and data in ppm (above) and cps (below).

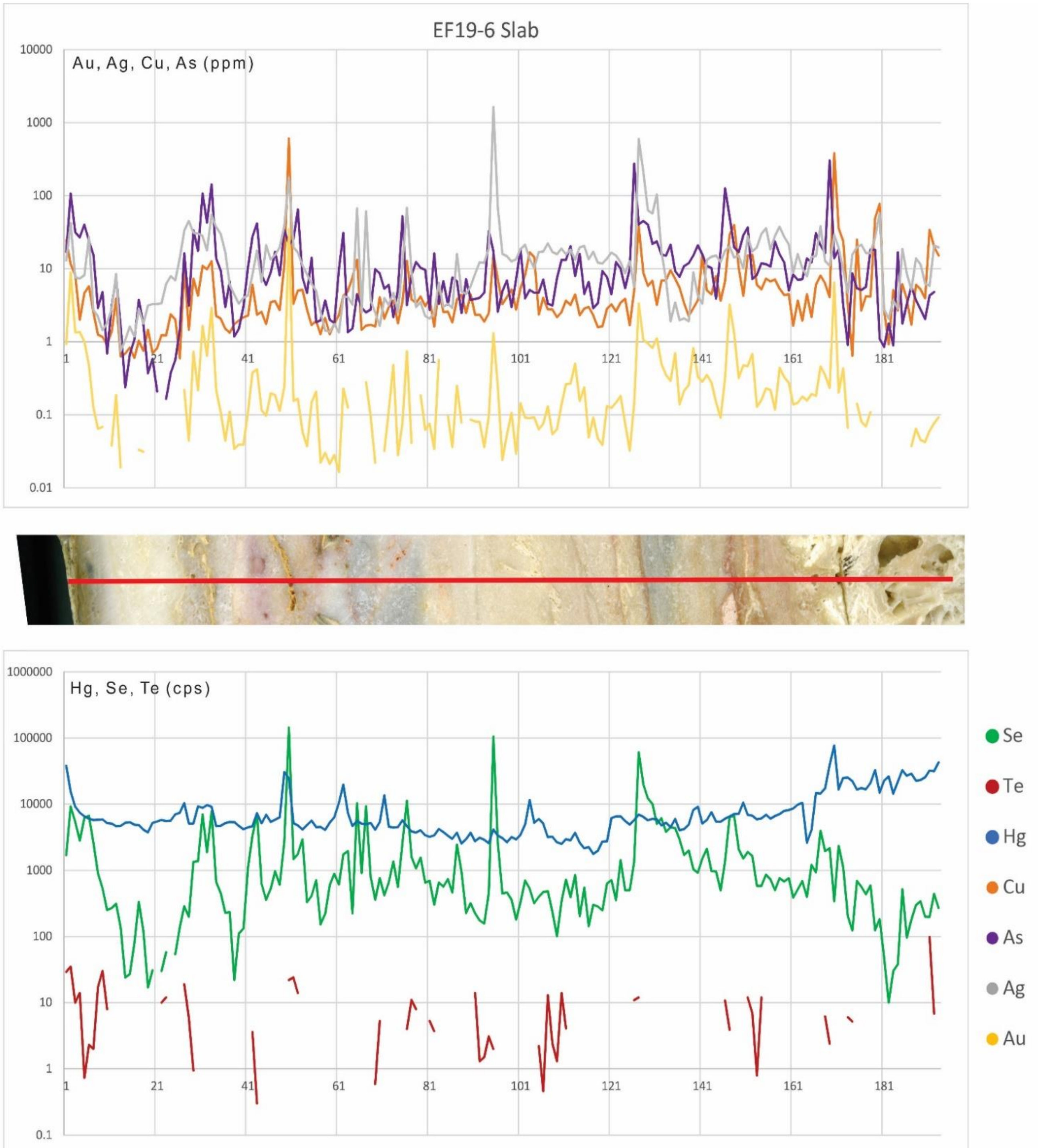

Figure 3.20: LA-ICP-MS transect of mid-slope apron sample EF19-6 (middle) and data in ppm (above) and cps (below).

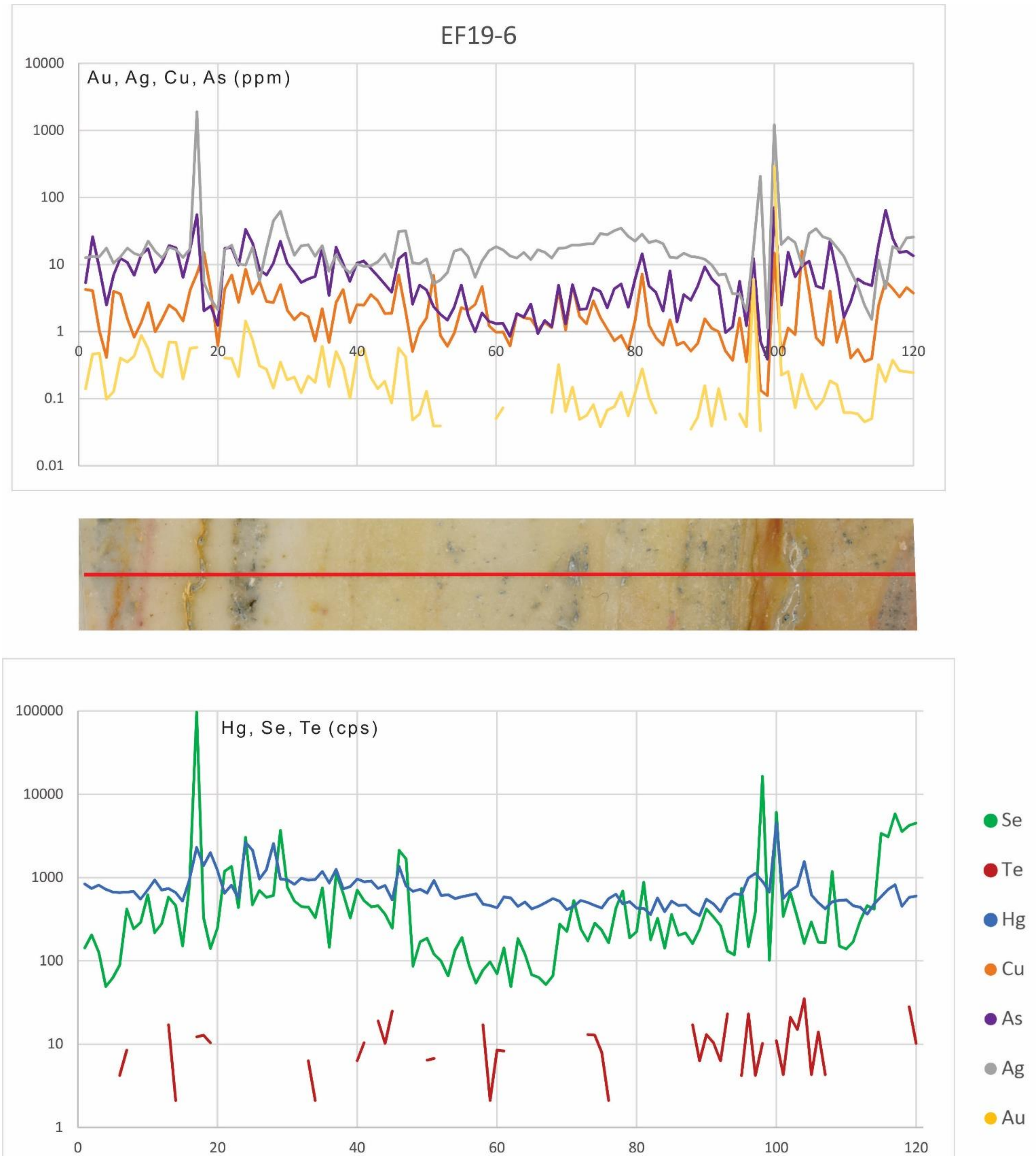

Figure 3.21: LA-ICP-MS transect of a thin section of mid-slope apron sample EF19-6 (middle) and data in ppm (above) and cps (below).

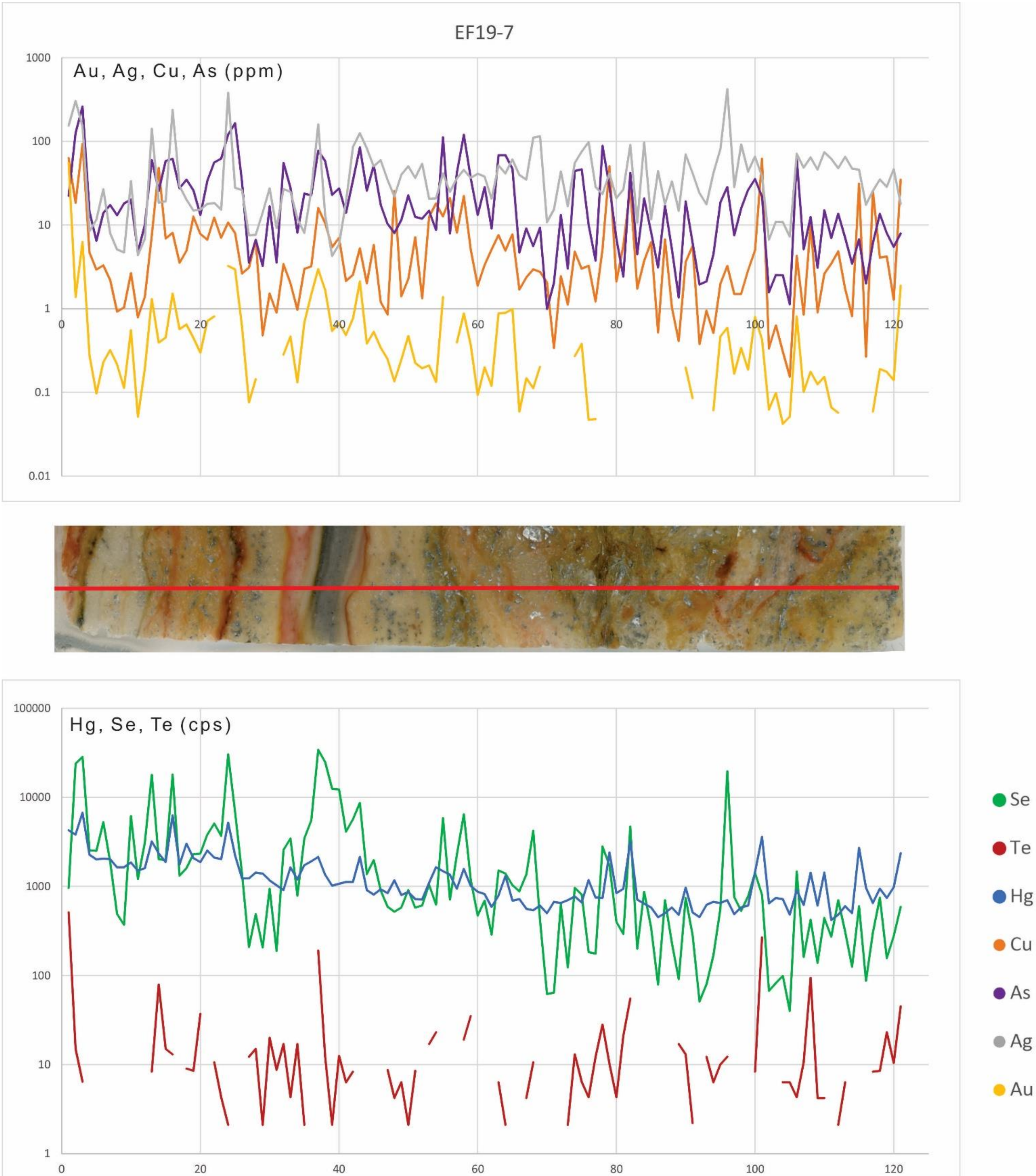

Figure 3.22: LA-ICP-MS transect of vent sample EF19-7 (middle) and data in ppm (above) and cps (below).

Figure 3.23: LA-ICP-MS transect of vent sample EF19-8 (middle) and data in ppm (above) and cps (below).

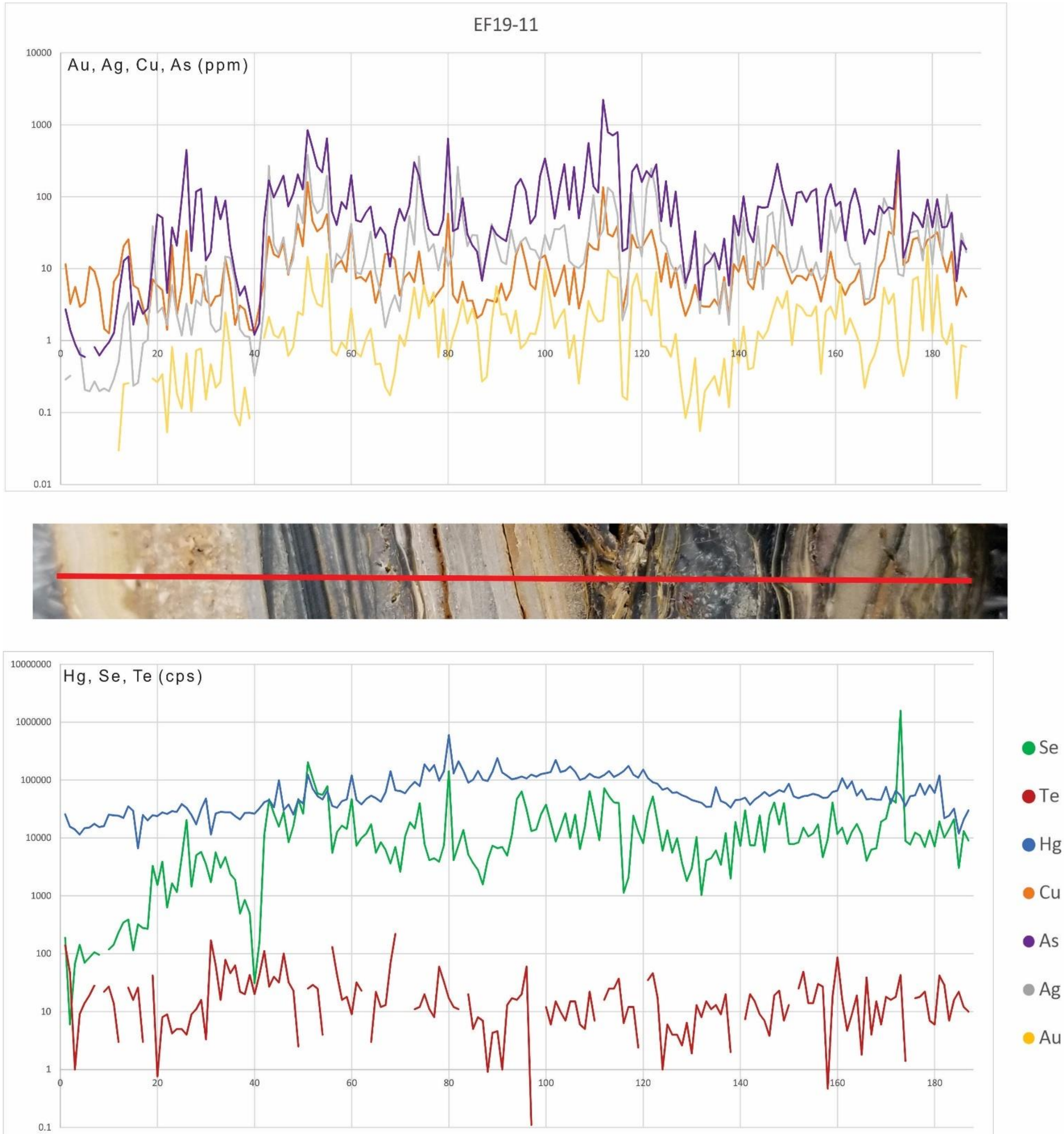

Figure 3.24: LA-ICP-MS transect of proximal slope sample EF19-11 (middle) and data in ppm (above) and cps (below).

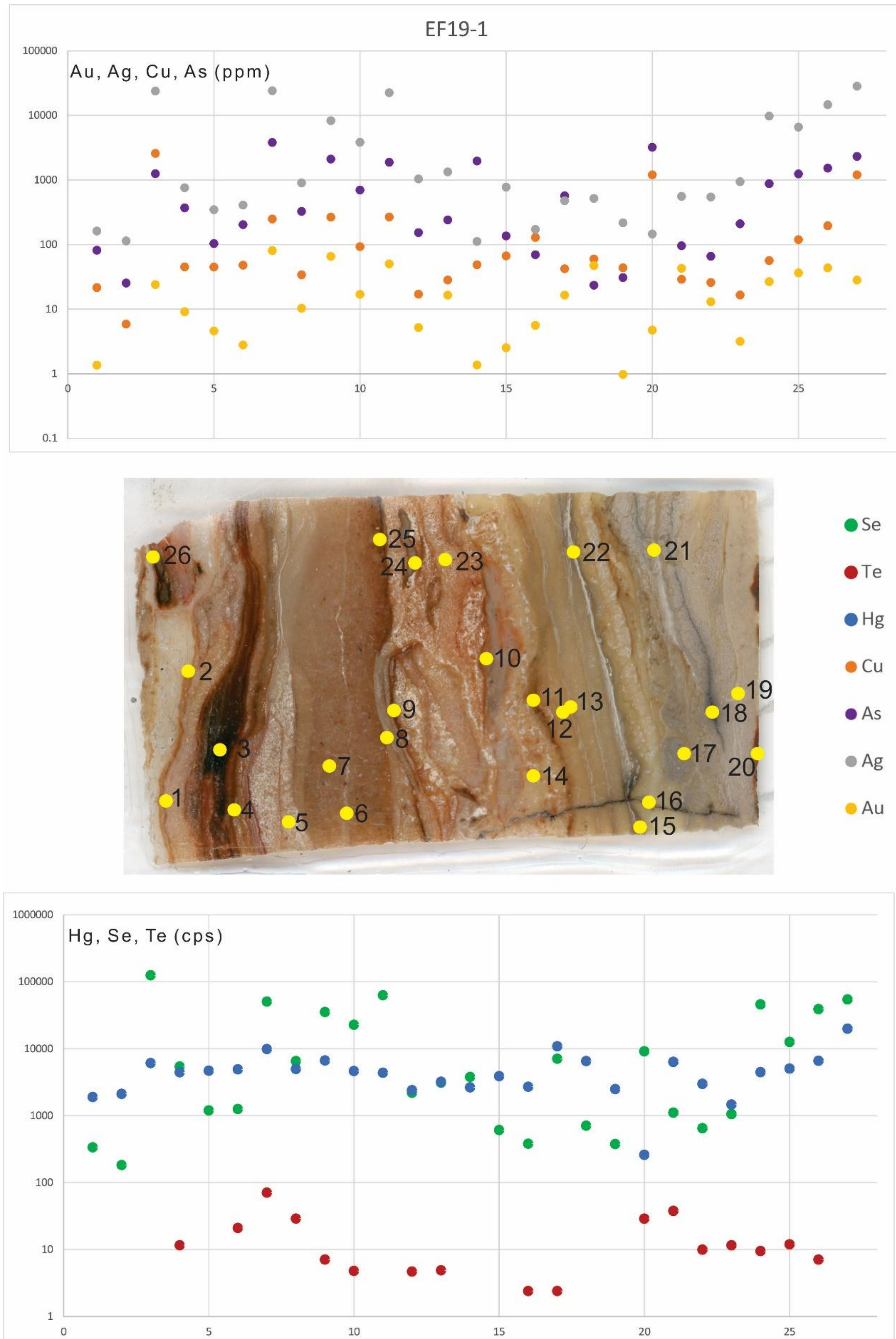

Figure 3.25: LA-ICP-MS spot analyses map image of proximal slope sample EF19-1 and data in ppm (above) and cps (below).

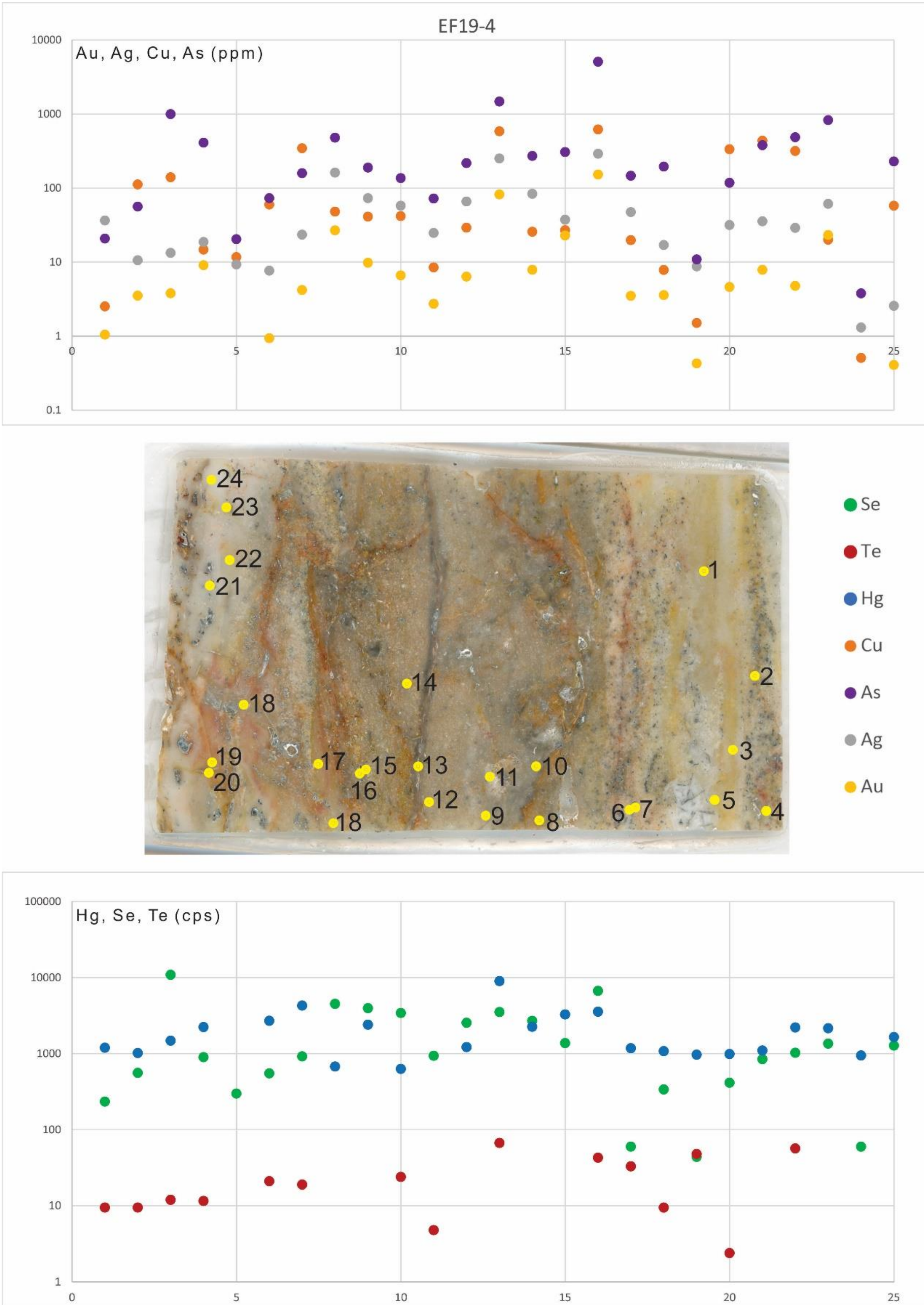

Figure 3.26: LA-ICP-MS spot analyses map image of mid-slope apron sample EF19-4 and data in ppm (above) and cps (below).

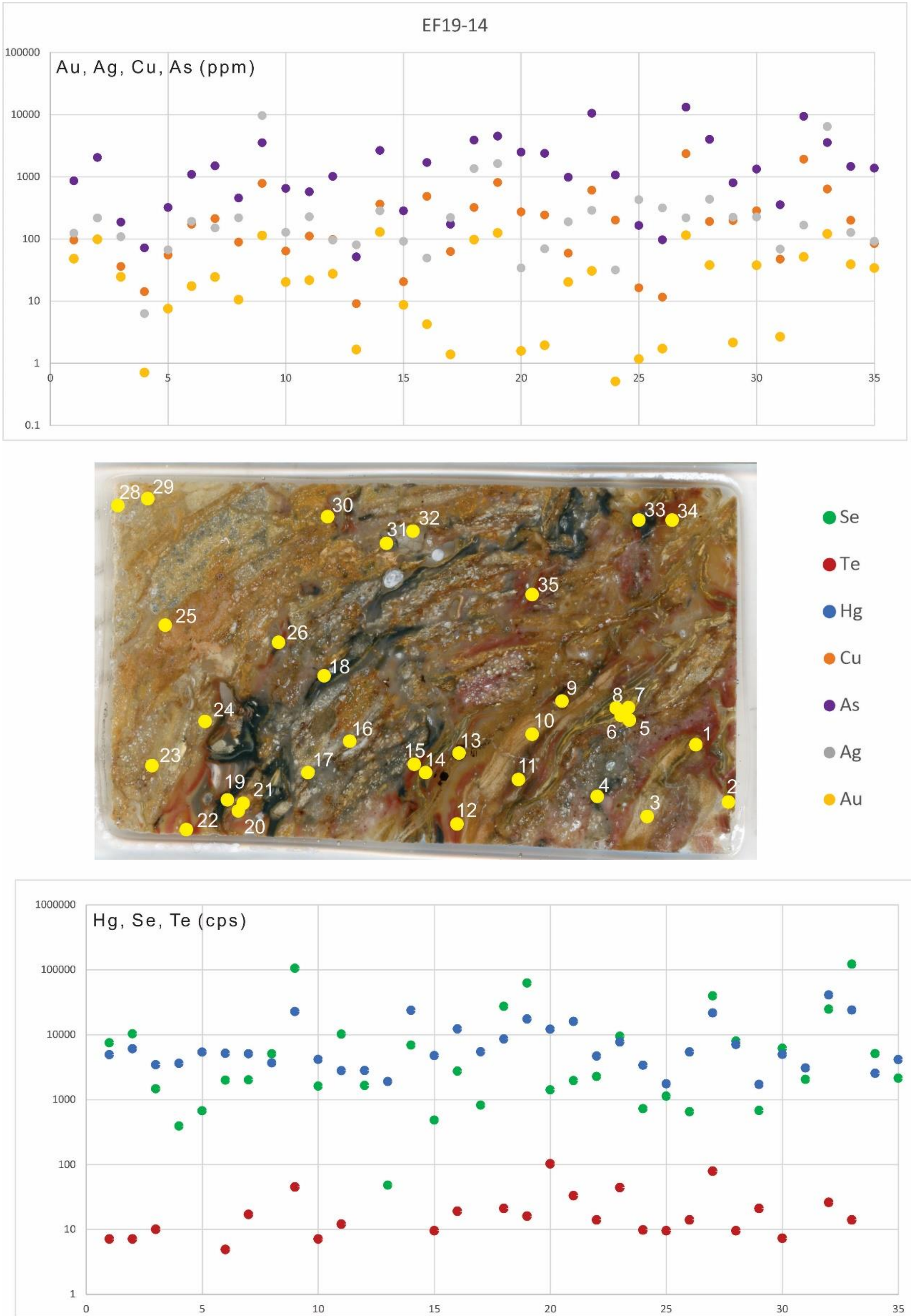

Figure 3.27: LA-ICP-MS spot analyses map image of mid-slope apron sample EF19-14 and data in ppm (above) and cps (below).

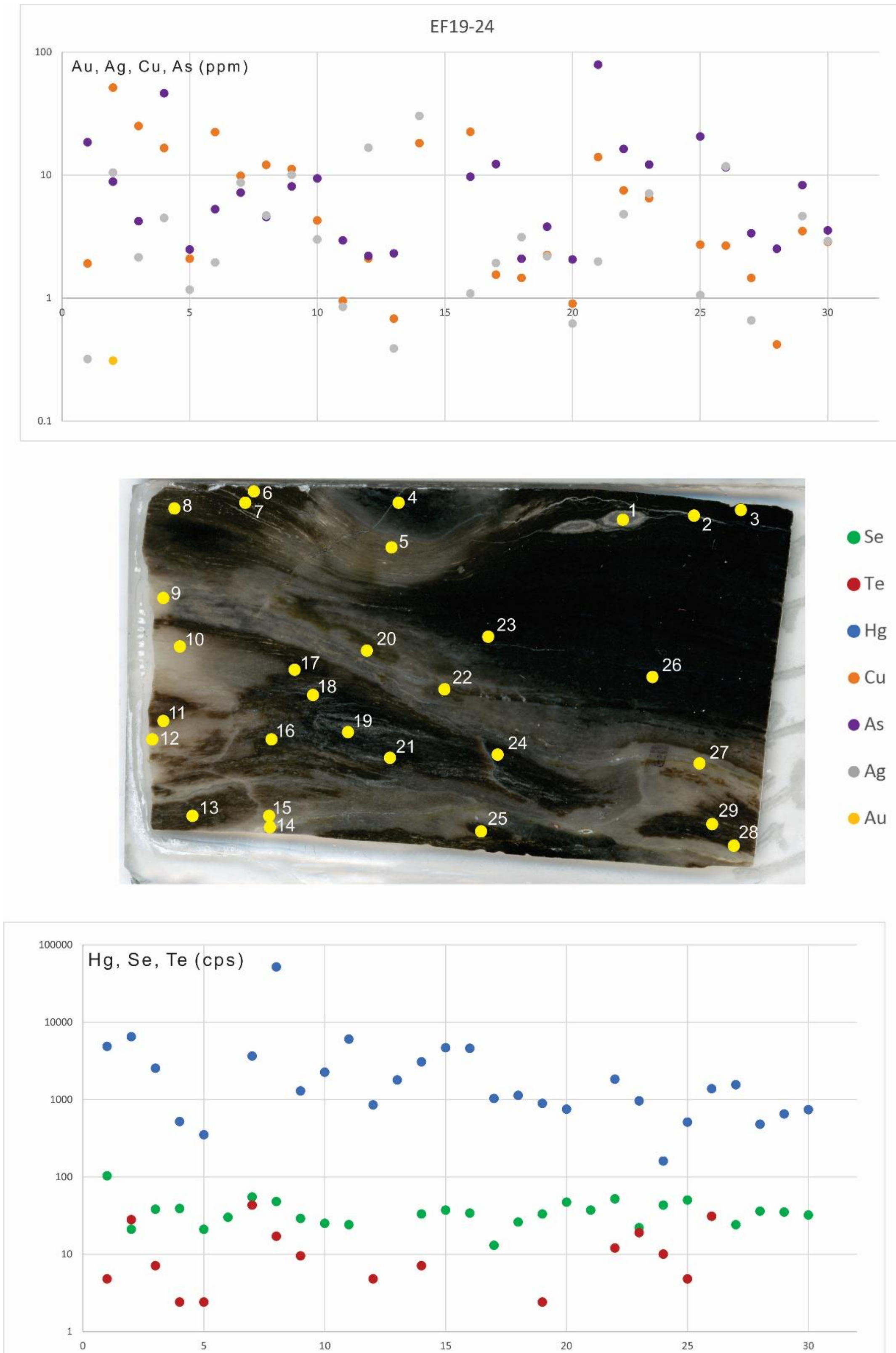

Figure 3.28: LA-ICP-MS spot analyses map image of distal slope/marsh sample EF19-24 and data in ppm (above) and cps (below).

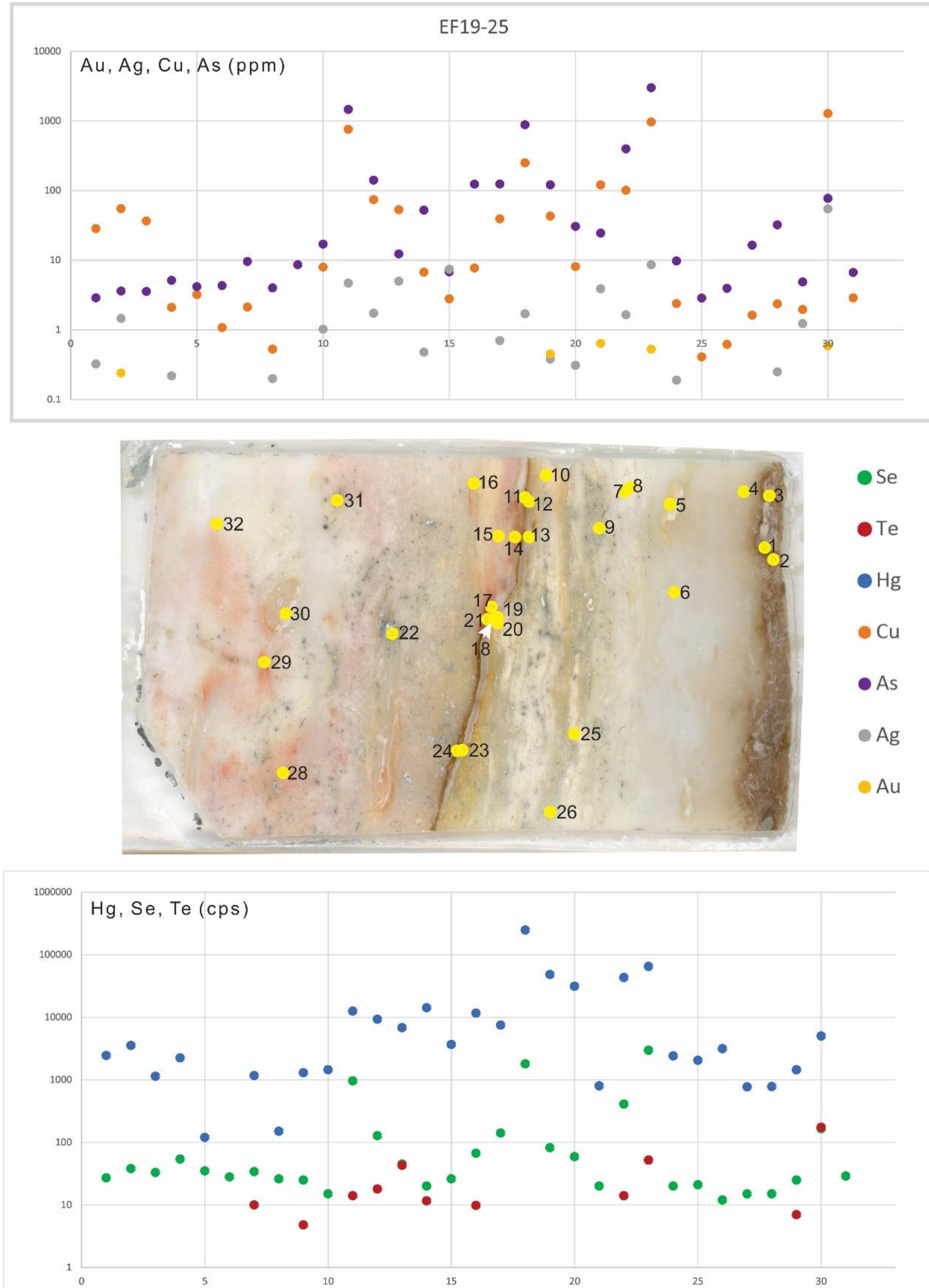

Figure 3.29: LA-ICP-MS spot analyses map image of Wagonwheel sample EF19-25 and data in ppm (above) and cps (below).

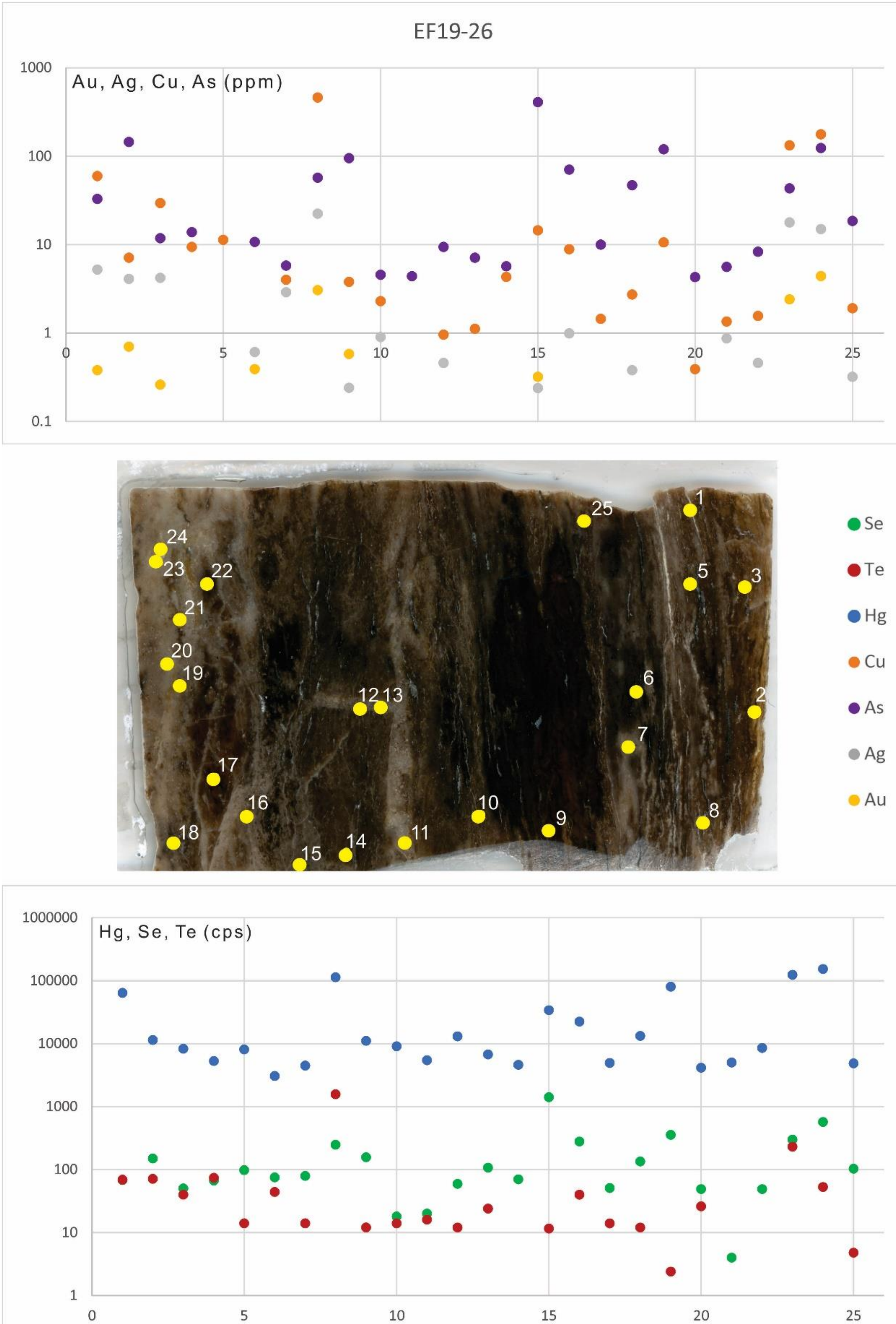

Figure 3.30: LA-ICP-MS spot analyses map image of distal slope/marsh EF19-26 and data in ppm (above) and cps (below).

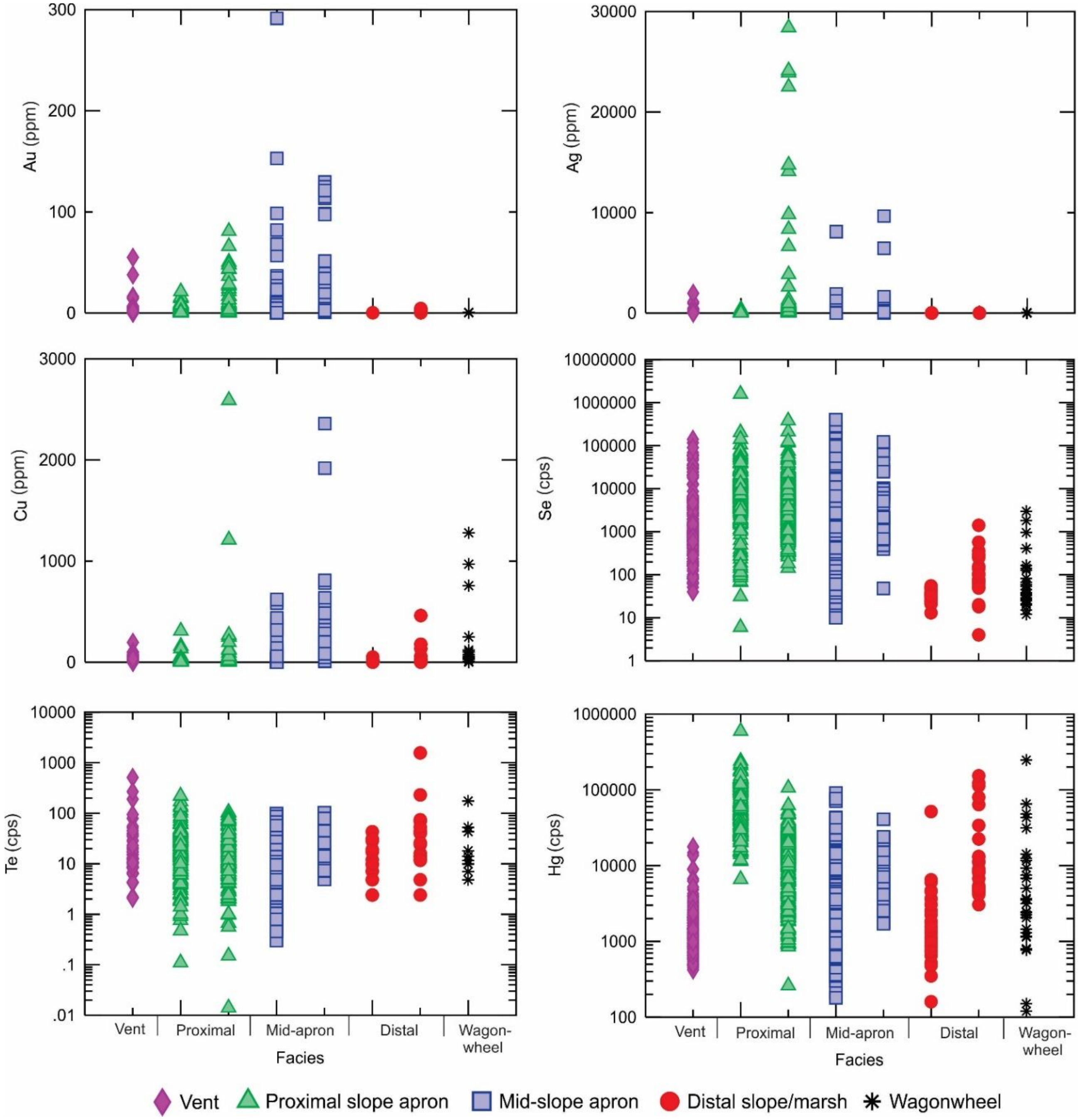

Figure 3.31: Graphical representation of metal(loid)s across the fluid pathway of Milestone. As distance from the vent increases (to the right), temperature decreases.

Chapter 4 - Discussion

History of the Main Knob and Paleosurface Formation:

Geologic mapping of the Main Knob (Fig. 3.1) suggests that the formation of the Main Knob likely began with a discharge silica-rich fluid flow that extended far across the knob, about 480m at its farthest, in the southeastern direction, creating a massive black sinter (e.g., stratigraphically lowest). This massive black sinter hosts of silicified plant life and was deposited across the knob, into the bottom of local topographic lows that existed across a rhyolite-lava-dominated paleosurface (Fig. 3.1). This initial phase was volumetrically the largest out of all observable facies due to the lateral extent. Based on the facies model of Hamilton et al. (2019), it should have higher temperature sinter equivalents that are now buried by younger deposits.

The next phase of the system was a high-volume phreatic eruption that deposited material laterally as far as ~50 m from the vent and created the matrix-supported breccia. As the eruption ceased, less clast-dominant material discharged to create facies of interbedded clast-dominant and fluid-dominant depositional bedding until silica-rich fluids took over as the main discharge. These fluids formed the bedded sinter and was the second longest phase temporally of the hydrothermal system based on the variety of samples and the overall thickness of the sinter facies. Additionally, this phase of discharge had to occur long enough to form an initial environment populated by thermophiles, which formed the bubble mats and stromatolites, much like the microbial mats that populate the Porcelain Basin in Yellowstone National Park (Fig. 4.1).

Eventually gases built up in the conduit, presumably from a decrease in the water table, and exploded upward and outward, creating the clast-supported breccia. We interpret that this violent eruption broke up the vent conduit and caused its collapse. Then, renewed silica discharge occurred and deposited sinter at the surface and silica infiltrate within the collapsed vent conduit. Geyserite was also deposited at the surface during this phase. First, geyserite eggs formed at the base of the vent. A calmer flow of fluid then pushed the eggs downslope and created a final coating of sinter. Nodular and specular geyserite were also deposited as the hot spring went through more vigorous expulsions of discharge around its vent. All features at the Main Knob are noted with relation to each facies, the vent, temperature formation, and where they lie on a typical schematic for paleosurface features (Fig. 4.2).

Textural, Elemental and Mineral Associations in Sinter:

Several textures indicative of boiling conditions have been observed in the sinter. Such textures include QAC, acicular quartz, and colloform banding. However, most visible occurrences of economic minerals (e.g., electrum) were found in the depositional flow of the siliceous fluids, rather than in veinlets created by a late-phase injection of fluid. Overall, the highest concentrations of metal(loid)s, particularly gold and silver (up to 153 ppm and 28400 ppm, respectively), are in the black and gray layers of the bedded sinter. Fluid flow formed the sluice box texture of electrum that is present in these deposits (Fig. 3.11). This textural evidence indicates that metal(loid) nanoparticles must have existed prior to their deposition on the surface, consistent with formation and aggregation of nanoparticles at depth due to boiling (Saunders, 2008, 2012; Saunders and Burke, 2017; Saunders et al., 2011b; 2019) and then subsequent transport of the nanoparticles onto the surface (Gartman et al., 2017; 2019; Saunders et al., 2019). This textural evidence is consistent with prior work that conclude the metals were derived from a co-existing magma (Saunders et al., 2015; Saunders and Burke 2017; Saunders et al., 2019).

The late-phase silica fluid brought forth a more sulfide-rich composition to the sinter as shown by the deposition and crystallization of pyrite in the secondary veinlet walls. Elements like Au, Ag, and Cu have higher concentrations in these veins in four samples (EF19-4, 6, 14, 25) than others with these veinlets. Many of the secondary veinlets that were analyzed have metal concentrations that are similar to or lower than those in the sinter that the veins crossed. The elevated levels of Al and K in all samples can be explained by the presence of argillically-altered rhyolite clasts included in the microbreccias of the sinters (Appendix B). Figures 4.3 and 4.4 plot selected metal(loid)s against Au and Ag, respectively. Across all samples, Au and Ag do not appear to have any significant relationship with elements that form economic minerals typically found in low-sulfidation epithermal deposits (selenides/tellurides/arsenides) (Figs. 4.3 and 4.4). Overall, the concentrations of Au, Ag, and Cu across the Main Knob are 0.027-153 ppm, 0.19-28400 ppm or 2.84 wt %, and 0.11-2590 ppm, respectively, showing that significant amounts of economic elements occur at this location. Albeit, the highest concentrations are within the black laminations rather than throughout the whole facies.

The variable elemental concentrations between individual sinter beds can be attributed to episodic phases of metal-rich and metal-poor discharge. The temperature of fluids affects the degree of mineralization and has been observed in hot spring environments by Sillitoe (2015), Hamilton et al. (2016), and Clark and Gemmell (2018). Precious and base metals are immobile in lower and ambient temperatures, and thus would precipitate out of solution closer to the vent and grade outwards. A good example of this is the Kohuamuri sinter in New Zealand, where the high to low gradation and zonation of elements from vent to marsh due to temperature changes aided in the identification of ore at depth (Hamilton et al., 2016). The concentrations of Au and Ag as a function of location across the Main Knob is depicted in Figures 4.5 and 3.31, in order to evaluate if there are any apparent changes in metal concentration with distance from the vent (e.g., along inferred flowpaths from the vent). Generally, what is observed is that there are high and low concentrations all across the area in no observable pattern relating to the geometry and facies-based temperature of the system. This suggests that the electrum nanoparticles formed at depth and were later deposited on the surface by the silica-rich fluids. Thus, the temperature of fluids at the surface did not play a role in the formation and deposition of precious metal(loids). They were instead transported from a deeper source to the surface and entrained in the fluid-flow across the Main Knob.

The primary textures observed at the Main Knob were chalcedony, calcite blades, amorphous silica, and electrum sluicebox textures. Late-phase textures include the QAC, comb quartz, jigsaw quartz, and silica/chalcedony veinlets. Chalcedony or amorphous silica needs to be exposed to higher temperatures of about 180°C (Fournier, 1989; Saunders, 1995; Moncada et al., 2012) for jigsaw quartz to form. The amorphous silica that makes up most of the sinter was most likely recrystallized to the jigsaw quartz while the superheated silica-saturated fluid was injected into the sinter at a temperature of over 180°C.

Milestone and Other Low-Sulfidation Deposits

The facies at the Main Knob of Milestone suggest an environment typical of a low-sulfidation hot spring. The most notable features in support of a low sulfidation hot spring deposit are the laminated sinter, bioformations, geyserite, explosion breccias, and silicified plant material (including large pieces of wood intermingled with the explosion breccia). What is observed at Milestone is similar to both present-day hot spring environments, and low-sulfidation epithermal deposits with mid-Miocene paleosurfaces in the Northern Great Basin as well. Ivanhoe and Midas are other significant mid-Miocene epithermal deposits within the Northern Great Basin that share a similar geologic history. Mid-Miocene magmatism occurred in all of these locations and the local magmas heated up meteoric water and it discharged along extensional faults (John et al., 2003; Wallace, 2003; Brueseke, 2010). Mercury-gold mineralization at Ivanhoe was coeval with local rhyolite domes and erupted through the extensional fault zones in the area (Wallace, 2003). The hydrothermal fluids associated with mineralization migrated to the surface and argillically altered local rhyolite lavas and tuffs. At Ivanhoe, the mercury deposits are in the sinter, and the gold lies within the underlying tuffs and subsurface vein deposits (Wallace, 2003). At its paleosurface, the sinter deposits at Ivanhoe contain surface vents, outflow breccias, parallel bedding, and massive sinter, similar to Milestone.

Midas is a low-sulfidation epithermal deposit located in the northern Nevada rift. Midas also formed in an extensional rifting environment that is associated with local bimodal basalt-rhyolite volcanism. Mafic dikes and sills, as well as silicic intrusions, populate the area through the structural weaknesses in the area caused by Basin and Range extension (John and Wallace, 2000; Leavitt et al., 2004). Propylitic alteration at Midas is also focused primarily around faults, veins, and the near-surface hot springs, while the argillic alteration is more developed in the host rocks, specifically rhyolite (Leavitt et al., 2004). Midas also hosts a sinter and silicified breccias and the sinter deposits and vents are also aligned with the north-northwest trending faults (Leavitt et al., 2004). Around the vent are brecciated material, laminated sinters, and silicified sediments (Leavitt et al., 2004)

It is also valid to compare Milestone to currently active low-sulfidation hot springs environments, such those found in Yellowstone National Park and the Taupo Volcanic Zone in New Zealand. In Yellowstone National Park, normal faults are related to regional extension and ring fractures adjacent to the Yellowstone caldera (Fournier, 1989; Morgan et al., 2017). Local hydrothermal activity is especially pronounced in these fault zones (Fournier, 1989). Siliceous sinters occur all across the park, but primarily in these normal fault zones, as hot spring pools, mounds, and terraces. Yellowstone contains numerous hot springs with all the same features found at Milestone (e.g., bioformations, sinter, clast-supported breccia, and geyserite) (Fig. 4.1). Furthermore, Beryl Spring, contains up to ~10 ppm gold in its discharging fluids (Fournier et al., 1994; Morgan et al., 2017).

The Taupo Volcanic Zone hosts relatively young (<340 ka) mineralized epithermal systems that are present in a portion of New Zealand that is undergoing intra- and back-arc rifting (Barker, 1993; Rowland and Simmons, 2015). There, rifting produced ~20 km-long arrays of N-NE trending normal faults (Rowland and Sibson, 2001; Rowland et al., 2010). The faults act as a series of structurally-controlled pathways for rising fluids. The Au-Ag mineralization and argillic alteration in the Taupo volcanic zone is associated with the structural weaknesses and fault-aligned eruptive centers in the rift basins, much like the Silver City District has rhyolite domes and mineralized areas localized on the normal faults in the Owyhee Mountains. The silicic vents have produced paleosurface features similar to those found on the Main Knob, such as eruption breccia, plant-rich fabrics, domal stromatolites, and wavy laminated sinter (Drake et al., 2014).

Milestone in the Silver City District:

Milestone is just northwest of the DeLamar mine, where notable epithermal deposits such as the North DeLamar, Glen Silver, and Sommercamp zones have been mined for silver and gold in the past several decades. The mineralization at Main Knob primarily exists in the laminated dark-colored beds of sinter (this study), and in the matrix-supported breccia (Barrett, 1985). Economic minerals at DeLamar and Florida Mountain are hosted in both veins, mineralized breccias, and porous rhyolite lava interiors (Lindgren, 1900; Bonnichesen, 1983; Mason, 2015; Gustin et al., 2019). Several major northwest trending faults, including the Northwest Fault, are the local structural pathways for rhyolite domes, sinter discharge, and epithermal deposits (Fig. 1.1). Mineralized areas such as Lucky Day, Twin Peaks, and Georgiana are located along these faults. Milestone is located just next to the Northwest Fault (Fig. 3.1). It is unclear whether Milestone formed before or after the faulting occurred. However, Halsor et al. (1983) suggested that the local rhyolite domes were emplaced along preexisting faults and followed by deposition of the Milestone sinter. Barret (1985) also reported the paleosurface as occurring after the faulting and rhyolite volcanism, consistent with rhyolite clasts in the Milestone breccias and the deposit overlying Silver City Rhyolite.

The rhyolite domes that have been classified as Silver City Rhyolite, which directly underlie the Milestone sinter, have been dated at 16.1 Ma by $^{40}Ar/^{40}Ar$ dating of sanidine (Brueseke and Hames, unpublished). Milestone was believed to have formed around the same time (Barret, 1985), but the sinter overlies the rhyolite. Adularia from epithermal veins from Florida Mountain and War Eagle Mountain have been dated at ~15.5-15.8 Ma (Aseto, 2012; Mason et al., 2015) and these cross-cut the rhyolite package. It is plausible that the hydrothermal system that formed Milestone was related to this same event, which affected much of the SCD at ~15.5 to 15.8 Ma.

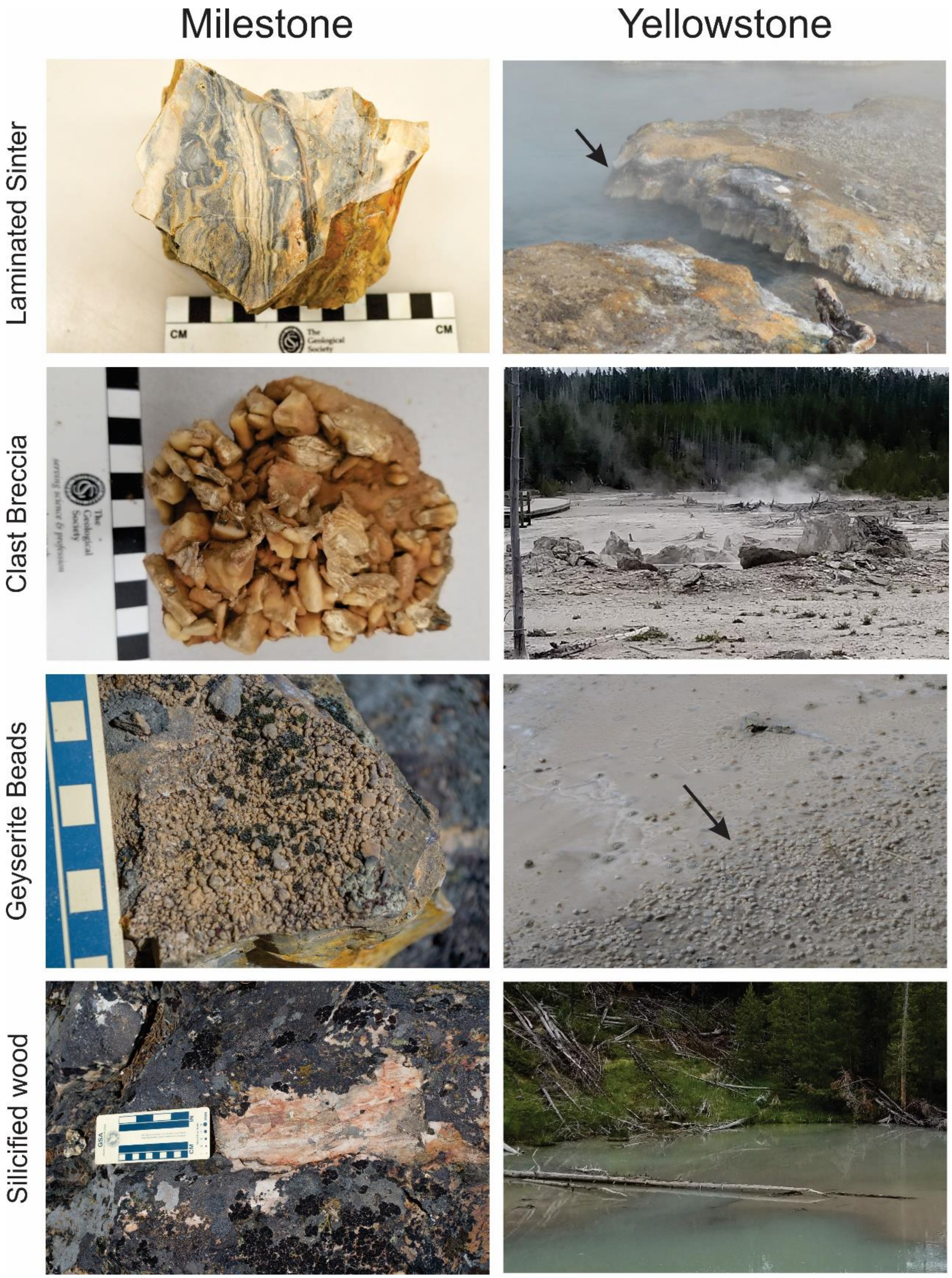

Figure 4.1: Comparison of hot spring features between Milestone and Yellowstone. From top to bottom: Laminated sinter from the Main Knob (left) and at Beryl Spring (right), clast-supported breccia from the Main Knob (left) and at Porcelain Basin (right), geyserite beads from the Main Knob (left) and at Porcelain Basin (right), silicified wood from the Main Knob (left), and at Porcelain Basin (right).

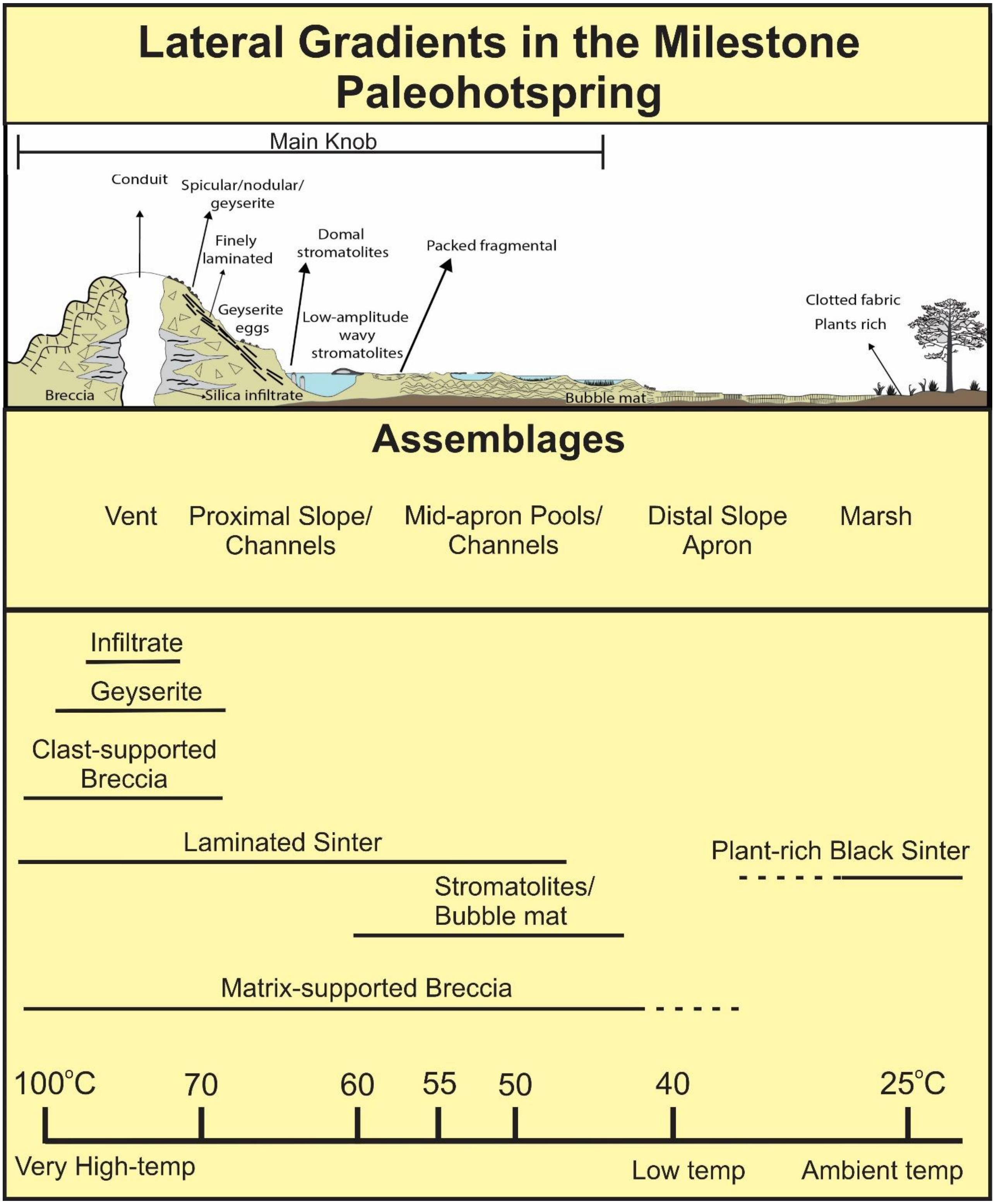

Figure 4.2: Paleosurface schematic for Milestone. The surface features are aligned with their geographic assemblages, the lithofacies defined in this study, and what temperature they formed under. Modified from Hamilton et al. (2019) to fit the observations at Milestone.

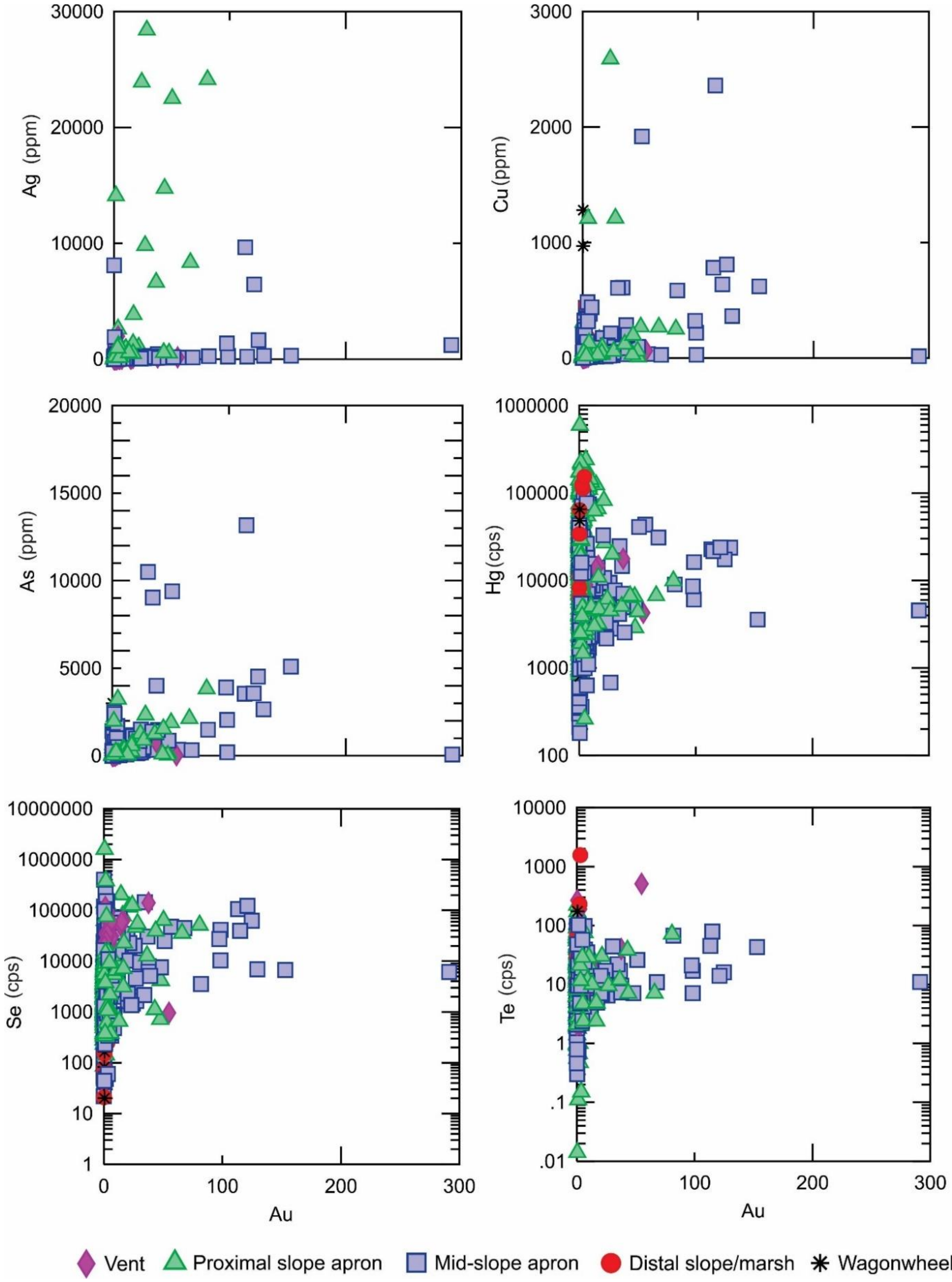

Figure 4.3: Data graphs of comparing elements commonly associated with low-sulfidation epithermal deposits against Au. Data points are organized into their slope location across Milestone.

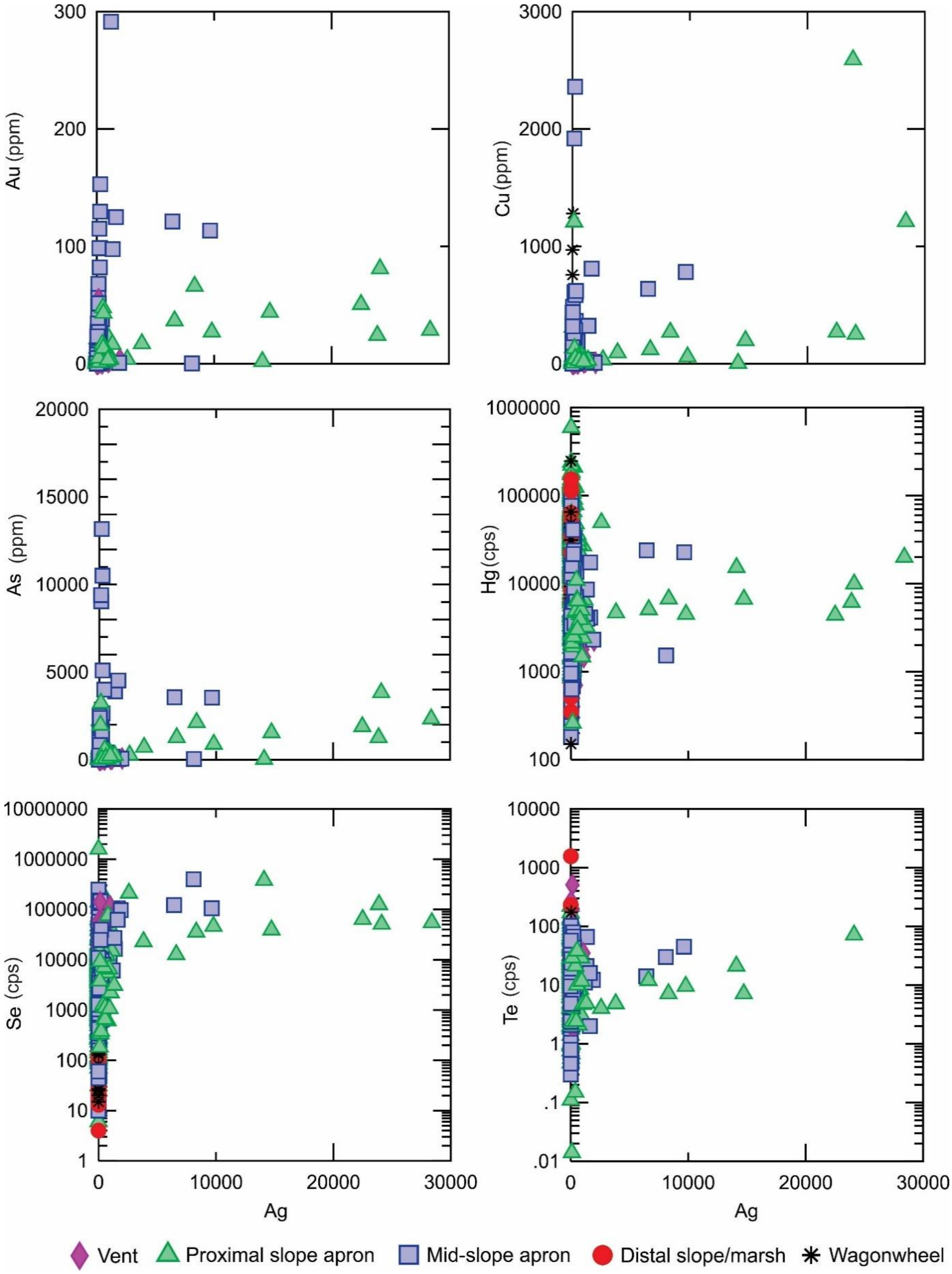

Figure 4.4: Data graphs comparing elements commonly associated with low-sulfidation epithermal deposits against Ag. Data points are organized into their slope location across Milestone.

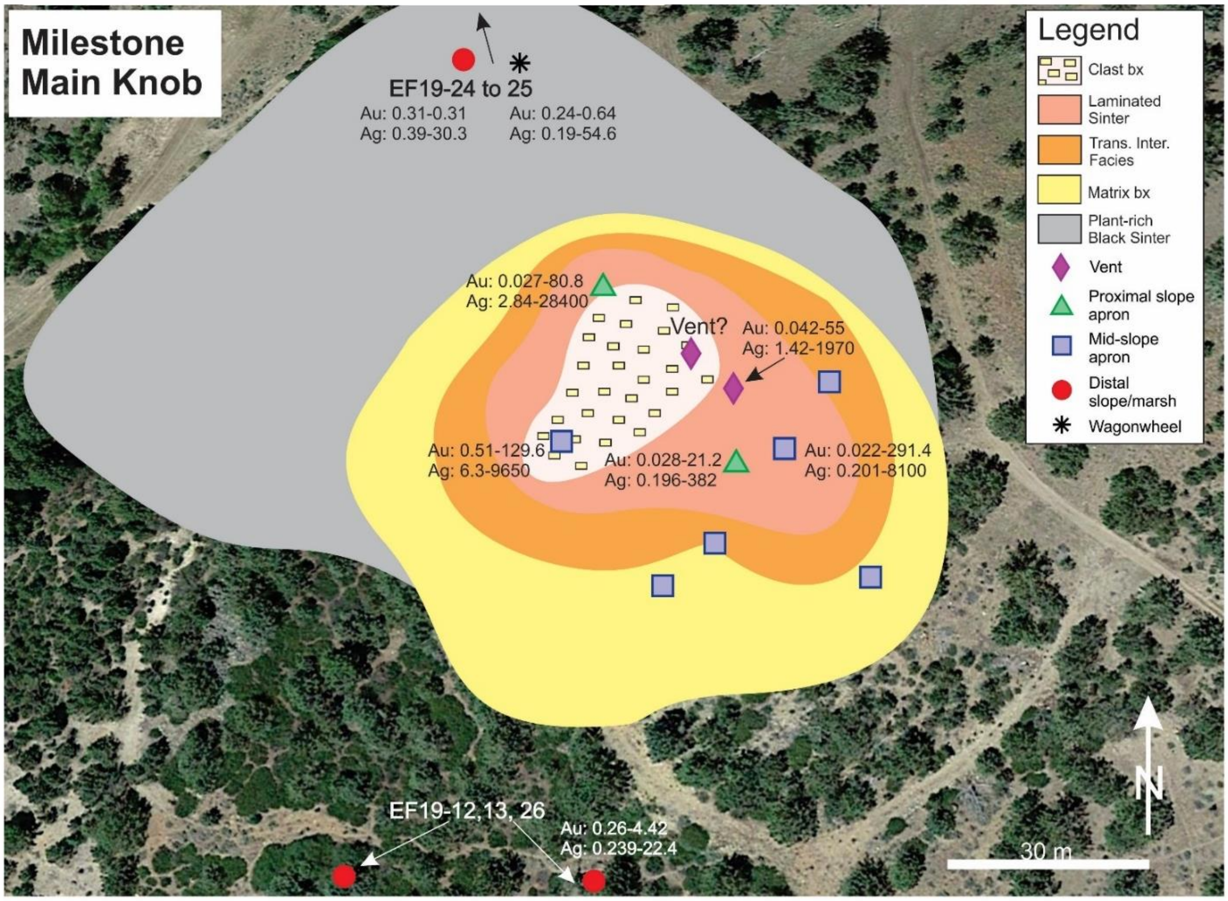

Figure 4.5: Map of sample locations at Milestone attributed with corresponding Au-Ag ranges (ppm).

Chapter 5 - Conclusions

Five lithofacies are present in the Milestone deposit Main Knob: Plant-rich black massive sinter, hydrothermal matrix-supported breccia, laminated sinter beds, clast-supported breccia, and geyserite. Other notable findings at Milestone include bioformations, channel scours, and the hydrothermal vent from which fluids (and explosions) were sourced. Two types of breccia exist at on the Main Knob, the matrix-supported breccia and the clast-supported breccia, representing two different eruption events. Built up pressure in the hydrothermal system injected a second-phase siliceous fluid into the sinter and ultimately resulted in a violent eruption that collapsed the vent. The paleosurface features found at the Milestone Main Knob are similar to those of typical hot springs that exist today.

Reflected Light Imaging revealed that deposition of electrum in thin laminations of black-colored sinter in both a sluice-box texture and possible thin dendrites. Other visible minerals in the sinter include euhedral to anhedral pyrite, anhedral pyrargyrite, and several textures of quartz (jigsaw, pseudo-acicular, quartz-after-calcite, comb quartz, colloform, and chalcedony). According to LA-ICP-MS transects and spot data, the black layers in the laminated sinter contain the highest ppm of trace metal(loids) (Figs. 3.18, 19, 23, 24, 27). There is no observable pattern of trace metal(loid)s with increasing distance from the inferred vent location, leading to the interpretation that micro and nanoparticles of economic minerals crystallized before being transported to the surface and deposited in the sinter.

Future Work

Based on the data collected, we suggest future drilling operations aim for the Main Knob itself and below. The identification of the hot spring vent and silica infiltrate at the surface, as well as textures that are consistent with boiling, are likely indications that precious metal-rich veins exist at depth. Given the presence of metal(loid) nanoparticles in the sinter, they are likely present, in veins, below the deposit. Typical vein formation in epithermal deposits is about 150-300 m in depth, therefore we assume the highest concentration of metal(loid)s to exist within this window.

Although few fluid inclusions were identified in the secondary silica veinlets, there is potential for fluid inclusion analysis to constrain the temperatures of these veinlets. It is suspected that vein or veinlets at depths may contain a higher population of inclusions. The use of O isotopes could also be useful to identify the fluid and metal source of the injection and depositional sinter fluid. Additionally, if any adularia (or other suitable K-rich phase) is discovered in the hot spring deposits, an age can be calculated using $^{40}Ar/^{39}Ar$ dating to confirm the absolute age of the deposit. A bulk XRD analysis of sinter could confirm the presence of adularia, as well as the different silica phases (e.g., opal-types), and overall bulk mineralogy of the deposit facies.

References

Aseto, C.O., 2012, Geology, geochemistry, and geochronology of low-sulfidation epithermal Au-Ag ores on War eagle Mountain, Silver City District, Idaho: Unpublished M.S. thesis, Auburn University.

Barker, R., 1993, The history of epithermal gold-silver exploration in the Taupo Volcanic Zone: New Zealand Mining, v. 12, p. 15–19.

Barrett, R., 1985, The geology, mineralization, and geochemistry of the milestone hot-spring silver-gold deposit near the Delamar silver mine, Owyhee county, Idaho. *University of Idaho*, M.S. thesis.

Bonnichsen, B, 1982, Chemical composition of the cougar point tuff and rhyolite lava flows from the Bruneau-Juarbidge eruptive center, Owyhee County, Idaho. *Idaho Geological Survey*, Moscow, Idaho.

Bonnichsen, B., 1983, Epithermal gold and silver deposits Silver City-Delamar district, Idaho. *Idaho Geological Survey*, Moscow, Idaho.

Brueseke, M.E., Heizler, M.T., Hart, W.K., Mertzman, S.K., 2007, Distribution of Oregon Plateau (U.S.A.) flood basalt volcanism: The Steens Basalts revisited: *Journal of Volcanology and Geothermal Research*, v. 161, p. 187–214.

Brueseke, M.E., and Hart, W.K., 2008, Geology and petrology of the mid-Miocene Santa Rosa-Calico volcanic field, northern Nevada: *Nevada Bureau of Mines and Geology,* Bullletin 113.

Brueseke, M.E., 2010, Magmatism and mineralization in the Oregon Plateau and northern Great Basin: Mid-Miocene volcanism and associated bonanza ore deposits and their relations to the inception of the Yellowstone hotspot, *Geological Society of Nevada*.

Camp, V.E., Ross, M.E., 2004, Mantle dynamics and genesis of mafic magmatism in the intermontane pacific northwest, *Journal of Geophysical Research*, v. 109, doi: 10.1029/2003JB002838.

Chang, Z, Hedenquist JW, White NC, Cooke DR, Roach M, Deyell CL, Garcia J Jr, Gemmell JB, McKnight S, Cuison AL (2011) Exploration tools for linked porphyry and epithermal deposits: example from the Mankayan intrusion-centered Cu-Au district, Luzon, Philippines, Economic Geology, v. 106, p. 1365–1398.

Clark, L.V., and Gemmell, J.B., 2018, Vein stratigraphy, mineralogy, and metal zonation of the Kencana low-sulfidation epithermal Au-Ag deposit, Gosowong Goldfield, Halmahera island, Indonesia, *Economic Geology*, v. 113, p. 209–236. doi: 10.5382/econgeo.2018.4549

Drake, B.D., Campbell, K.A., Rowland, J.V., Guido, D.M., Browne, P.R.L., Rae, A., 2014, Evolution of a dynamic paleo-hydrothermal system at Mangatete, Taupo Volcanic Zone, New Zealand, *Journal of Volcanology and Geothermal Research*, v. 282, p. 19-35, doi: 10.1016/j.jvolgeores.2014.06.010.

Ekren, E.B., McIntyre, D.H., Bennett, E.H., and Malde, H.E., 1981, Geologic map of Owyhee County, Idaho, west of longitude 116˚W. *U.S. Geological Survey*, Map 1-1256.

Ekren, E.B., McIntyre, D.H., Bennett, E.H., and Marvin R.F., 1982, Cenozoic stratigraphy of western Owyhee County, Idaho, in Bonnichsen, B. and Breckenridge, R.M., eds., Cenozoic Geology of Idaho, *Idaho Bureau of Mines and Geology*, Bulletin 26

Fournier, R.O., 1989, Geochemistry and dynamics of the Yellowstone National Park hydrothermal system, Annual Review of Earth Sciences, U.S. Geological Survey, v. 17, p. 13-53.

Fournier, R.O., Kennedy, B., Mack, A.M., and Thompson, J.M., 1994, Correlation of gold in siliceous sinters with 3He/4He in hot spring waters of Yellowstone National Park: *Geochimica et Cosmochimica Acta*, v. 58, p. 5401–5419.

Gartman, A., Hannington, M., Jamieson, J.W., Peterkin, B., Garbe-Schönberg, D., Findlay, A.J., Fuchs, S., Kwasnitschka, T., 2017, Boiling-induced formation of colloidal gold in black smoker hydrothermal fluids. *Geology*, v. 46, p. 39–42.

Gartman, A, Findlay AJ, Hannington M., Garbe-Schönberg, D., Jamieson, J. W., Kwasnitschka, T., 2019, The role of nanoparticles in mediating element deposition and transport in hydrothermal vents, *Geochim Cosmochim Acta*, v. 231, p. 113–131.

Guido, D.M., and Campbell, K.A., 2019, Plastic silica conglomerate with an extremophile microbial matrix in a hot-water stream paleoenvironment, *Astrobiology*, v. 19, p. 1433-1441, doi: 10.1089/ast.2018.1998.

Gustin, M.M., Weiss, S.I., 2017, Technical report and resource estimate, Delamar gold-silver project, Owyhee County, Idaho, USA. *Mine Development Associates*, Integra Resources Corp.

Gustin, M.M., Weiss, S.I., McPartland, J.S., 2019, Technical report and updated resource estimate for the Delamar and Florida Mountain gold-silver project, Owyhee County, Idaho, USA. *Mine Development Associates*, Integra Resources Corp.

Halsor, S., 1983, A volcanic dome complex and DeLamar silver mine, Owyhee County, Idaho, *Michigan Technological University*, M.S. thesis.

Halsor, S.P., Bornhorst, T.J., Beebe, M., Richardson, K., and Strowd, W., 1988, Geology of the DeLamar silver mine, Idaho – A volcanic dome complex and associated hydrothermal system. *Economic Geology*, v. 83, p. 1159-1169.

Hamilton, A., Campbell, K., Rowland, J., Browne, P., The Kohuamuri siliceous sinter as a vector for epithermal mineralization, Coromandel Volcanic Zone, New Zealand, *Miner Deposita*, doi: 10.1007/s00126-016-0658-8.

Hamilton, A.R., Campbell, K.A., Guido, D.M., 2019, Atlas of siliceous hot spring deposits (sinter) and other silicified surface manifestations in epithermal environments, *GNS Science*, v. 56, doi: 10.21420/BQDR-XQ16

Hames, W., Unger, D., Saunders, J., Kamenov, G., 2009, Early Yellowstone hotspot magmatism and gold metallogeny, *Journal of Volcanology and Geothermal Research*, v. 188, pp. 214-224.

Hasten, Z., 2012, Mid-Miocene magmatism in the Owyhee Mountains, ID: Origin and petrogenesis of volcanic rocks in the Silver City District, *Kansas State University*, M.S. thesis.

Hasten, Z., Brueseke, M., Saunders, J., and Hames, W., 2012, Mid-Miocene volcanism in the Owyhee Mountains (ID) and implications for coeval epithermal precious metal mineralization: *Geochimica et Cosmochimica Acta*, Goldschmidt Conference Abstracts, 2012.

Hedenquist, J.W., Lowenstern, J.B., 1994, The role of magmas in the formation of hydrothermal ore deposits, *Nature*, v. 370, p. 519-527.

Heinrich, C.A., Günther D., Audétat A., Ulrich T., and Frischknecht R., 1999, Metal Fractionation between magmatic brine and vapor, determined by microanalysis of fluid inclusions: *Geology*, v. 27, p. 755-758.

Jochum, K.P., Wilson, S.A., Abouchami, W., Amini, M., Chmeleff, J., Eisenhauer, A., Hegner, E., Iaccheri, L.M., Kieffer, B., Krause, J., McDonough, W.F., 2011, GSD-1G and MPI-

DING reference glasses for in situ and bulk isotopic determination, *Geostandards and Geoanalytical Research*, v. 35, p. 193-226, doi: 10.1111/j.1751-908X.2010.00114.x

John, D.A., 2001, Miocene and early Pliocene epithermal gold-silver deposit in the Northern Great Basin, western United States: Characteristics, distribution, and relationship to magmatism, *Economic Geology*, v. 96, p. 1827-1853.

John D.A., Hofstra, A.H., Fleck, R.J., Brummer, J.E., Saderholm, E.C., 2003, Geologic setting and genesis of the Mule Canyon low-sulfidation epithermal gold-silver deposit, north-central Nevada, *Economic Geology*, v. 98, p. 425-463.

Kamenov, G.D., Saunders, J.A., Hames, W.E., Unger, D.L., 2007, Mafic magmas as sources for gold in middle Miocene epithermal deposits of the Northern Great Basin, United States: Evidence from Pb isotope compositions of native gold, *Economic Geology*, v. 102, pp. 1191-1195, doi: 0361-0128/07/3696/5/5-1191.

Leavitt, E. D., Spell, T. L., Goldstrand, P. M., and Arehart, G. B., Geochronology of the Midas low-sulfidation epithermal gold-silver deposit, Elko County, Nevada, *Economic Geology*, v. 99, p. 1665-1686, doi: 0361-0128/01/3475/1665-22.

Lindgren, W., 1900, The gold and silver veins of the Silver City, De Lamar, and other mining districts in Idaho. *U.S. Geological Survey 20th Annual Report*, Part 3, p. 65-256.

Liu, Y.S., Hu, Z.C., Li, M., and Gao, S., 2013, Applications of LA-ICP-MS in the elemental analyses of geological samples: Chinese Science Bulletin, *Geochemistry*, v. 58, p. 3863-3878, doi: 10.1007/s11434-013-5901-4.

Lynne, B. Y., 2012, Mapping vent to distal-apron hot spring paleo-flow pathways using siliceous sinter architecture, *Geothermics*, v. 43, p. 3-24, doi: 10.1016

Marshall, D., Anglin, C. D., and Mumin H., 2011, Ore mineral atlas, 2nd edition, *Geological Association of Canada – Mineral Deposists Division*, Newfoundland, Canada.

Mason, M.S., Saunders, J.A., Aseto, C., Hames, W.E., and Brueseke, M.E., 2015, Epithermal Au-Ag ores of War Eagle and Florida Mountains, Silver City district, Owyhee County, Idaho: in Pennell, W.M., and Garside, L.J., eds., Proceedings of the Geological Society of Nevada Symposium, *New Concepts and Discoveries*, Reno, p. 1067-1078.

Maynard, A.M., Brueseke, M.E., and Mathur, R.M., 2015, Copper isotope compositions of Cenozoic mafic rocks from the northern Great Basin and Snake River Plain (USA): Geological Society of America Abstracts with Programs, v. 47.

Moncada, D., Mutchler, S., Nieto, A., Reynolds, Rimstidt, J.D., Bodnar, R.J., 2012, Mineral textures and fluid inclusion petrography of the epithermal Au-Ag deposits at Guanajuato, Mexico: Application to exploration, Journal of Geochemical Exploration, v. 114, p. 20-35.

Morgan, L.A., Shanks, W.C.P., Lowenstern, J.B., Farrell, J.M., Robinson, J.E., Geologic field-trip guide to the volcanic and hydrothermal landscape of the Yellowstone Plateau, *U.S. Geological Survey Scientific Investigations* Report 2017–5022–P, p. 100, doi: 10.3133/sir20175022P.

Norman, M.D., Leeman, W.P., 1989, Geochemical evolution of Cenozoic-Cretaceous magmatism and its relation to tectonic setting, southwestern Idaho, U.S.A., *Earth and Planetary Science Letters,* v. 94, p. 78-96.

Norton, D.L., 1982, Fluid and heat transport phenomena typical of copper-bearing pluton environments, *Advances in geology of the Porphyry Copper Deposits of Southwestern North America*, University of Arizona Press, p. 59-72.

Pansze, A.J., 1975, Geology and ore deposits of the Silver City-De Lamar-Flint Region Owyhee County Idaho, Idaho Bureau of Mines and Geology, no. 161.

Paton, C., Hellstrom, J., Paul, B., Woodhead, J., Hergt, J., 2011, Iolite: freeware for the visualisation and processing of mass spectrometric data, *Journal of Analytical Atomic Spectrometry,* v. 26, p. 2508-2518, doi: 10.1039/C1JA10172B

Richards, J.P., 2009, Postsubduction porphyry Cu-Au and epithermal Au deposits: Products of remelting of subduction-modified lithosphere, *Geology*, v. 37, 247-250, doi:10.1130/G25451A.1

Ridley, J., 2016, Ore deposit geology, *Cambridge University Press*, ISBN 978-1-107-02222-5.

Rowland, J.V., and Sibson, R.H., 2001, Extensional fault kinematics within the Taupo Volcanic Zone, New Zealand: Soft-linked segmentation of a continental rift system, *New Zealand Journal of Geology and Geophysics,* v. 44:2, p. 271-283, doi: 10.1080/00288306.2001.9514938

Rowland, J.V., and Simmons, S.F., 2005, Tectonic controls on the epithermal ore-forming environment, northern New Zealand, p. 695-704.

Rowland, J.V., Wilson, C.J.N., Gravley, D.M., 2008, Spatial and temporal variations in magma-assisted rifting, Taupo Volcanic Zone, New Zealand, *Journal of Volcanology and Geothermal Research*, v. 190, p. 89-108.

Rowland, J.V., Wilson, C.J.N., Gravley, D.M., 2010, Spatial and temporal variations in magma-assisted rifting, Taupo Volcanic Zone, New Zealand, *Journal of Volcanology and Geothermal Research*, v. 190, p. 89-108, doi: 10.1016/j.jvolgeores.2009.05.004.

Sawkins, F.J., 1990, Metal deposits in relation to plate tectonics, *Springer-Verlag*, 2nd edition.

Saunders, J.A., Unger, D.L., Kamenov, G.D., Fayek, M., Hames, W.E., Utterback, W.C., 2008, Genesis of middle Miocene Yellowstone hotspot-related bonanza epithermal Au-Ag depostits, Northern Great Basin, USA, *Miner Deposita*, doi: 10.1007/s00126-008-0201-7

Saunders, J. A., Kamenov, G.D., Hofstra, A.H., Unger, D.L., Creaser, R.A., Barra, F., 2010, "Forensic" geochemical approaches to constrain the source of Au-Ag in low-sulfidation epithermal ores, *Great Basin Evolution and Metallogeny*, pp. 693-700.

Saunders, J.A., Vikre, P., Unger, D.L., Beasley, L., 2011b, Colloidal and physical transport textures exhibited by electrum and naumannite in bonanza epithermal veins from western USA, and their significance. *Great Basin Evolution and Metallogeny Symposium Proceedings*, Geological Society of Nevada, Reno-Sparks, NV, USA, p. 825–832.

Saunders, J.A., 2012, Textural evidence of episodic introduction of metallic nanoparticles into bonanza epithermal ores, *Minerals,* v. 2, p. 228–243.

Saunders, J.A., and Brueseke, M.E., 2012, Volatility of Se and Te during subuction-related distillation and the geochemistry of epithermal ores of the western United States, *Economic Geology*, v. 107, pp. 165–172.

Saunders, J.A., Kamenov, G.D., Mathur, R., Shimizu, T., Brueseke, M.E., 2013, Transport and deposition of metallic nanoparticles and the origin of bonanza epithermal ores, *Society of Geology applied to Mineral deposits*, Biennial SGA Proceedings, Uppsala, Sweden, in press.

Saunders, J.A., Hofstra, A.H., Goldfarb, R.J., and Reed, M.H., 2014, Geochemistry of Hydrothermal Gold Deposits, In: Holland H.D. and Turekian K.K. (eds.) Treatise on Geochemistry, Second Edition, Elsevier, v. 13, p. 383-424.

Saunders, J.A., Mathur, R., Kamenov, G.D., Shimizu, T., Brueseke, M. E., 2015, New isotopic evidence bearing on bonanza (Au-Ag) epithermal ore-forming processes. *Miner Deposita*. doi 10.1007/s00126-015-0623-y.

Saunders, J.A., and Burke, M., 2017, Formation and aggregation of gold (electrum) nanoparticles in epithermal ores, *Minerals,* v. 7, p. 1-11, doi:10.3390/min7090163.

Saunders, J.A., Burke, M., Brueseke, M.E., 2019, Scanning-electron-microscope imaging of gold (electrum) nanoparticles in middle Miocene bonanza epithermal ores from northern Nevada, USA, *Mineralium Deposita*, v. 55, p. 389-398, doi: 10.1007/s00126-019-00935-y

Sillitoe, R.H., 2015, Epithermal paleosurfaces, *Miner Deposita*, v. 50, p. 767-793, doi: 10.1007/s00126-015-0614-z.

Sillitoe, R.H., Hedenquist, J.W., 2003, Linkages between volcanotectonic settings, ore-fluid compositions, and epithermal precious metal deposits, *Society of Economic Geologists*, v.10, p. 1-24.

Streck, M.J., 2014, Evaluation of crystal mush extraction models to explain crystal-poor rhyolites, *Journal of Volcanology and Geothemal Research*, v. 284, p. 79-94

Tămaş C.G., and Milési, J.P., 2003, Hydrovolcanic breccia pipe structures—general features and genetic criteria—I. Phreatomagmatic breccias. Geologia, v. 1. P. 127-147, doi: 10.5038/1937-8602.47.1.10.

Taylor H.P., 1979, Oxygen and hydrogen isotope relationships in hydrothermal mineral deposits. *Geochemistry of hydrothermal ore deposits*, 2nd ed., p. 236–277.

Vikre, P.G., 2007, Sinter-vein correlations at Buckskin Mountain, National District, Humboldt County, Nevada. Society of Economic Geologists, Inc. *Economic Geology*, v. 102, p. 193-224.

Wallace, A.R., 2003, Geology of the Ivanhoe Hg-Au district, northern Nevada: Influence of Miocene volcanism, lakes, and active faulting on epithermal mineralization, *Economic Geology*, v. 98, p. 409-424.

White, D.E., Heropoulos, C., and Fournier, R.O., 2001, Gold and other minor elements associated with the hot springs and geysers of Yellowstone National Park, Wyoming, Supplemented with data from Steamboat Springs, Nevada, *U.S. Geological Survey Bulletin* 2001.

Wilkinson, J.J., 2001, Fluid inclusions in hydrothermal ore deposits, *Lithos*, v. 55, p. 229-272.

Appendix A - Thin Section Descriptions

Descriptions occurred right when K-State was shutting down campus operations due to the 2020 COVID-19 pandemic. Thus, more detailed thin section descriptions, including crystal size measurements, were unable to occur because of the reflected light microscopy lab shutdown.

EF19-1:

Layered mosaic quartz, contains QAC with quartz crystals growing in the void as comb quartz. Sinter is more massive than mosaic. Most of the sinter beds contain rounded silicified fragments. Much of the bedding has oxidation staining. Sluice-box textures occur in three different layers. Veinlets that cut across the sinter perpendicularly. Minor jigsaw quartz is the infill of the veins. Much of the sinter contains hematite, and could explain the red color and oxidation staining. Any gold/pyrite is finely disseminated in brown/black sinter.

EF19-3:

Much of this sample has oxidation staining. Gray and light brown beds dominate the sinter portion of this sample. The other half of this sample consists of a matrix-supported breccia with shadows of rounded clasts. The clasts have been silicified so that that majority of this area is made up of massive quartz. Quartz after calcite formations are smaller compared to QAC formations in the other samples. Two sub-rounded grains of pyragyrite are found near a vein of quartz. Veins in this sample are filled in by comb quartz.

EF19-4:

This sample consists of massive sinter with alternating bands of tan, white, black, and reddish brown. Some layers are more distinct than others. Disseminated gold/pyrite in distinct sinter layers, primarily the reddish-brown layers, lots of QAC with crystallized quartz in the voids. A flood of sinter filled in other voids from the QAC. Much of the fluid includes silicified clasts that have been brecciated and transported. Brecciated/QAC areas are more jigsaw quartz, and the sinter is more massive/rock flour texture.

EF19-5:

Alternating bands of brown, black, gray, and white sinter, partially deformed by injections. The whiter the layer, the less gold. Massive quartz mosaic, veinlets of injected quartz which brecciate preexisting sinter in the process. The top of the layers contains the finest quartz, and the size grades downwards. Impurities are settled at the top of the sinter layer. Major voids in the sinter are filled by quartz after calcite formations. Disseminated gold occurs in gray/black layers, no more than 5microns in size.

EF19-6:

Massive sinter with jigsaw quartz occupying the very few veinlets that cross perpendicular to the apparent bedding. Three bands contain entrained silicified and rounded fragments. Fragments could be pieces of feldspar. They have yellowish colors in xpl. About 90% of the fragments have been completely silicified. Two anhedral red crystals are found in this sample could be arsenopyrite, but it is difficult to distinguish.

EF19-7:

Massive amorphous quartz makes up this sample with alternating bands of gray, red, tan, and black sinter. Disseminated gold is in gray layer, few clusters of gold particles more concentrated in the top of the gray sinter, where it is almost black. Thicker bands of sinter have minor amounts of jigsaw quartz, as if it were just starting to recrystallize. Gold particles in a reddish layer coat a clast of albite. A significant amount of gold is present in the thin black layer, and is more disseminated in top red layer. This black layer exhibits a sluicebox texture. Rust-colored oxidation stains coat some sinter layers. Everything is completely silicified with small entrained clasts that are also oxidized. The brecciated portion is mostly QAC with comb quartz crystallized in the empty space.

EF19-8:

Amorphous silica is the dominant phase. Alternating bands of wavy tan, white, and black sinter characterize this sample. The thinner black layer has sluicebox textures where electrum is concentrated at the outermost layer, and become more disseminated below. This could be interpreted as branches of a dendritic crystal cut perpendicularly across the outer branches.

Above the thinnest black layer are quartz after calcite formations with comb quartz growing into the open spaces. The other colored bands of sinter contain both electrum and oxidized sub-rounded grains of pyrite, which gives the beds a rusted orange color. The rest of the sinter contains massive quartz with impurities coloring the sinter to a light brown. There are also some rounded areas of jigsaw quartz and more QAC at the top of the slide. Curved portions of jigsaw quartz infiltrate the massive sinter. This could be from the fluids that replaced the bladed calcite, and deformed the sinter as it still existing as a silica gel before solidifying completely. Silica injections brecciate small areas of the sample before further fracturing and infilling the rock.

EF19-12:

Massive jigsaw quartz dominates this sample with only slight differentiations in color to distinguish any type of bedding. Any color appears as an oxidation stain. Thin (~2mm) beds contain dark brown massive quartz.

EF19-13:

Sample is highly fractured with veinlets spreading across wavy sinter that has been recrystallized to jigsaw quartz. Similar to all other black/brown specimens with wavy alternating whiteish gray and brown/black bands. Veinlets of silica are injected and permeate through preexisting cracks and fractures. Veins are filled with transparent chalcedony/acicular quartz and others are filled with jigsaw quartz with brown chalcedony filling the void. Some veinlets are broken formed boudinage. Sparse pyrite populates the veins and veinlets.

EF19-14:

Amorphous silica banding predominates. The colors of bands are light tan, red, pink, and brown. Many beds hold rounded inclusions that are not easily identifiable due to the extent of silicic alteration in the laminated sinter. The more brecciated portion contains angular to sub-angular clasts of the matrix-supported breccia, rhyolite, quartz, feldspar, and biotite have been transported by the sinter fluids. Those along with silicified clasts are enveloped in sinter. Highly interbedded with breccia and sinter. Sinter was likely brecciated and cut through by later-phase flows or injections of sinter. Comb quartz occupy those veinlets with jigsaw quartz covering the vein wall. Disseminated gold flakes exist in the red sinter, perhaps transported with the surficial discharge. Disseminated pyrite and gold in dark brown/black sinter.

EF19-24:

Brown, thinly laminated layers of amorphous silica and jigsaw quartz, though difficult to distinguish with the color. Lighter layers could be injected fluid through fractured dark brown/black layers and are composed of mosaic quartz. Where there is a larger void, comb quartz has grown with opaque cubes. Pyrite is mostly disseminated in small clusters of cubes within these veinlets. Larger clusters have been oxidized and are rusted.

EF19-25:

White and pick sinter dominate this sample. Jigsaw quartz makes up 95% of the sinter. The remaining 5% is the comb quartz that has crystallized from veinlets in the sample, and the metals within the bedded sinter. A small portion of the sample has distinct layering where rounded pyrite grains lie. Silica injection resulted in the layered sinter and brought with it the pyrite grains, as well as an influx of silver, though not seen in RFL. Late phase silica contains the most metals. Rounded silica grains were observed in the brown layer of sinter, which could possibly be geyserite eggs. Otherwise, sparse pyrite. Dark brown sinter through center has the high points.

EF19-26:

Laminated wavy dark brown to light gray sinter that has been deformed by fluid injection. The entire sample that is not obscured by the intense color is composed of jigsaw quartz, suggesting a recrystallization at a later point. Veins and veinlets fill in fractures in the sample and consist of jigsaw and massive quartz.

Appendix B - Supporting Figures

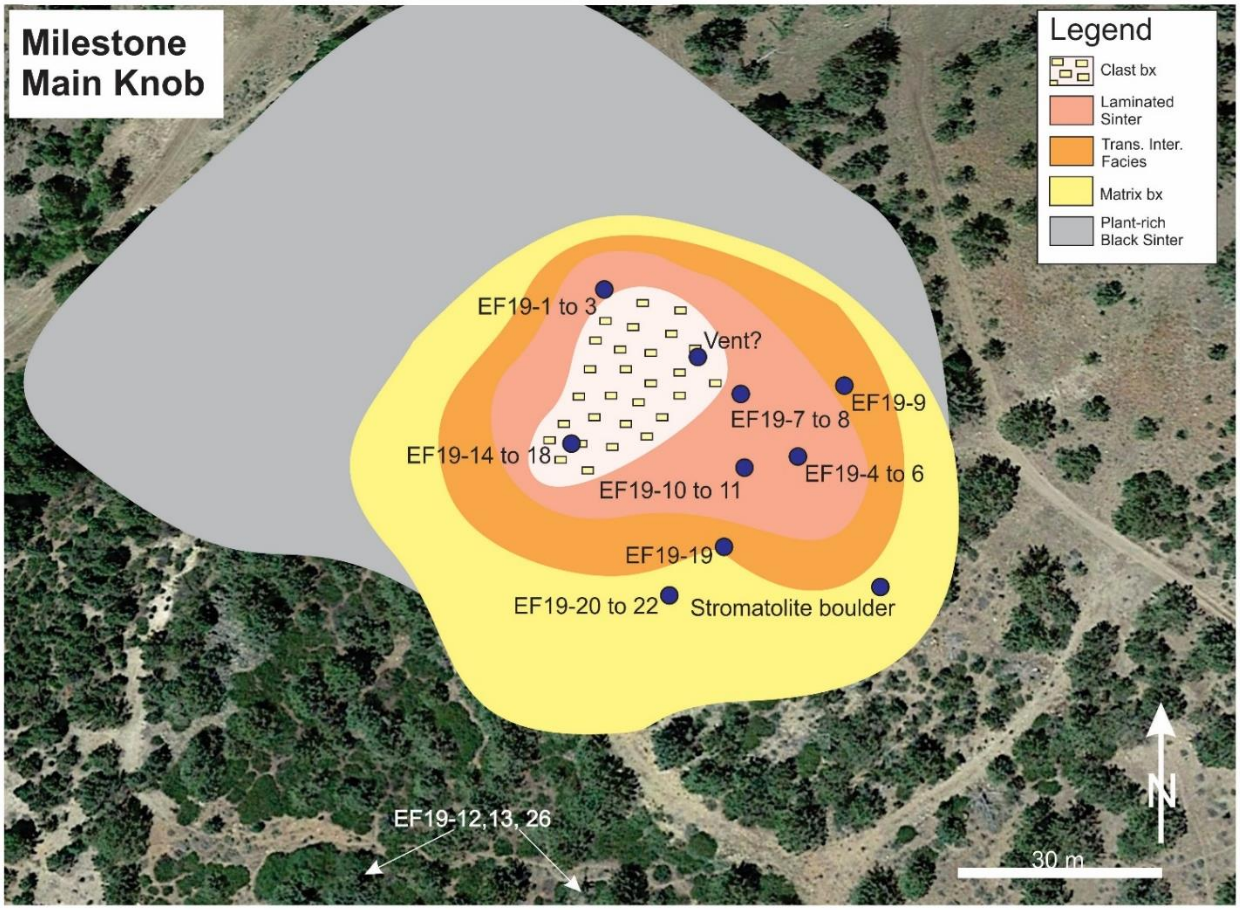

Figure B.5.1: Map of the Main Knob at Milestone with geographic locations of collected samples and notable features.

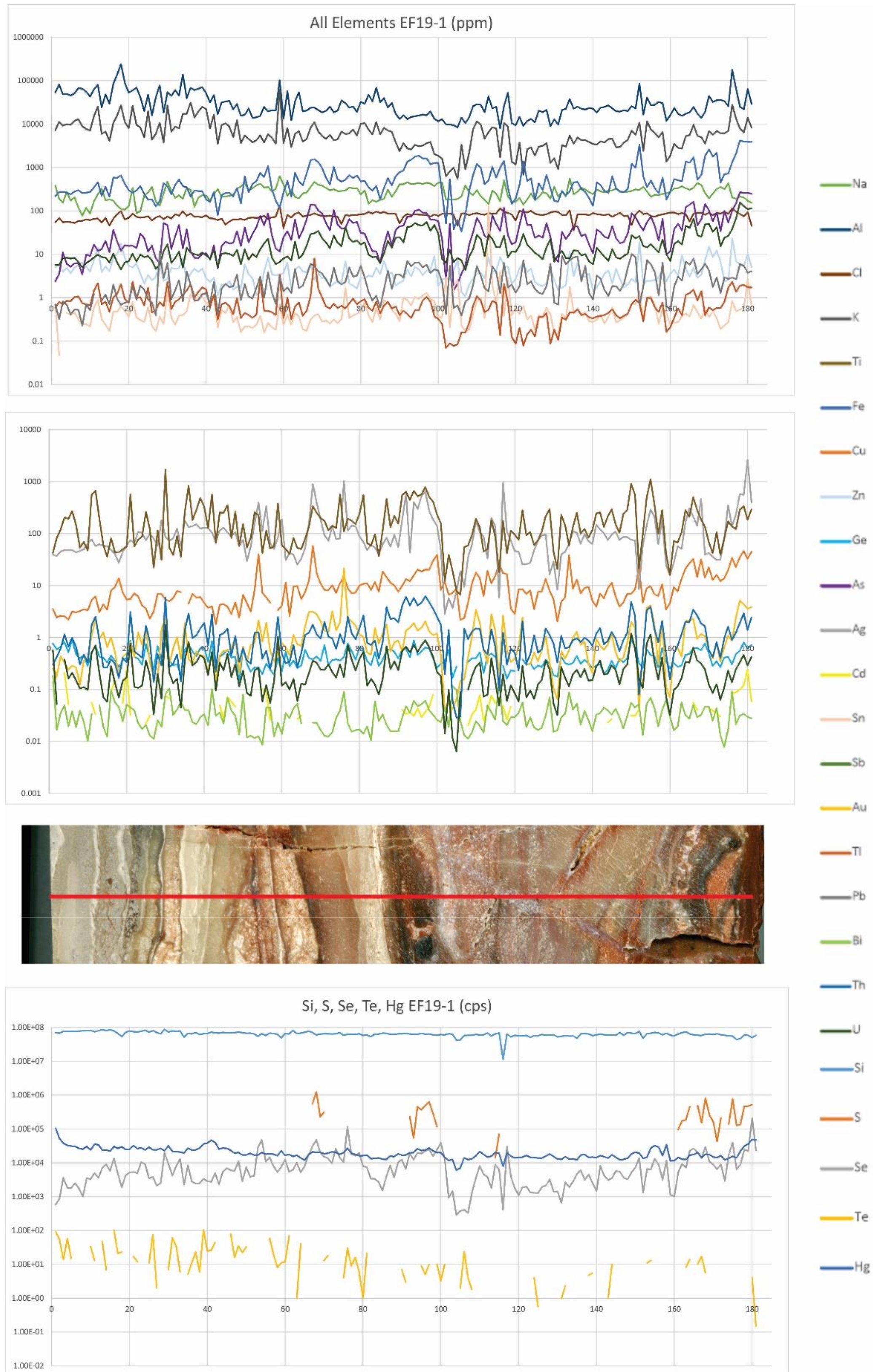

Figure B.5.2: LA-ICP-MS transect of proximal slope sample EF19-1 (middle) and all data in ppm (above) and cps (below).

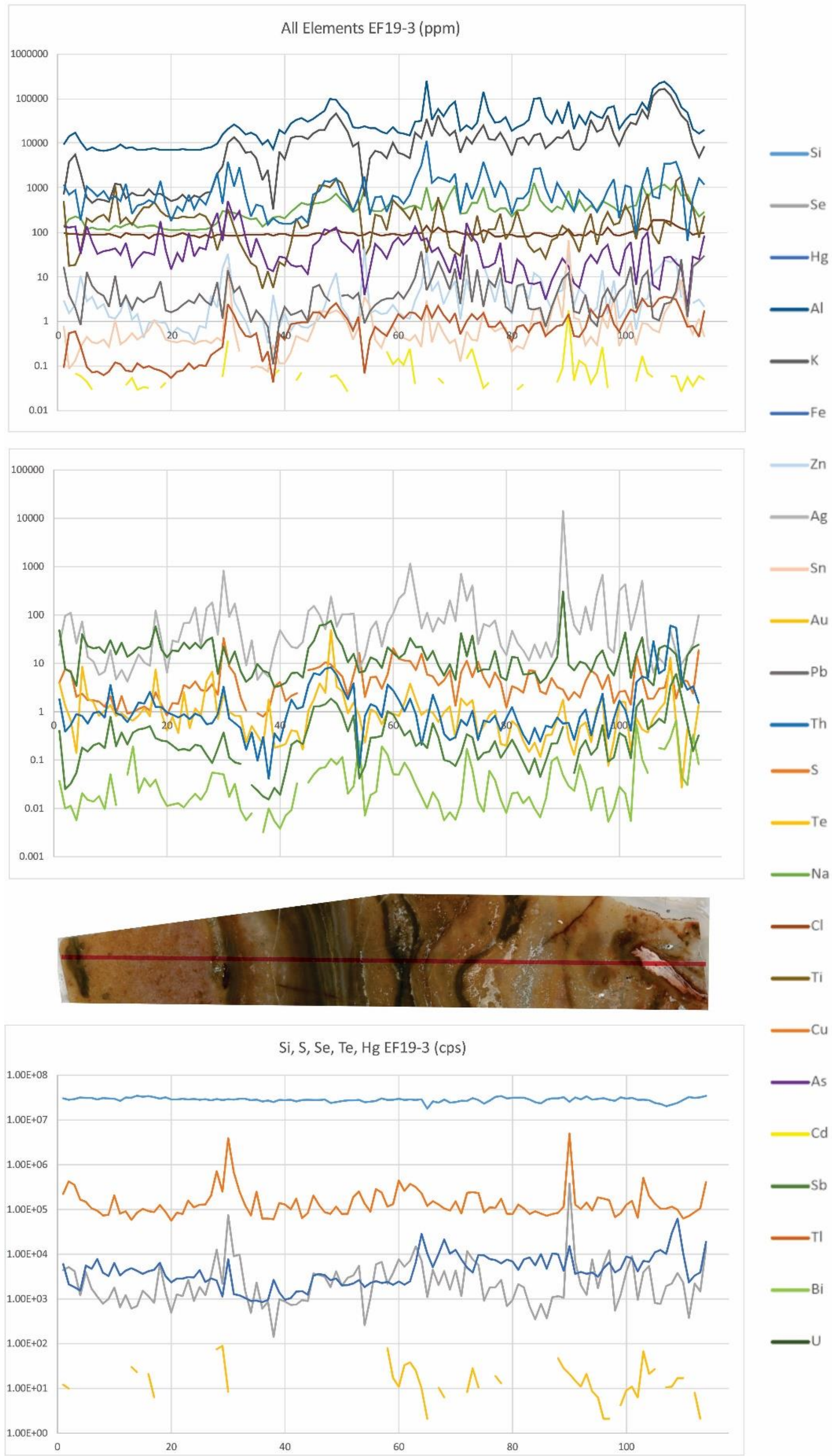

Figure B.5.3: LA-ICP-MS transect of proximal slope sample EF19-3 (middle) and all data in ppm (above) and cps (below).

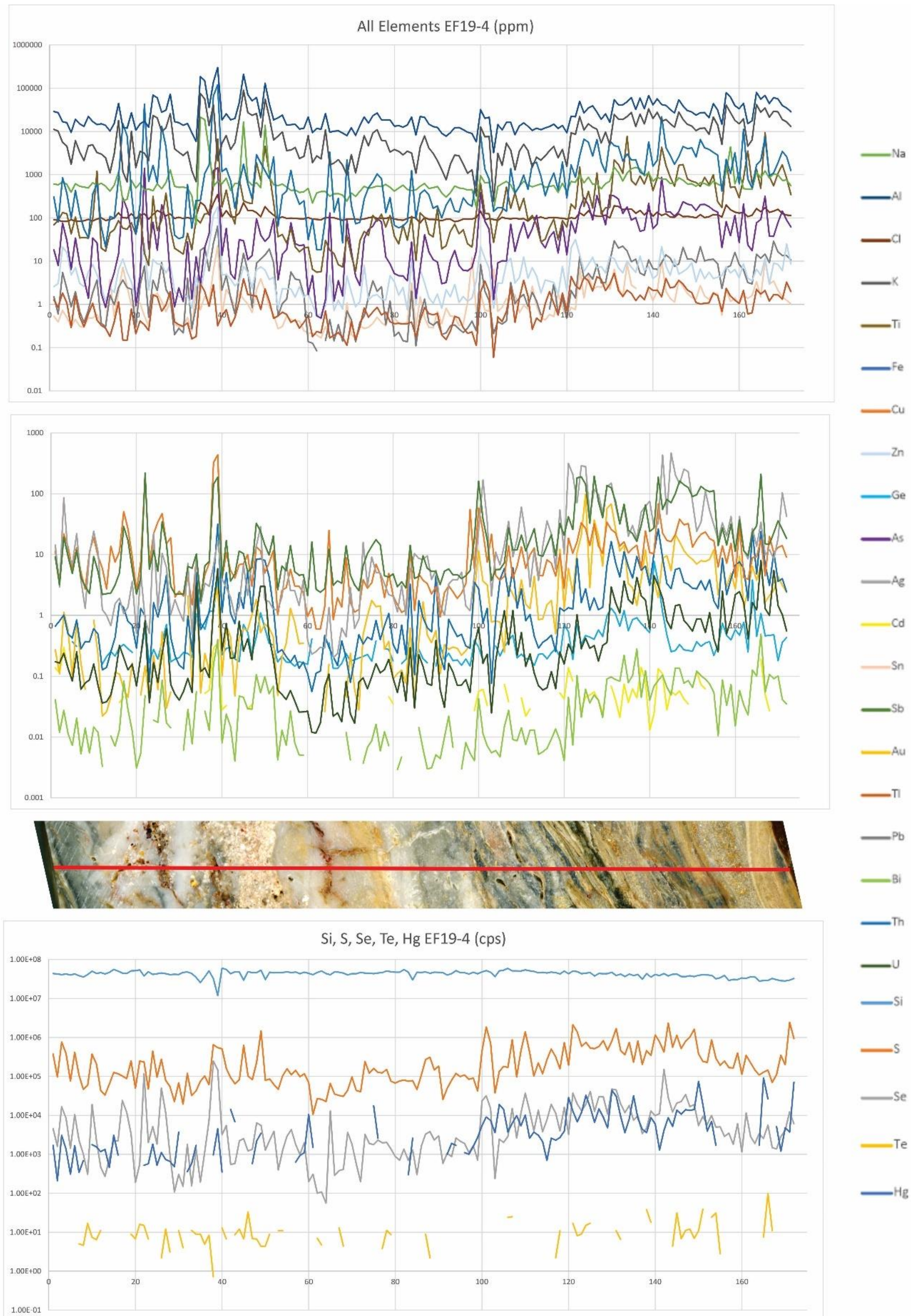

Figure B.5.4: LA-ICP-MS transect of mid-slope apron sample EF19-4 (middle) and all data in ppm (above) and cps (below).

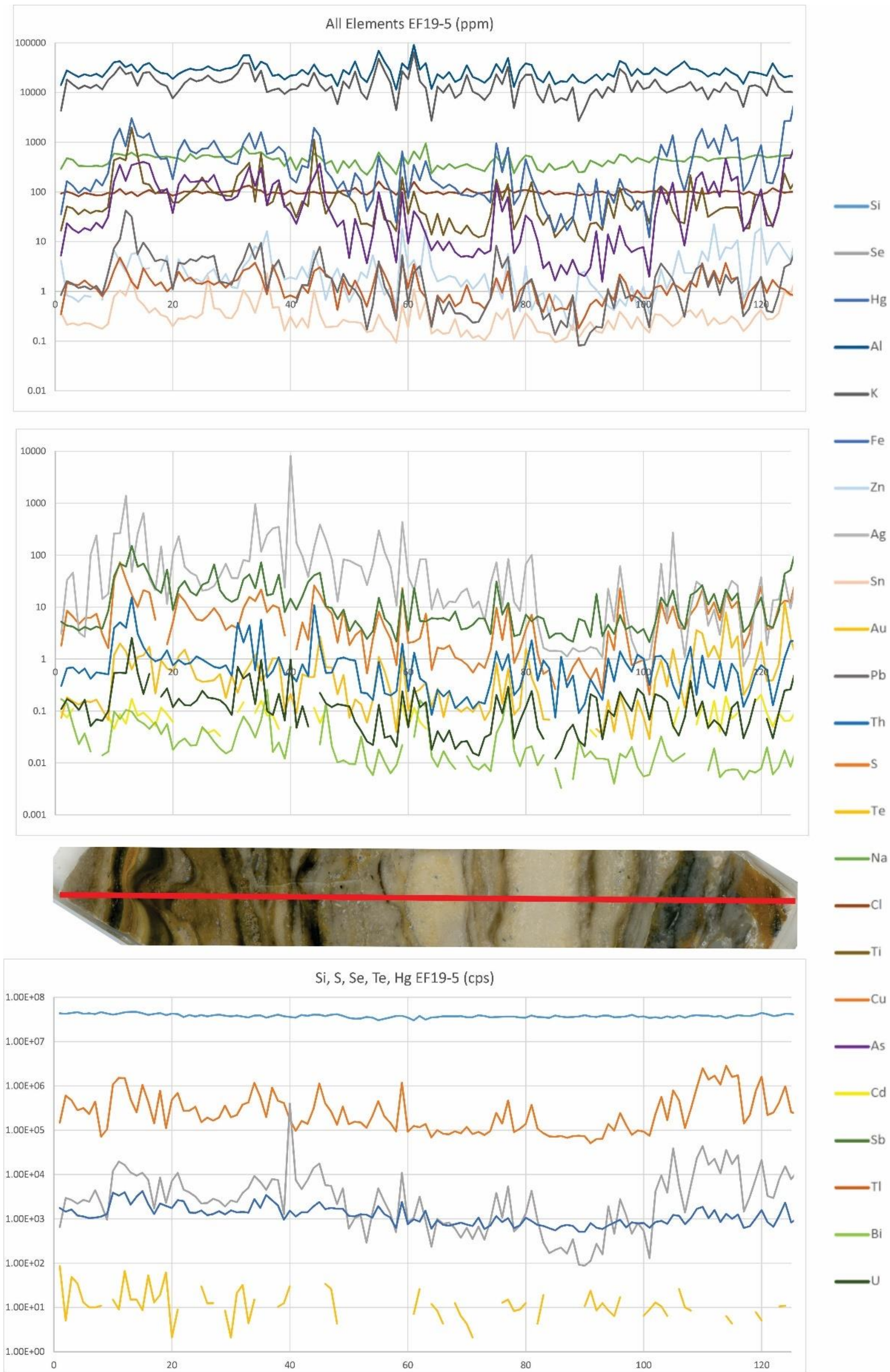

Figure B.5.5: LA-ICP-MS transect of mid-slope apron sample EF19-5 (middle) and all data in ppm (above) and cps (below).

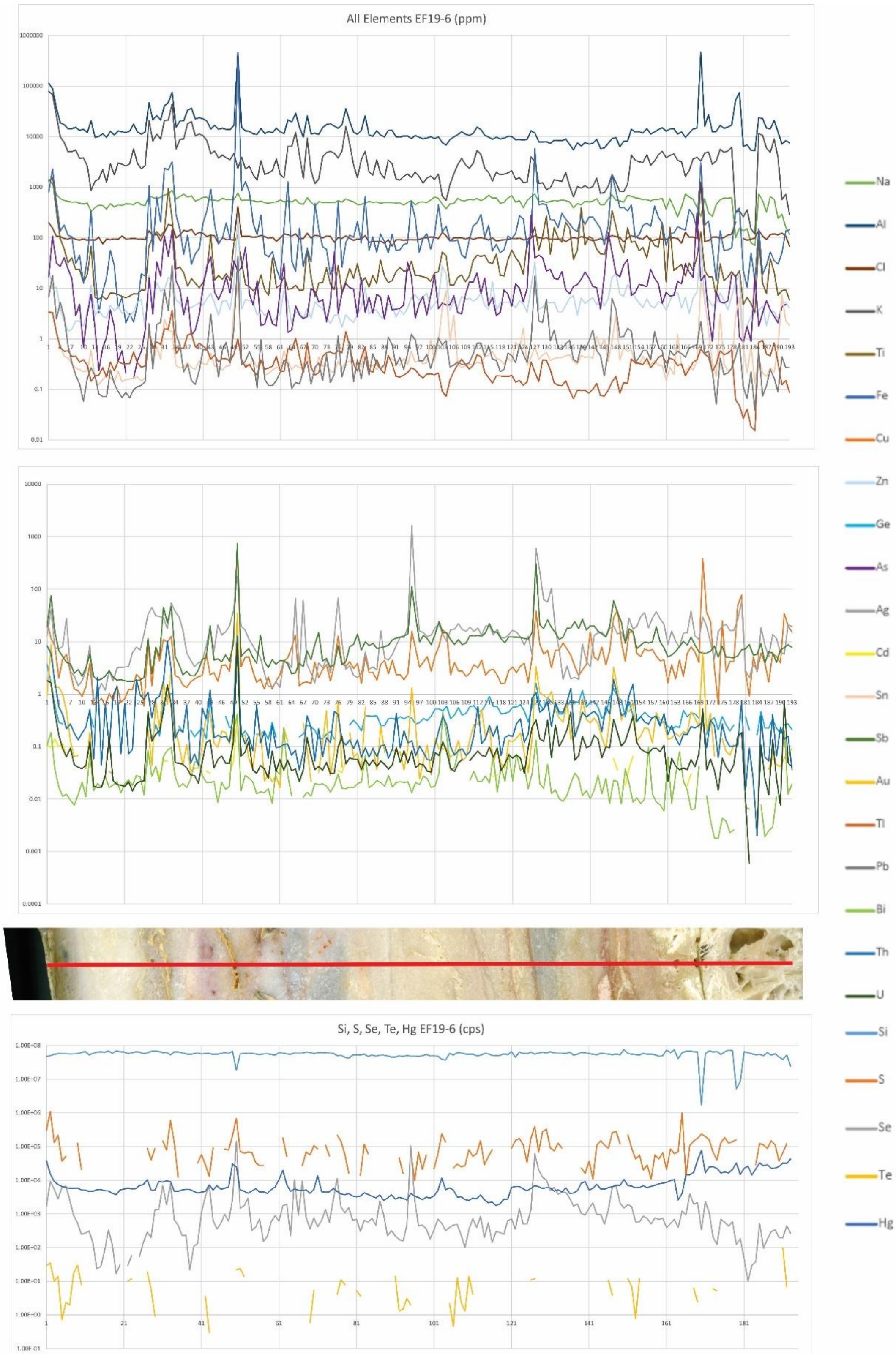

Figure B.5.6: LA-ICP-MS transect of mid-slope apron sample EF19-6 (middle) and all data in ppm (above) and cps (below).

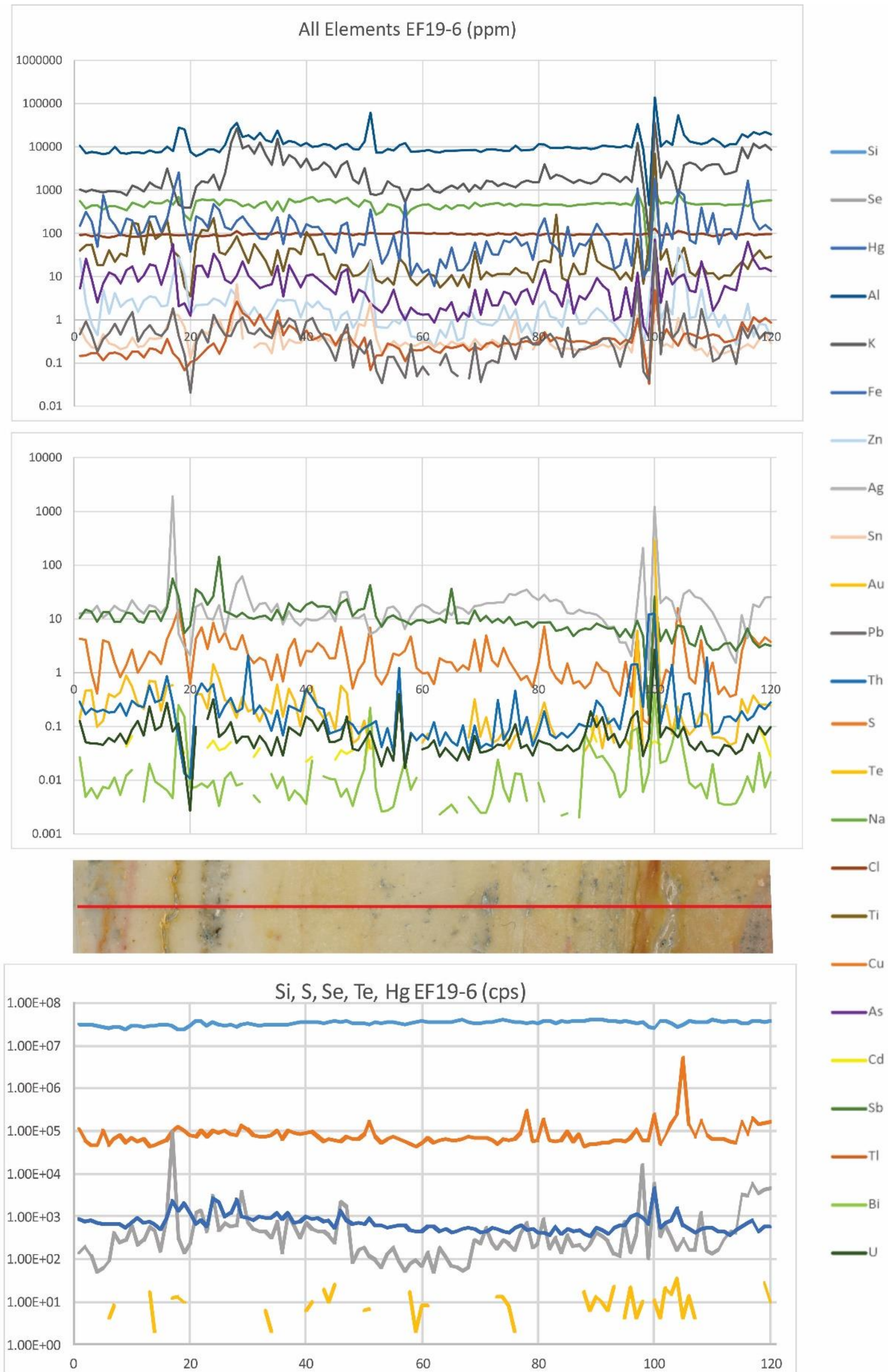

Figure B.5.7: LA-ICP-MS transect of a thin section of mid-slope apron sample EF19-6 (middle) and all data in ppm (above) and cps (below).

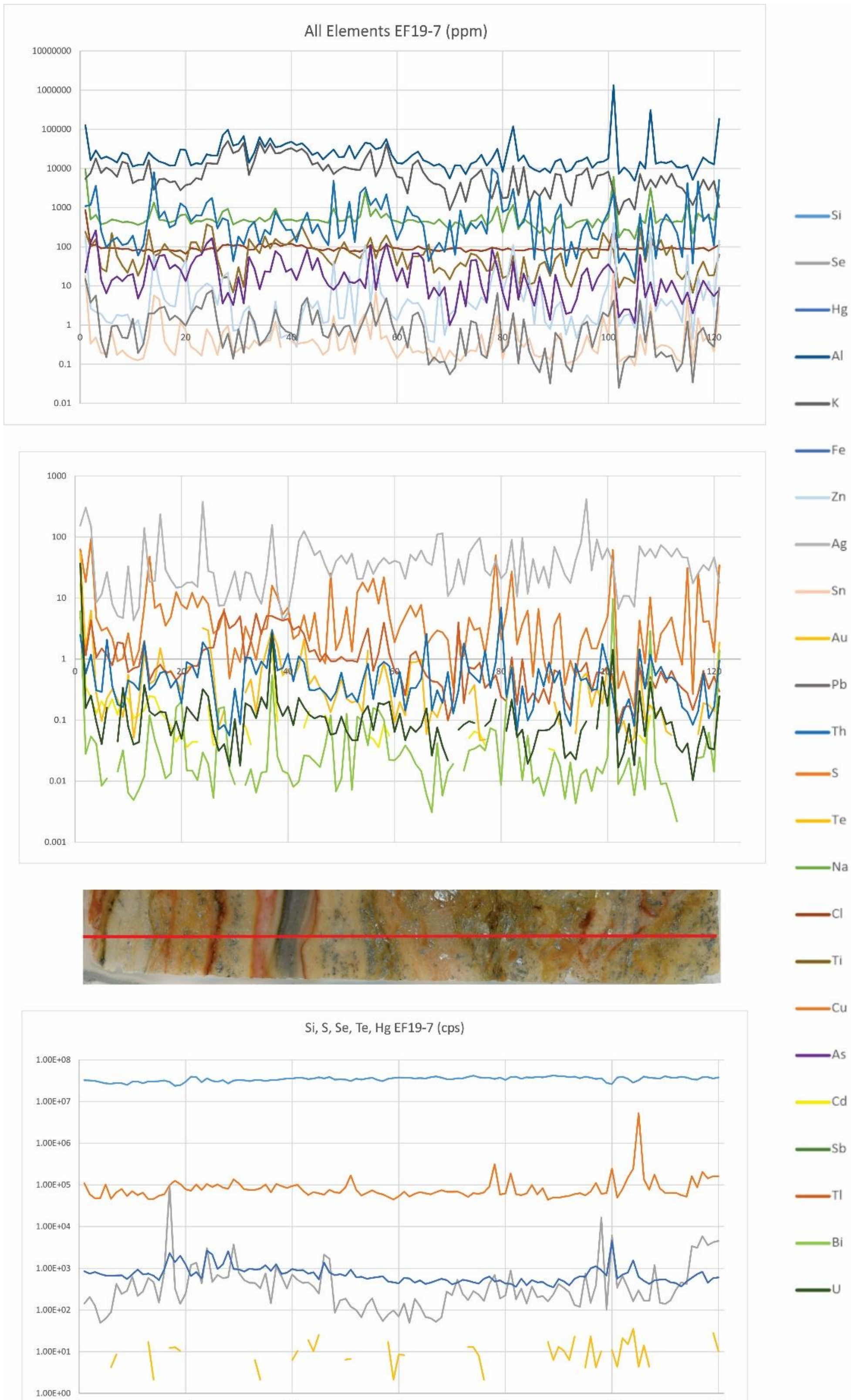

Figure B.5.8: LA-ICP-MS transect of vent sample EF19-7 (middle) and all data in ppm (above) and cps (below).

Figure B.5.9: LA-ICP-MS transect of vent sample EF19-8 (middle) and all data in ppm (above) and cps (below).

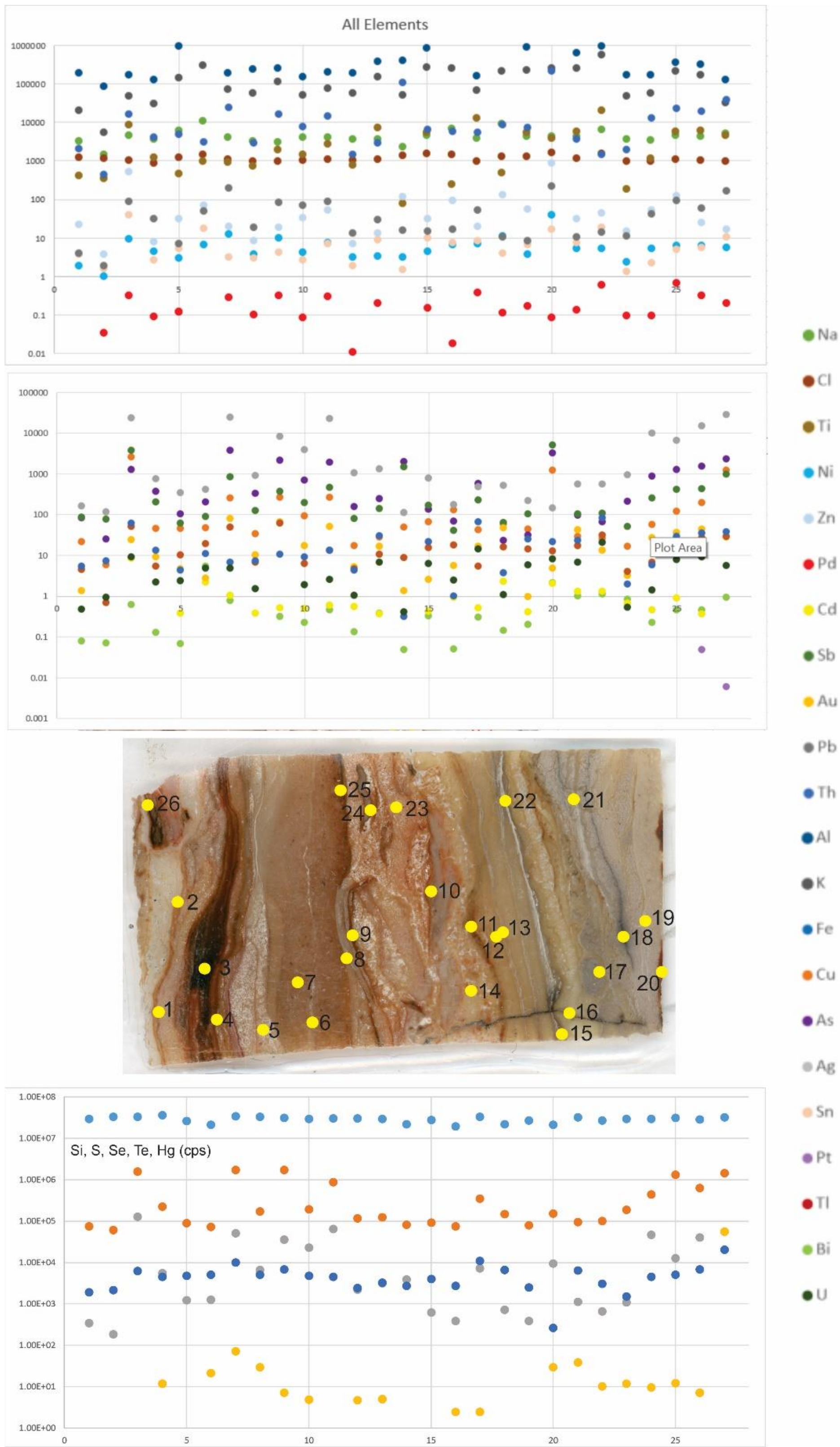

Figure B.5.10: LA-ICP-MS spot analyses map image of proximal slope sample EF19-1 and all data in ppm (above) and cps (below).

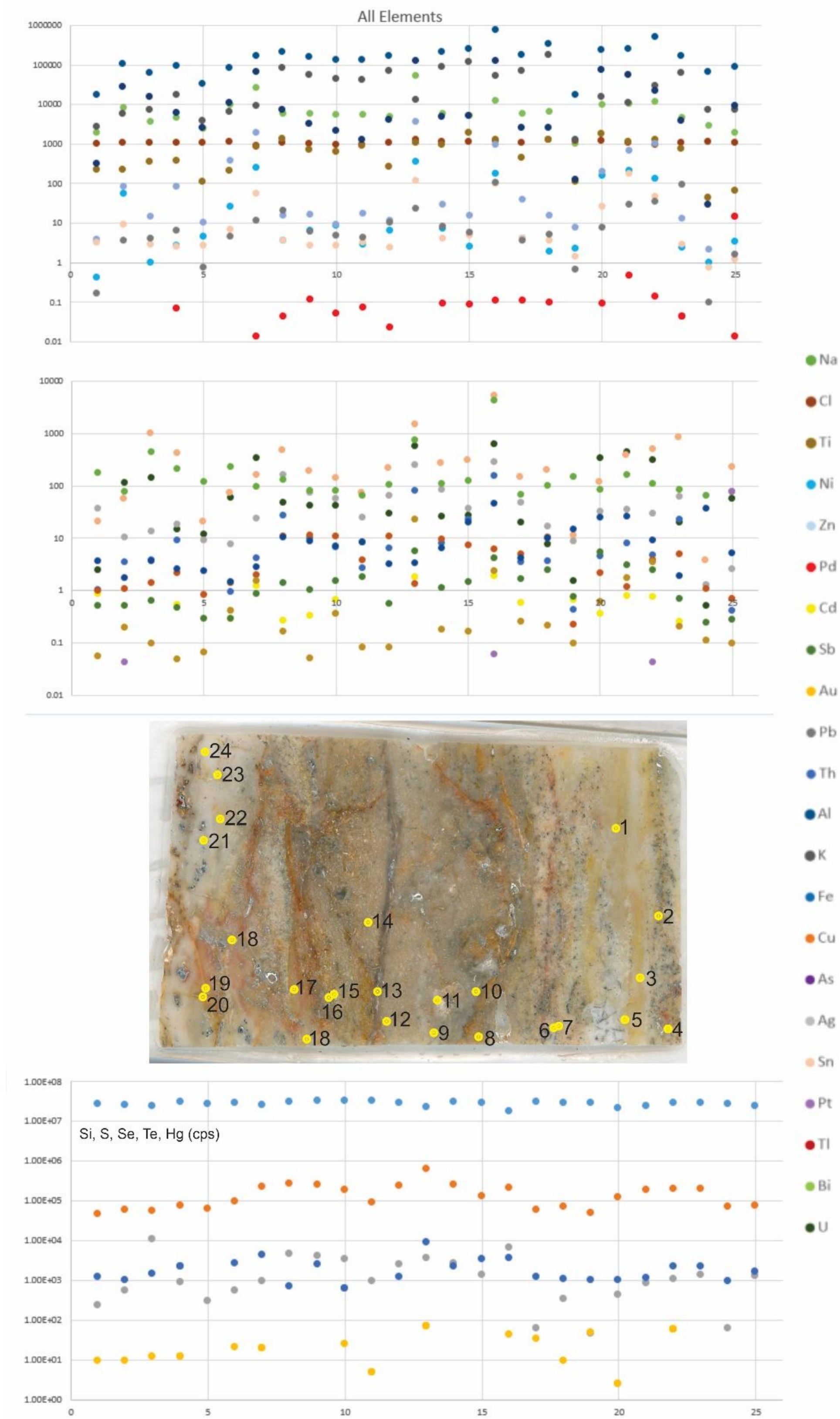

Figure 5.11: LA-ICP-MS spot analyses map image of mid-slope apron sample EF19-4 and all data in ppm (above) and cps (below).

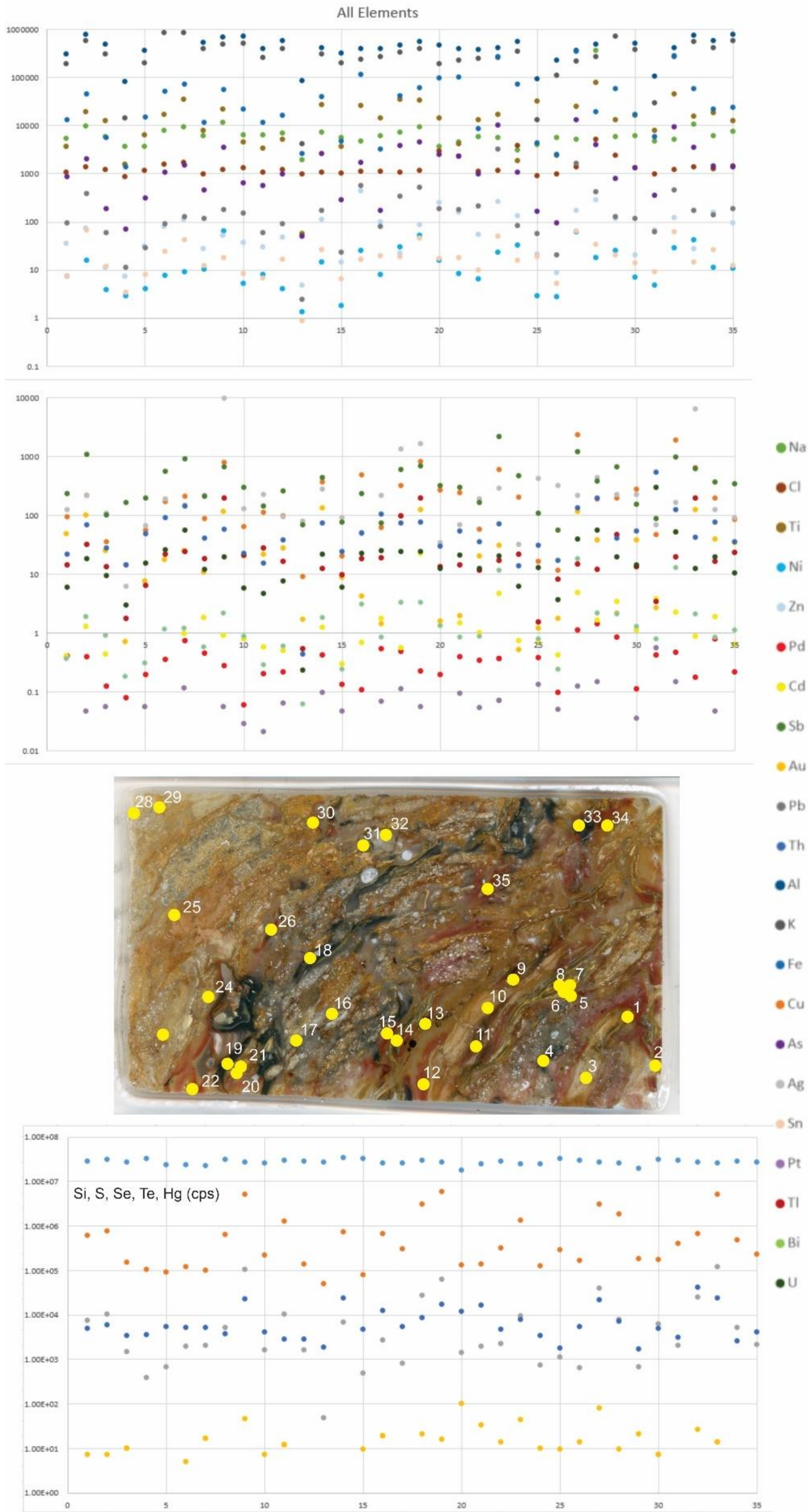

Figure B.5.12: LA-ICP-MS spot analyses map image of mid-slope apron sample EF19-14 and all data in ppm (above) and cps (below).

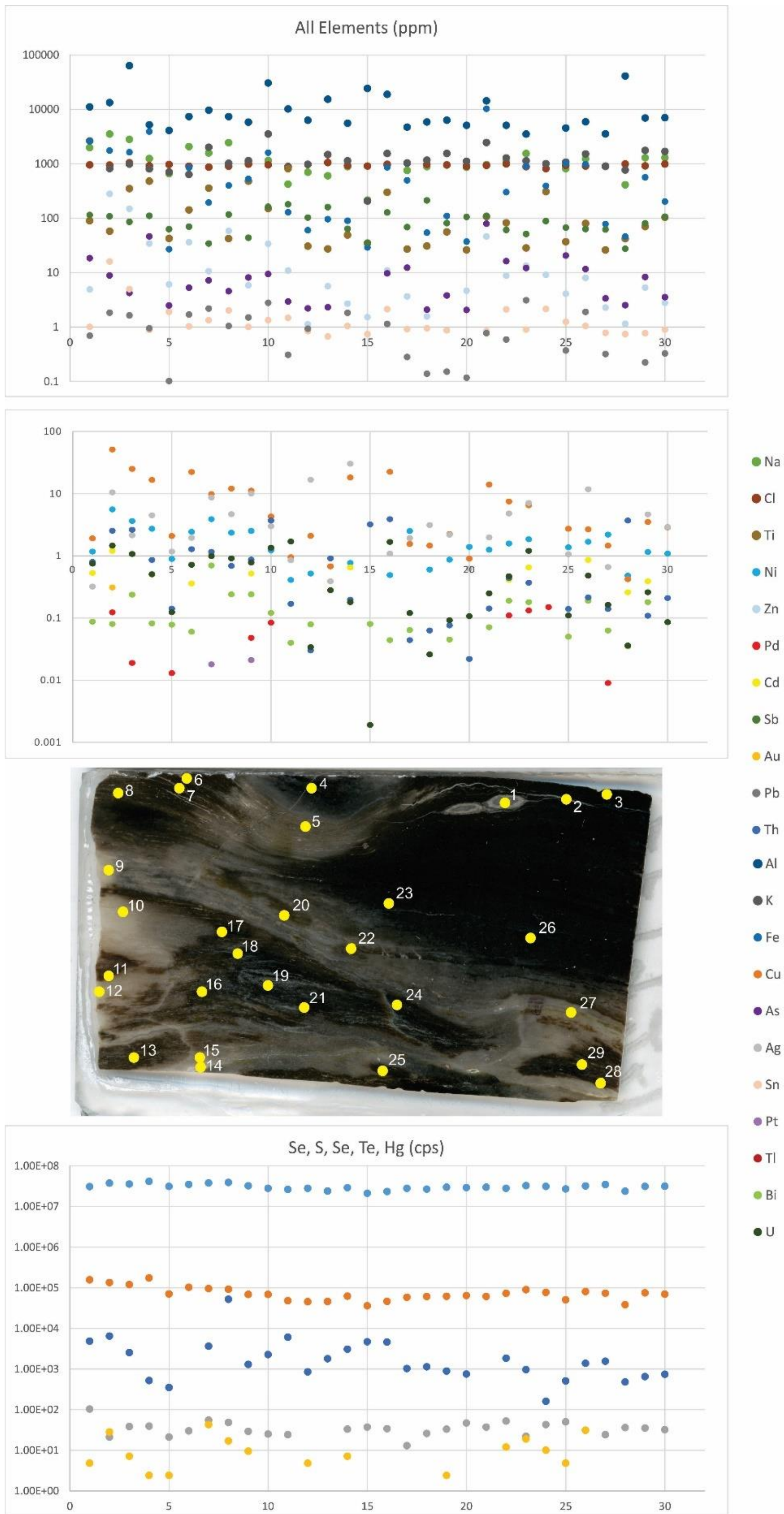

Figure B.5.13: LA-ICP-MS spot analyses map image of distal slope/marsh sample EF19-24 and data in ppm (above) and cps (below).

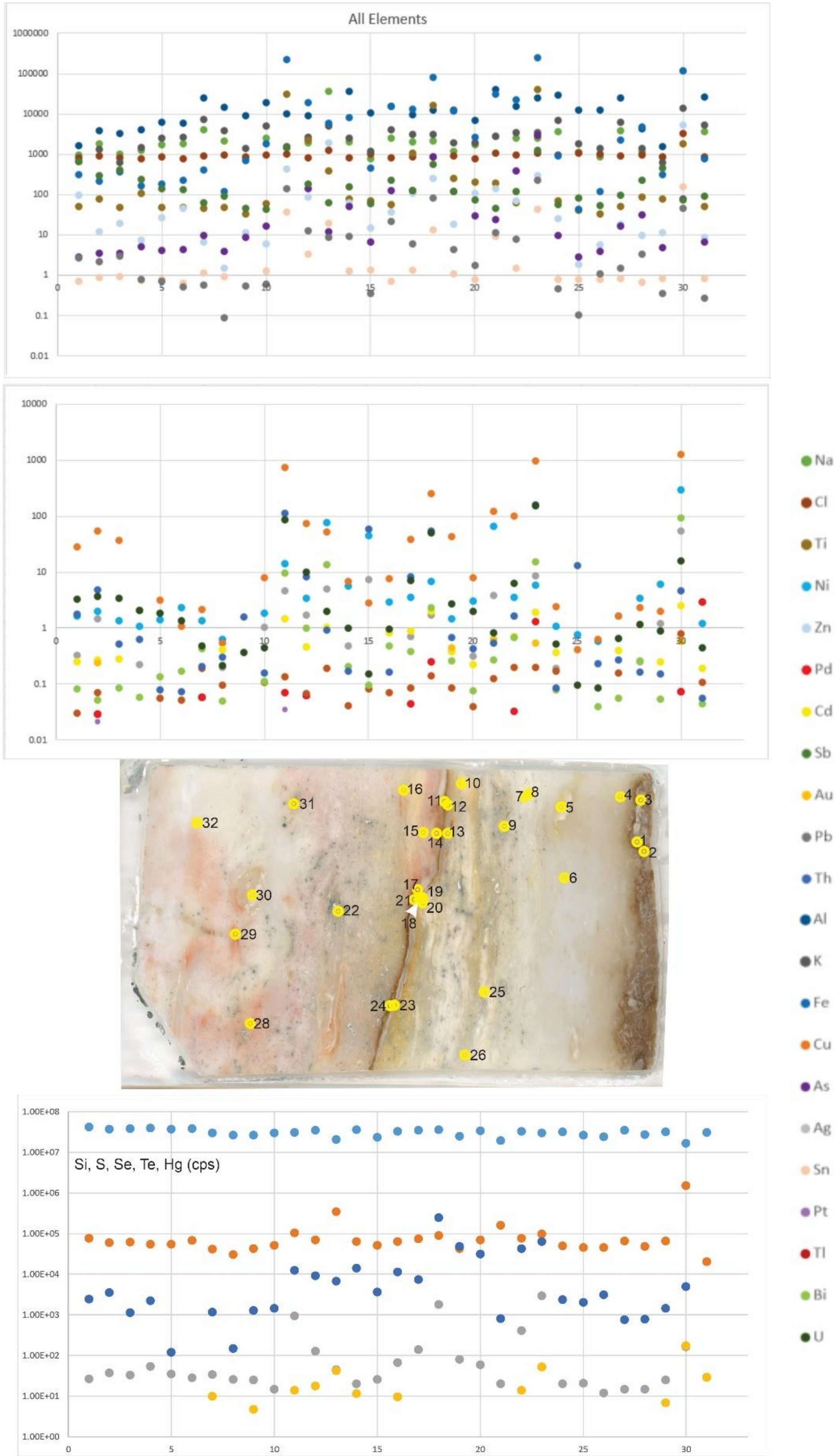

Figure B.5.14: LA-ICP-MS spot analyses map image of Wagonwheel sample EF19-25 and data in ppm (above) and cps (below).

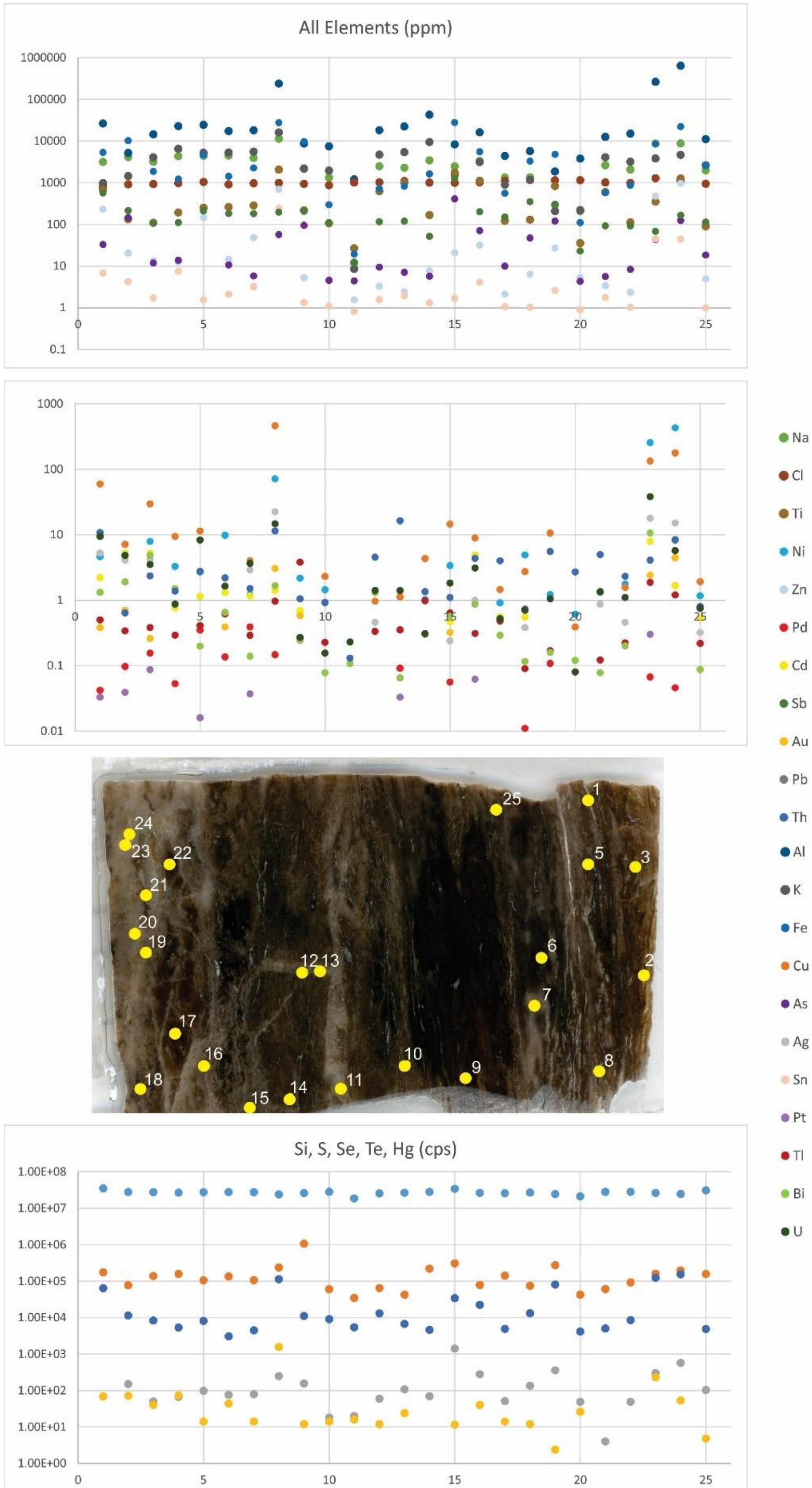

Figure B.5.15: LA-ICP-MS spot analyses map image of distal slope/marsh EF19-26 and data in ppm (above) and cps (below).

Appendix C - LA-ICP-MS Chemistry Results

Spot #	Si (cps)	Std. Dev (2σ)	S (cps)	Std. Dev (2σ)	Se (cps)	Std. Dev (2σ)	Te (cps)	Std. Dev (2σ)	Hg (cps)	Std. Dev (2σ)
EF19-1										
EF19-1.01	2.86E+07	980000	73600	3100	336	72	0	1	1900	450
EF19-1.02	3.29E+07	970000	59300	3100	183	49	0	1	2110	420
EF19-1.03	3.25E+07	1.00E+06	1.57E+06	160000	125000	38000	0	1	6110	670
EF19-1.04	3.51E+07	1.10E+06	223000	11000	5420	270	11.6	9.9	4450	470
EF19-1.05	2.60E+07	720000	88100	4200	1200	200	0	1	4700	1100
EF19-1.06	2.10E+07	740000	71200	5100	1260	280	21	15	4920	470
EF19-1.07	3.31E+07	750000	1.70E+06	76000	50700	2000	71	63	9880	720
EF19-1.08	3.22E+07	930000	171000	10000	6550	670	29	26	4980	490
EF19-1.09	3.11E+07	840000	1.67E+06	180000	35400	3600	7.1	8	6680	500
EF19-1.10	2.86E+07	1.10E+06	191200	6600	22800	1300	4.8	6.7	4650	510
EF19-1.11	2.95E+07	850000	850000	110000	63100	4400	0	1	4380	560
EF19-1.12	2.94E+07	1.20E+06	116200	5900	2190	220	4.7	6.5	2400	480
EF19-1.13	2.92E+07	700000	123400	5100	3100	250	4.9	6.8	3210	410

Spot #	Si (cps)	Std. Dev (2σ)	S (cps)	Std. Dev (2σ)	Se (cps)	Std. Dev (2σ)	Te (cps)	Std. Dev (2σ)	Hg (cps)	Std. Dev (2σ)
EF19-1.14	2.15E+07	1.10E+06	79400	9000	3780	330	0	1	2650	410
EF19-1.15	2.75E+07	510000	90700	3000	610	100	0	1	3900	450
EF19-1.16	1.91E+07	300000	73700	3100	381	67	2.4	4.8	2700	370
EF19-1.17	3.25E+07	700000	340800	9200	7090	280	2.4	4.8	10900	660
EF19-1.18	2.18E+07	280000	143600	7500	710	110	0	1	6530	390
EF19-1.19	2.62E+07	470000	78000	2900	376	59	0	1	2490	570
EF19-1.20	2.10E+07	270000	149400	6300	9190	330	29	14	260	440
EF19-1.21	3.12E+07	450000	94600	3900	1110	130	38	25	6360	970
EF19-1.22	2.65E+07	520000	97600	3800	650	92	10	11	3000	460
EF19-1.23	2.92E+07	880000	185000	11000	1060	130	11.6	9.9	1470	310
EF19-1.24	2.90E+07	960000	440000	80000	46000	20000	9.5	9.2	4470	630
EF19-1.25	3.09E+07	790000	1.28E+06	340000	12640	670	12	16	5060	410
EF19-1.26	2.84E+07	530000	611000	22000	39100	1300	7.1	8	6630	430
EF19-1.27	3.16E+07	870000	1.43E+06	63000	54400	5000	0	1	19900	2900

Spot #	Na (ppm)	Std. Dev (2σ)	Al (ppm)	Std. Dev (2σ)	Cl (ppm)	Std. Dev (2σ)	K (ppm)	Std. Dev (2σ)	Ti (ppm)	Std. Dev (2σ)
EF19-1.01	3300	220	191000	29000	1202	72	20400	4000	418	42
EF19-1.02	1438	46	83800	1000	1122	59	5540	200	341	14
EF19-1.03	4570	180	164800	3400	1047	63	46900	1300	8490	390
EF19-1.04	3540	120	125500	2000	883	57	29880	900	1244	98
EF19-1.05	6060	180	925000	42000	1195	82	140100	8300	461	88
EF19-1.06	10820	410	--	--	1460	84	294100	5700	993	63
EF19-1.07	4160	340	183800	2900	1066	68	73100	2400	927	36
EF19-1.08	3260	280	237000	13000	960	66	55100	1800	737	56
EF19-1.09	3130	130	248300	3500	993	57	111600	3500	1940	160
EF19-1.10	4050	130	147900	4000	1007	76	51700	2500	1434	93
EF19-1.11	3970	170	195300	5200	1056	79	76100	3100	2690	160
EF19-1.12	3520	130	185200	4100	1015	76	56000	2200	751	66
EF19-1.13	3530	330	369900	9800	1075	82	152400	5200	7060	300

Spot #	Na (ppm)	Std. Dev (2σ)	Al (ppm)	Std. Dev (2σ)	Cl (ppm)	Std. Dev (2σ)	K (ppm)	Std. Dev (2σ)	Ti (ppm)	Std. Dev (2σ)
EF19-1.14	2247	58	386000	25000	1344	97	51200	3700	78.3	5.3
EF19-1.15	4420	110	815000	11000	1511	76	264700	3800	5470	380
EF19-1.16	6700	250	--	--	1470	120	246600	5700	244	13
EF19-1.17	3761	97	158300	2100	989	58	68800	1200	12540	480
EF19-1.18	9240	520	--	--	1288	97	213300	9100	496	31
EF19-1.19	4300	130	879000	11000	1286	78	221900	3400	5260	140
EF19-1.20	4410	130	--	--	1660	100	243900	4400	3850	100
EF19-1.21	4200	490	635000	14000	1150	62	253400	9100	5830	260
EF19-1.22	6520	490	936000	11000	1550	82	557000	8500	20490	460
EF19-1.23	3620	320	167900	3100	970	63	46450	850	186	15
EF19-1.24	3420	230	169200	5500	974	71	55900	3500	1167	84
EF19-1.25	4550	180	361000	16000	1081	53	207000	10000	5560	410
EF19-1.26	4210	130	324100	7800	1041	64	168200	4500	6030	350
EF19-1.27	5020	330	124700	1900	958	65	32690	720	4630	180

Spot #	Ti (ppm)	Std. Dev (2σ)	Fe (ppm)	Std. Dev (2σ)	Ni (ppm)	Std. Dev (2σ)	Cu (ppm)	Std. Dev (2σ)	Zn (ppm)	Std. Dev (2σ)
EF19-1.01	41.2	4.3	2140	160	1.96	0.53	21.6	2.5	22.2	5.8
EF19-1.02	32.5	1.3	437	45	1	0.34	5.88	0.43	3.9	2
EF19-1.03	941	42	16910	780	9.7	1	2590	990	530	270
EF19-1.04	123	10	4210	220	4.63	0.69	45.3	1.9	8.1	1.3
EF19-1.05	52	8.5	4880	200	3.01	0.74	45	2.1	32.5	2.2
EF19-1.06	106	5.9	3220	110	6.8	2	48.1	6	71	11
EF19-1.07	96	4.3	24570	390	13	1.6	249.9	4.8	20.1	1.5
EF19-1.08	71.3	5.2	2990	200	3.84	0.74	34.1	2	8.5	1.2
EF19-1.09	191	17	16360	930	10.2	1.2	267	27	19.3	1.7
EF19-1.10	139.3	8.5	7820	210	4.36	0.7	93.2	3.5	33.4	3.1
EF19-1.11	268	18	14990	650	7.5	1	268	15	54.4	4
EF19-1.12	71.2	6.4	1499	96	3.29	0.64	17.1	2.8	7.1	1.1
EF19-1.13	776	33	2910	120	3.41	0.64	28.3	1.2	13.6	1.5

Spot #	Ti (ppm)	Std. Dev (2σ)	Fe (ppm)	Std. Dev (2σ)	Ni (ppm)	Std. Dev (2σ)	Cu (ppm)	Std. Dev (2σ)	Zn (ppm)	Std. Dev (2σ)
EF19-1.14	8.18	0.45	112000	10000	3.3	0.78	48.9	2.9	116.8	6
EF19-1.15	598	38	6470	150	4.6	1.1	66.8	1.7	31.5	2.8
EF19-1.16	34	1.6	6010	300	7	1.2	129	16	94.5	9.6
EF19-1.17	1392	51	5501	94	7.37	0.76	42.3	1.2	20.5	1.3
EF19-1.18	59.5	3.1	8570	330	11.5	1.3	60	2.4	134	10
EF19-1.19	594	18	7230	120	3.85	0.63	43.7	1.3	56.1	3.3
EF19-1.20	383	12	217700	3200	40.6	2.6	1208	27	878	32
EF19-1.21	650	31	3712	92	5.4	1.5	29.1	1.3	32.7	4.1
EF19-1.22	2284	49	1509	36	5.5	3.3	26	1.1	45.8	7.1
EF19-1.23	18.3	1.4	2000	230	2.48	0.54	16.6	1.3	15.3	1.5
EF19-1.24	113.9	8.3	13030	850	5.3	3	56.9	2.5	54.6	5.7
EF19-1.25	624	44	23140	740	6.27	0.97	119.8	2.9	127.1	4.2
EF19-1.26	664	38	19810	970	6.4	1.2	196.2	5.1	25	1.9
EF19-1.27	517	22	39800	1500	5.68	0.81	1210	45	17.4	1.3

Spot #	As (ppm)	Std. Dev (2σ)	Pd (ppm)	Std. Dev (2σ)	Ag (ppm)	Std. Dev (2σ)	Cd (ppm)	Std. Dev (2σ)	Sn (ppm)	Std. Dev (2σ)
EF19-1.01	82	7.3	--	--	162.1	5.8	--	--	3.73	0.85
EF19-1.02	25.4	2.6	0.035	0.04	113.8	3.8	--	--	1.6	0.22
EF19-1.03	1257	53	0.32	0.11	23900	8400	8.4	4.1	40.2	7.3
EF19-1.04	371	26	0.092	0.055	761	39	--	--	2.7	0.27
EF19-1.05	104	12	0.121	0.089	348	25	0.38	0.2	5.27	0.6
EF19-1.06	204	17	0	1	410	37	2.2	1.6	18.5	1.4
EF19-1.07	3820	76	0.29	0.12	24120	540	1.05	0.67	3.23	0.48
EF19-1.08	328	22	0.102	0.061	903	51	0.38	0.3	3	1
EF19-1.09	2120	120	0.32	0.12	8330	850	0.51	0.27	4.31	0.86
EF19-1.10	701	23	0.088	0.062	3840	300	0.5	0.24	2.74	0.43
EF19-1.11	1882	83	0.3	0.12	22500	1300	0.6	0.23	7.3	1.5
EF19-1.12	154	15	0.011	0.022	1040	41	0.55	0.38	1.91	0.45
EF19-1.13	242	15	0.209	0.093	1339	49	0.36	0.46	9.17	0.83

Spot #	As (ppm)	Std. Dev (2σ)	Pd (ppm)	Std. Dev (2σ)	Ag (ppm)	Std. Dev (2σ)	Cd (ppm)	Std. Dev (2σ)	Sn (ppm)	Std. Dev (2σ)
EF19-1.14	1970	170	--	--	112	20	--	--	1.53	0.27
EF19-1.15	136.6	6.7	0.158	0.093	777	20	0.43	0.31	10.29	0.59
EF19-1.16	69.9	4.4	0.019	0.037	172.6	7.3	0.93	0.38	7.48	0.8
EF19-1.17	570	10	0.38	0.13	478	10	0.52	0.54	8.64	0.65
EF19-1.18	23.6	2.1	0.115	0.08	520	35	2.27	0.56	4.04	0.39
EF19-1.19	30.9	2.2	0.175	0.083	217.3	6.7	0.41	0.21	6.9	0.53
EF19-1.20	3225	75	0.086	0.073	146.1	4.8	2.04	0.68	16.8	0.68
EF19-1.21	96.4	8.6	0.141	0.07	562	22	1.31	0.88	7.51	0.87
EF19-1.22	66.1	4.2	0.62	0.17	549	16	1.32	0.94	19.5	1.1
EF19-1.23	211	22	0.098	0.072	947	31	0.66	0.43	1.36	0.41
EF19-1.24	882	47	0.099	0.064	9800	3700	0.46	0.27	2.32	0.34
EF19-1.25	1251	43	0.68	0.18	6630	820	0.9	0.42	5.02	0.5
EF19-1.26	1533	65	0.32	0.14	14740	880	0.37	0.24	5.65	0.53
EF19-1.27	2326	98	0.212	0.09	28400	1500	--	--	11.05	0.57

Spot #	Sb (ppm)	Std. Dev (2σ)	Pt (ppm)	Std. Dev (2σ)	Au (ppm)	Std. Dev (2σ)	Tl (ppm)	Std. Dev (2σ)	Pb (ppm)	Std. Dev (2σ)
EF19-1.01	86.2	3	--	--	1.36	0.32	4.47	0.97	3.97	0.61
EF19-1.02	76.6	2.9	--	--	--	--	0.696	0.067	1.89	0.3
EF19-1.03	3800	1700	--	--	24.1	1.3	50.2	1.8	87.8	2.8
EF19-1.04	206	13	--	--	9.12	0.82	5.48	0.4	32.8	4.4
EF19-1.05	60.3	3.4	0	1	4.6	1.9	10.34	0.54	7.2	1.9
EF19-1.06	90.6	5.8	--	--	2.8	0.85	19.01	0.87	50.5	8.6
EF19-1.07	827	14	0	1	80.8	2.2	48.2	1.4	197	5.7
EF19-1.08	125.5	6.5	--	--	10.38	0.82	6.66	0.33	18.9	1.6
EF19-1.09	373	20	0	1	66	4.4	60.6	6.1	84.6	6.1
EF19-1.10	197.1	4.7	0	1	17	0.88	6.22	0.41	71.4	4.2
EF19-1.11	455	18	--	--	50.4	2	13.2	0.89	89.2	5
EF19-1.12	78.6	3.8	--	--	5.19	0.62	4.71	0.48	13.7	1.7
EF19-1.13	139	3.5	--	--	16.5	1.1	10.5	0.52	31	1.9

Spot #	Sb (ppm)	Std. Dev (2σ)	Pt (ppm)	Std. Dev (2σ)	Au (ppm)	Std. Dev (2σ)	Tl (ppm)	Std. Dev (2σ)	Pb (ppm)	Std. Dev (2σ)
EF19-1.14	1450	130	0	1	1.37	0.31	8.63	0.82	15.7	1.5
EF19-1.15	169	5.5	--	--	2.53	0.28	15.41	0.54	15.06	0.87
EF19-1.16	40.5	1.7	--	--	5.62	0.72	17.65	0.65	17	1.3
EF19-1.17	224	3.7	--	--	16.51	0.74	5.39	0.3	53.2	1.3
EF19-1.18	63.8	1.5	--	--	47.6	4.7	16.2	1	10.93	0.92
EF19-1.19	103.4	2	--	--	0.98	0.2	14.25	0.38	8.72	0.68
EF19-1.20	5060	120	0	1	4.76	0.41	12.63	0.58	219	8
EF19-1.21	102.1	2.3	--	--	43	34	17.1	1	10.9	1.6
EF19-1.22	107.1	2.4	--	--	13.06	0.53	31.5	1.1	14.5	1.5
EF19-1.23	51.1	2.9	--	--	3.19	0.39	4.03	0.25	11.5	1.8
EF19-1.24	252	15	--	--	26.9	3	6.72	0.36	42.1	4.1
EF19-1.25	414	13	--	--	36.5	1	16.36	0.67	96.6	3.2
EF19-1.26	426	19	0.048	0.037	43.8	2.5	27	1.2	61.2	2
EF19-1.27	963	32	0.006	0.013	28.4	1.4	28.7	2.4	166.4	9.5

Spot #	Bi (ppm)	Std. Dev (2σ)	Th (ppm)	Std. Dev (2σ)	U (ppm)	Std. Dev (2σ)
EF19-1.01	0.078	0.033	5.5	1.9	0.468	0.068
EF19-1.02	0.07	0.038	7.32	0.9	0.92	0.087
EF19-1.03	0.615	0.065	61.8	2.8	9.09	0.61
EF19-1.04	0.13	0.026	13.13	0.76	2.21	0.23
EF19-1.05	0.069	0.03	4.37	0.99	2.4	1.1
EF19-1.06	5.4	8.1	11	1.1	4.8	1.6
EF19-1.07	0.78	0.3	6.68	0.46	4.8	3.4
EF19-1.08	--	--	7.4	2.7	1.5	0.19
EF19-1.09	0.32	0.11	10.65	0.84	--	--
EF19-1.10	0.221	0.048	8.95	0.62	1.92	0.22
EF19-1.11	0.451	0.069	13.39	0.76	2.53	0.27
EF19-1.12	0.131	0.054	4.37	0.48	1.06	0.2
EF19-1.13	0.383	0.068	29.8	1	6.88	0.45

Spot #	Bi (ppm)	Std. Dev (2σ)	Th (ppm)	Std. Dev (2σ)	U (ppm)	Std. Dev (2σ)
EF19-1.14	0.049	0.025	0.314	0.078	0.406	0.061
EF19-1.15	0.33	0.12	21.9	1.3	6.29	0.72
EF19-1.16	0.051	0.026	0.99	0.11	2.49	0.2
EF19-1.17	0.309	0.046	66.3	2.4	14.09	0.62
EF19-1.18	0.141	0.096	3.68	0.25	1.08	0.14
EF19-1.19	0.203	0.067	25.3	1.9	5.73	0.59
EF19-1.20	2.12	0.16	21.59	0.92	8.15	0.3
EF19-1.21	1.01	0.53	23.6	1.5	6.8	1.5
EF19-1.23	0.83	0.68	1.95	0.18	0.54	0.22
EF19-1.24	0.229	0.041	5.84	0.51	1.4	0.17
EF19-1.25	0.45	0.11	28.6	3.2	7.9	1.1
EF19-1.26	0.465	0.067	35.2	2.1	8.96	0.95
EF19-1.27	0.93	0.14	38.4	1.2	5.52	0.47

Spot #	Si (cps)	Std. Dev (2σ)	S (cps)	Std. Dev (2σ)	Se (cps)	Std. Dev (2σ)	Te (cps)	Std. Dev (2σ)	Hg (cps)	Std. Dev (2σ)
EF19-4										
EF19-4.01	2.76E+07	690000	44700	3000	234	57	9.5	9.2	1200	370
EF19-4.02	2.55E+07	360000	60100	4500	560	100	9.5	9.2	1020	440
EF19-4.03	2.44E+07	680000	53300	3600	10900	2100	12	10	1480	440
EF19-4.04	3.00E+07	720000	76400	4900	900	170	11.6	9.9	2240	680
EF19-4.05	2.68E+07	690000	62300	3200	299	58	0	1	-400	450
EF19-4.06	2.79E+07	920000	97200	8700	551	82	21	16	2700	570
EF19-4.07	2.50E+07	510000	216000	20000	920	150	19	14	4280	680
EF19-4.08	3.04E+07	550000	262000	25000	4530	430	0	1	680	600
EF19-4.09	3.29E+07	1.10E+06	248000	15000	3970	510	0	1	2410	550
EF19-4.10	3.27E+07	1.10E+06	185000	10000	3430	400	24	19	630	590
EF19-4.11	3.25E+07	1.20E+06	91500	4700	940	110	4.8	6.7	-90	500
EF19-4.12	2.80E+07	870000	237000	21000	2550	290	0	1	1220	610

Spot #	Si (cps)	Std. Dev (2σ)	S (cps)	Std. Dev (2σ)	Se (cps)	Std. Dev (2σ)	Te (cps)	Std. Dev (2σ)	Hg (cps)	Std. Dev (2σ)
EF19-4.13	2.29E+07	570000	630000	170000	3540	800	67	36	9000	1200
EF19-4.14	3.07E+07	1.00E+06	244000	18000	2710	340	0	1	2260	530
EF19-4.15	2.91E+07	870000	127000	9700	1380	200	0	1	3280	540
EF19-4.16	1.79E+07	900000	210000	42000	6700	1600	43	25	3570	660
EF19-4.17	3.04E+07	1.10E+06	57600	3400	60	44	33	18	1180	500
EF19-4.18	2.81E+07	1.10E+06	70900	4300	339	65	9.5	9.2	1080	480
EF19-4.19	2.79E+07	700000	48800	3000	44	37	48	61	970	540
EF19-4.20	2.14E+07	400000	124200	8800	415	85	2.4	4.8	990	560
EF19-4.21	2.45E+07	1.40E+06	185000	34000	850	180	0	1	1100	350
EF19-4.22	2.92E+07	1.20E+06	199000	13000	1030	170	57	29	2220	560
EF19-4.23	2.88E+07	830000	200000	15000	1360	220	0	1	2160	600
EF19-4.24	2.76E+07	1.00E+06	69900	3600	60	38	0	1	950	600
EF19-4.25	2.34E+07	670000	75800	6200	1280	540	0	1	1660	500

Spot #	Na (ppm)	Std. Dev (2σ)	Al (ppm)	Std. Dev (2σ)	Cl (ppm)	Std. Dev (2σ)	K (ppm)	Std. Dev (2σ)	Ti (ppm)	Std. Dev (2σ)
EF19-4.01	1926	27	17420	220	982	65	2592	69	218	13
EF19-4.02	8150	300	104700	3200	1029	64	5734	78	222	29
EF19-4.03	3730	140	60300	2100	1062	67	6940	210	349	47
EF19-4.04	4560	250	89700	1300	1020	71	17150	750	359	31
EF19-4.05	2440	140	31500	1600	1030	66	3740	230	110.1	6.2
EF19-4.06	9900	2200	81800	9300	1128	67	6300	290	205	43
EF19-4.07	26100	3400	166000	17000	882	80	9190	670	850	220
EF19-4.08	5750	140	202900	8400	1046	56	80400	4400	1318	96
EF19-4.09	5858	84	155700	3500	999	70	56000	2200	685	35
EF19-4.10	5450	170	130200	2400	916	63	44000	1200	639	44
EF19-4.11	5570	150	129700	2500	936	58	41600	1900	891	20
EF19-4.12	4960	170	167500	2400	1028	73	69800	2200	261	24

Spot #	Na (ppm)	Std. Dev (2σ)	Al (ppm)	Std. Dev (2σ)	Cl (ppm)	Std. Dev (2σ)	K (ppm)	Std. Dev (2σ)	Ti (ppm)	Std. Dev (2σ)
EF19-4.13	4960	170	167500	2400	1028	73	69800	2200	261	24
EF19-4.14	53800	5300	--	--	1230	110	13100	1600	1060	130
EF19-4.15	5940	290	206500	4500	1083	73	88900	2700	910	170
EF19-4.16	5280	130	247000	11000	1090	72	118000	5800	1880	560
EF19-4.17	12100	2000	761000	67000	1180	110	52600	1800	1285	64
EF19-4.18	5850	410	171200	7100	1044	62	67700	5000	427	29
EF19-4.19	6700	300	339000	27000	1247	91	177000	17000	1240	140
EF19-4.20	1021	32	16920	820	1205	67	1242	46	109.5	6.8
EF19-4.21	9860	800	230000	20000	1160	100	15210	460	1770	120
EF19-4.22	10600	2900	240000	34000	1027	98	10500	1500	1120	140
EF19-4.23	11600	1100	499000	40000	948	76	29000	1500	1280	100
EF19-4.24	4570	150	165500	4100	1032	76	62100	2800	740	120
EF19-4.25	2840	130	65700	2800	1105	83	7020	370	44.2	3.8

Spot #	Ti (ppm)	Std. Dev (2σ)	Fe (ppm)	Std. Dev (2σ)	Ni (ppm)	Std. Dev (2σ)	Cu (ppm)	Std. Dev (2σ)	Zn (ppm)	Std. Dev (2σ)
EF19-4.01	19.1	1.1	305	33	0.42	0.27	2.52	0.34	3.77	0.62
EF19-4.02	23.5	2.4	27300	1900	54.9	4.6	112.3	8.6	84.3	8.6
EF19-4.03	31.8	4.4	15400	2300	1.01	0.35	140	24	14.3	4.8
EF19-4.04	33.9	2.7	5840	470	2.79	0.67	14.78	0.98	82.2	8.2
EF19-4.05	9.48	0.33	2530	360	4.64	0.81	11.7	1.4	10.2	1.1
EF19-4.06	23	6.7	10900	2900	26.9	8.5	60	16	390	120
EF19-4.07	92	23	64200	7200	257	55	346	40	1900	180
EF19-4.08	123	8.7	6940	650	3.54	0.69	48.3	5.4	15.3	1.8
EF19-4.09	65.9	3	3170	270	6.4	1.2	41.2	3.2	16.1	3.3
EF19-4.10	56.5	2.8	2140	220	8.6	1	41.9	4.4	9.3	1.3
EF19-4.11	83.4	1.4	1221	68	2.86	0.53	8.48	0.69	17.2	4.2
EF19-4.12	25	2.4	3930	420	6.47	0.81	29.3	3	11.6	1.3

Spot #	Ti (ppm)	Std. Dev (2σ)	Fe (ppm)	Std. Dev (2σ)	Ni (ppm)	Std. Dev (2σ)	Cu (ppm)	Std. Dev (2σ)	Zn (ppm)	Std. Dev (2σ)
EF19-4.13	120	13	123000	12000	357	60	585	45	3660	530
EF19-4.14	86	16	4850	700	7.19	0.87	25.8	3.1	30.3	3.3
EF19-4.15	185	59	5040	820	2.54	0.66	27.1	3.5	16	1.7
EF19-4.16	127.8	6.7	121000	16000	178	30	620	100	960	220
EF19-4.17	41.7	2.4	2450	750	4.1	1.4	19.8	9.6	39.8	4.7
EF19-4.18	118	13	2470	330	1.88	0.67	7.85	0.89	15.5	1.8
EF19-4.19	8.85	0.67	124	77	2.3	1.3	1.51	0.86	7.6	1.9
EF19-4.20	174	11	74600	6000	161	10	335	23	197	35
EF19-4.21	120	18	53000	13000	213	41	439	91	680	150
EF19-4.22	126.9	9.2	22000	3300	134	20	318	40	1010	130
EF19-4.23	72	12	3790	520	2.44	0.75	20.1	3	12.8	2.3
EF19-4.24	3.27	0.3	29	20	1	0.42	0.51	0.21	2.1	2.2
EF19-4.25	6.2	2.4	9000	5100	3.4	1.6	58	31	14.5	5.6

Spot #	As (ppm)	Std. Dev (2σ)	Pd (ppm)	Std. Dev (2σ)	Ag (ppm)	Std. Dev (2σ)	Cd (ppm)	Std. Dev (2σ)	Sn (ppm)	Std. Dev (2σ)
EF19-4.01	20.8	2.1	0	1	36.6	2.3	0.86	1.29	3.3	0.37
EF19-4.02	56.4	6.2	--	--	10.6	1.7	--	--	9.15	0.85
EF19-4.03	1000	110	0	1	13.3	1.3	--	--	2.96	0.52
EF19-4.04	411	38	0.069	0.053	18.7	1.1	0.53	0.23	2.62	0.32
EF19-4.05	20.4	1.8	--	--	9.29	0.98	--	--	2.67	0.26
EF19-4.06	73.1	8.9	--	--	7.65	0.88	0.29	0.18	6.7	1.3
EF19-4.07	159	22	0.014	0.029	23.5	3.1	1.21	0.54	56	13
EF19-4.08	481	47	0.044	0.043	162	33	0.27	0.16	3.71	0.43
EF19-4.09	189	16	0.115	0.061	73	8.2	0.33	0.23	2.74	0.36
EF19-4.10	137	16	0.053	0.045	57.9	7.4	0.66	0.48	2.68	0.27
EF19-4.11	72.4	3.8	0.076	0.054	24.8	4.1	--	--	3.3	0.39
EF19-4.12	218	16	0.023	0.033	66	7.5	--	--	2.4	0.34

Spot #	As (ppm)	Std. Dev (2σ)	Pd (ppm)	Std. Dev (2σ)	Ag (ppm)	Std. Dev (2σ)	Cd (ppm)	Std. Dev (2σ)	Sn (ppm)	Std. Dev (2σ)
EF19-4.13	1480	360	--	--	252	55	1.81	0.58	121	20
EF19-4.14	273	36	0.093	0.061	84	25	--	--	4.04	0.57
EF19-4.15	308	39	0.088	0.062	37.4	3.4	--	--	4.88	0.87
EF19-4.16	5090	930	0.114	0.089	291	56	1.9	1	101	17
EF19-4.17	147	13	0.109	0.074	47.5	1.8	0.59	0.36	4	1.4
EF19-4.18	196	21	0.097	0.068	17.09	0.93	--	--	3.71	0.44
EF19-4.19	10.9	3.2	--	--	8.78	0.68	0.66	0.57	1.44	0.38
EF19-4.20	118.1	7.4	0.094	0.073	31.8	2.7	0.36	0.27	25.7	2.1
EF19-4.21	380	46	0.49	0.22	35.6	6.3	0.81	0.34	175	21
EF19-4.22	488	74	0.141	0.076	29.1	4.8	0.75	0.35	45.9	6.8
EF19-4.23	830	110	0.045	0.043	61.3	9.4	0.26	0.18	2.82	0.46
EF19-4.24	3.8	1.2	0	1	1.31	0.19	--	--	0.78	0.17
EF19-4.25	230	110	0.014	0.028	2.57	0.92	--	--	1.18	0.34

Spot #	Sb (ppm)	Std. Dev (2σ)	Pt (ppm)	Std. Dev (2σ)	Au (ppm)	Std. Dev (2σ)	Tl (ppm)	Std. Dev (2σ)	Pb (ppm)	Std. Dev (2σ)
EF19-4.01	173.6	3.2	0	1	1.05	0.25	1.01	0.14	0.167	0.069
EF19-4.02	77.4	2.7	0.043	0.036	3.53	0.77	1.07	0.17	3.7	4
EF19-4.03	437	45	--	--	3.8	1.2	1.41	0.12	4.16	0.64
EF19-4.04	212	21	--	--	9.1	1.3	2.16	0.17	6.56	0.84
EF19-4.05	121	12	--	--	--	--	0.84	0.096	0.78	0.25
EF19-4.06	226	10	--	--	0.94	0.27	1.39	0.12	4.46	0.86
EF19-4.07	97.7	5.1	--	--	4.2	1.1	2.01	0.16	11.34	0.87
EF19-4.08	131	10	0	1	26.9	1.9	10.8	1.1	20.9	1.7
EF19-4.09	80.3	5.9	--	--	9.8	1.3	11.2	1.1	6.01	0.61
EF19-4.10	79.7	5.4	--	--	6.63	0.72	10.7	1.1	4.8	0.51
EF19-4.11	64.2	1.5	0	1	2.74	0.29	3.77	0.24	4.39	0.47
EF19-4.12	103.2	7.1	--	--	6.39	0.93	10.7	1.2	10.1	1

Spot #	Sb (ppm)	Std. Dev (2σ)	Pt (ppm)	Std. Dev (2σ)	Au (ppm)	Std. Dev (2σ)	Tl (ppm)	Std. Dev (2σ)	Pb (ppm)	Std. Dev (2σ)
EF19-4.13	730	120	--	--	82	17	1.33	0.2	23.6	4.4
EF19-4.14	110.5	8.2	0	1	7.9	0.9	9.51	0.65	8.39	0.96
EF19-4.15	127	12	--	--	23	2.8	7.47	0.42	5.79	0.66
EF19-4.16	4330	780	0.06	0.052	153	23	6.25	0.69	104	18
EF19-4.17	68.7	7.7	--	--	3.51	0.61	5.07	0.43	3.69	0.7
EF19-4.18	99.4	9.6	--	--	3.6	0.55	10.36	0.84	5.1	1
EF19-4.19	148.9	4.2	--	--	0.43	0.17	0.229	0.05	0.67	0.32
EF19-4.20	86	3.6	0	1	4.64	0.56	2.16	0.18	7.7	1.3
EF19-4.21	163.5	7.3	--	--	7.9	1.3	1.16	0.17	29.1	7.5
EF19-4.22	110	11	0.043	0.034	4.8	1.1	3.82	0.25	36.1	4.1
EF19-4.23	84.8	9.5	--	--	23.3	4.1	4.96	0.31	96	11
EF19-4.24	65.1	4.7	--	--	--	--	1.09	0.12	0.097	0.062
EF19-4.25	77	12	--	--	0.41	0.24	0.7	0.18	1.64	0.49

Spot #	Bi (ppm)	Std. Dev (2σ)	Th (ppm)	Std. Dev (2σ)	U (ppm)	Std. Dev (2σ)
EF19-4.01	0.057	0.029	3.7	2	0.51	0.058
EF19-4.02	0.201	0.061	1.77	0.25	0.511	0.078
EF19-4.03	0.098	0.039	3.73	0.81	0.646	0.088
EF19-4.04	0.049	0.023	2.63	0.25	0.481	0.06
EF19-4.05	0.068	0.033	2.34	0.19	0.299	0.041
EF19-4.06	0.42	0.12	1.45	0.46	0.298	0.048
EF19-4.07	1.52	0.22	2.82	0.61	0.88	0.14
EF19-4.08	0.163	0.036	10.3	1.6	1.42	0.15
EF19-4.09	0.052	0.02	8.93	0.43	1.028	0.091
EF19-4.10	0.36	0.27	6.95	0.36	1.55	0.42
EF19-4.11	0.081	0.032	8.45	0.33	1.83	0.41
EF19-4.12	0.081	0.036	3.16	0.25	0.57	0.12

Spot #	Bi (ppm)	Std. Dev (2σ)	Th (ppm)	Std. Dev (2σ)	U (ppm)	Std. Dev (2σ)
EF19-4.13	23.2	8.1	3.36	0.47	5.7	2.6
EF19-4.14	0.184	0.056	6.39	0.67	1.15	0.15
EF19-4.15	0.163	0.044	20.2	7.5	1.49	0.34
EF19-4.16	2.33	0.63	45.7	1.4	4.14	0.37
EF19-4.17	0.26	0.13	4.2	0.27	1.67	0.77
EF19-4.18	0.22	0.16	9.88	0.95	2.52	0.47
EF19-4.19	0.1	0.15	15	21	0.78	0.47
EF19-4.20	0.61	0.13	25.4	0.9	5.48	0.5
EF19-4.21	1.73	0.46	25.9	5.3	3.04	0.46
EF19-4.22	3.45	0.5	9.2	0.87	2.44	0.32
EF19-4.23	0.203	0.044	1.93	0.14	0.71	0.11
EF19-4.24	0.11	0.07	37	29	0.25	0.16
EF19-4.25	0.098	0.038	5.1	8.9	0.28	0.11

Spot #	Si (cps)	Std. Dev (2σ)	S (cps)	Std. Dev (2σ)	Se (cps)	Std. Dev (2σ)	Te (cps)	Std. Dev (2σ)	Hg (cps)	Std. Dev (2σ)
EF19-14										
EF19-14.01	2.78E+07	700000	594000	33000	7500	480	7.1	8	4910	460
EF19-14.02	3.05E+07	550000	744000	70000	10320	540	7.1	8	6050	460
EF19-14.03	2.68E+07	850000	152000	15000	1460	290	10	13	3440	510
EF19-14.04	3.22E+07	1.40E+06	106000	7100	391	76	0	1	3600	510
EF19-14.05	2.37E+07	620000	91900	6000	670	100	0	1	5390	480
EF19-14.06	2.36E+07	570000	119900	3300	1990	150	4.9	6.8	5160	370
EF19-14.07	2.25E+07	650000	101000	4100	2010	140	17	13	5080	470
EF19-14.08	3.10E+07	660000	632000	52000	5060	410	0	1	3670	490
EF19-14.09	2.67E+07	950000	5.06E+06	310000	105600	7500	45	32	22700	1200
EF19-14.10	2.56E+07	1.20E+06	219000	22000	1610	280	7.1	8	4150	430
EF19-14.11	2.96E+07	620000	1.25E+06	150000	10200	1000	12	12	2790	630
EF19-14.12	2.74E+07	560000	135600	5000	1650	180	0	1	2800	540
EF19-14.13	2.65E+07	770000	49500	3600	48	42	0	1	1900	500
EF19-14.14	3.32E+07	840000	725000	63000	6910	420	0	1	23700	3100
EF19-14.15	3.24E+07	520000	79000	4800	482	82	9.5	9.2	4750	650
EF19-14.16	2.60E+07	510000	650000	140000	2740	370	19	16	12270	780
EF19-14.17	2.57E+07	840000	295000	16000	820	110	0	1	5450	690

Spot #	Si (cps)	Std. Dev (2σ)	S (cps)	Std. Dev (2σ)	Se (cps)	Std. Dev (2σ)	Te (cps)	Std. Dev (2σ)	Hg (cps)	Std. Dev (2σ)
EF19-14.18	2.88E+07	650000	2.99E+06	160000	27200	1400	21	13	8550	820
EF19-14.19	2.65E+07	560000	5.74E+06	470000	62300	5400	16	11	17400	1200
EF19-14.20	1.81E+07	650000	128500	9600	1410	290	102	39	12090	950
EF19-14.21	2.50E+07	1.10E+06	136000	17000	1960	190	33	28	16000	1400
EF19-14.22	2.82E+07	820000	318000	16000	2270	200	14	13	4680	460
EF19-14.23	2.42E+07	620000	1.30E+06	170000	9460	810	44	20	7700	690
EF19-14.24	2.47E+07	220000	124900	6000	724	83	9.8	9.4	3390	600
EF19-14.25	3.28E+07	550000	294000	20000	1130	130	9.5	9.2	1750	550
EF19-14.26	2.94E+07	510000	168000	6600	650	130	14	11	5420	680
EF19-14.27	2.72E+07	800000	2.99E+06	110000	39500	2600	79	27	21600	1500
EF19-14.28	2.58E+07	1.10E+06	1.83E+06	270000	7940	900	9.5	9.2	7050	810
EF19-14.29	1.97E+07	270000	183000	13000	680	130	21	13	1710	720
EF19-14.30	3.14E+07	500000	171200	4300	6150	260	7.3	8.2	4960	560
EF19-14.31	2.94E+07	720000	407000	49000	2050	300	0	1	3060	670
EF19-14.32	2.68E+07	930000	660000	100000	24800	1700	26	14	40800	3400
EF19-14.33	2.61E+07	550000	5.03E+06	200000	121800	4700	14	11	23900	1400
EF19-14.34	2.78E+07	440000	489000	23000	5110	310	0	1	2540	730
EF19-14.35	2.63E+07	530000	229000	6000	2140	150	0	1	4130	450

Spot #	Na (ppm)	Std. Dev (2σ)	Al (ppm)	Std. Dev (2σ)	Cl (ppm)	Std. Dev (2σ)	K (ppm)	Std. Dev (2σ)	Ti (ppm)	Std. Dev (2σ)
EF19-14.01	5440	150	299000	17000	1052	77	193000	15000	3720	370
EF19-14.02	9710	330	784000	13000	1360	81	584000	13000	19280	880
EF19-14.03	5790	290	484000	15000	1188	78	311000	13000	12700	2500
EF19-14.04	3660	140	80200	2400	875	65	14380	970	1531	66
EF19-14.05	3610	120	355000	15000	1176	72	196000	11000	6400	300
EF19-14.06	7870	380	--	--	1557	93	831000	12000	17060	390
EF19-14.07	9460	190	--	--	1673	87	850000	17000	34730	970
EF19-14.08	6100	180	524000	12000	977	52	389000	11000	7730	380
EF19-14.09	11710	300	688000	11000	1200	60	489100	9000	21320	560
EF19-14.10	6210	120	720000	21000	1293	69	508000	14000	4550	420
EF19-14.11	6440	320	396000	17000	1051	77	262000	16000	3360	310
EF19-14.12	6880	150	583000	10000	1203	75	401000	12000	5050	310
EF19-14.13	1943	78	85870	880	960	59	4100	260	55.3	4
EF19-14.14	7090	160	418100	9700	1042	66	310200	5900	27210	690
EF19-14.15	5646	93	323200	4500	1028	62	196500	3400	3580	100
EF19-14.16	4780	170	398000	14000	1101	60	237000	10000	25700	5100
EF19-14.17	6070	130	400200	8100	1101	70	267100	6300	14290	610

Spot #	Na (ppm)	Std. Dev (2σ)	Al (ppm)	Std. Dev (2σ)	Cl (ppm)	Std. Dev (2σ)	K (ppm)	Std. Dev (2σ)	Ti (ppm)	Std. Dev (2σ)
EF19-14.18	7180	150	466700	7200	1077	54	332900	8400	35410	930
EF19-14.19	9360	270	563000	11000	1172	62	399900	7000	32900	1200
EF19-14.20	3680	320	468000	46000	2950	210	188100	9900	14500	5400
EF19-14.21	4480	340	389900	9600	2250	190	222100	7000	4220	810
EF19-14.22	5770	120	373500	4600	1126	78	250000	3900	12800	170
EF19-14.23	5530	170	407000	11000	1163	63	252100	6400	17000	2700
EF19-14.24	3026	87	563000	12000	3870	230	346800	7600	1820	140
EF19-14.25	3901	95	93300	1000	905	53	12800	260	31500	610
EF19-14.26	5480	120	221500	9900	991	61	107800	8300	2414	63
EF19-14.27	5200	120	364000	10000	1350	85	218100	8300	24710	850
EF19-14.28	357000	75000	488000	16000	5120	340	270000	11000	78000	15000
EF19-14.29	5810	290	--	--	2350	110	723000	35000	13300	2000
EF19-14.30	6015	84	512100	7000	1292	52	375900	4900	16190	390
EF19-14.31	4670	390	106800	2100	987	57	29000	1000	7750	480
EF19-14.32	5020	170	415000	14000	1231	67	272000	12000	44000	11000
EF19-14.33	10480	290	746000	18000	1379	67	560000	12000	15800	530
EF19-14.34	6080	120	574500	7200	1244	68	413600	6000	18690	730
EF19-14.35	7490	140	771600	9400	1407	62	579000	8400	12460	370

Spot #	Ti (ppm)	Std. Dev (2σ)	Fe (ppm)	Std. Dev (2σ)	Ni (ppm)	Std. Dev (2σ)	Cu (ppm)	Std. Dev (2σ)	Zn (ppm)	Std. Dev (2σ)
EF19-14.01	369	39	13500	1300	7.4	1	96.1	9.1	35.9	2.8
EF19-14.02	2122	81	46700	1500	16.1	1.8	218	5.6	72.4	5
EF19-14.03	1400	280	5640	580	3.9	1.1	36.1	4.3	11.2	1.5
EF19-14.04	151.6	6.9	1380	320	2.94	0.62	14.2	3.2	7.2	1
EF19-14.05	705	40	15190	720	4.2	1.1	55.2	2.8	31.7	3.7
EF19-14.06	1932	45	52680	820	7.7	1.6	172.8	3.8	79.4	6.7
EF19-14.07	3950	110	74200	3500	9.3	1.3	212.6	7.6	111	6
EF19-14.08	882	44	11580	530	10.6	1.1	89.3	4	27.3	2.3
EF19-14.09	2416	67	56400	2600	64.9	3.7	782	23	50.7	3.1
EF19-14.10	486	54	22000	1600	5.22	0.87	63.7	4.7	37.4	2.9
EF19-14.11	359	39	11550	870	8.22	0.99	111.1	6	30.3	2
EF19-14.12	567	38	16680	430	4.2	0.67	97.8	3.6	48.2	2.7
EF19-14.13	5.64	0.26	2620	150	1.35	0.4	9.1	1.2	4.78	0.88
EF19-14.14	3017	57	41100	1600	14.7	1.4	363	18	111.1	5.1
EF19-14.15	391	18	4780	330	1.8	0.43	20.5	1.4	14.5	1.7
EF19-14.16	2780	480	115200	9800	25.4	2.1	484	36	443	42
EF19-14.17	1645	75	3240	280	8.3	0.91	62.7	5.2	98	20

Spot #	Ti (ppm)	Std. Dev (2σ)	Fe (ppm)	Std. Dev (2σ)	Ni (ppm)	Std. Dev (2σ)	Cu (ppm)	Std. Dev (2σ)	Zn (ppm)	Std. Dev (2σ)
EF19-14.18	3990	62	42100	950	30.3	1.7	321.7	7.8	22.1	1.9
EF19-14.19	3780	110	62400	5400	54	8.4	810	120	85	26
EF19-14.20	1640	620	100000	19000	16.1	3.1	272	53	248	44
EF19-14.21	467	96	102000	11000	8.6	1.6	244	20	154.6	8.4
EF19-14.22	1471	16	8840	160	6.68	0.75	58.9	2	53.3	2.4
EF19-14.23	1940	290	275000	31000	23.4	2.6	606	64	256	38
EF19-14.24	181	15	72500	3300	33.8	2.9	200.6	6.6	134	10
EF19-14.25	3570	52	4380	320	2.99	0.49	16.4	2.2	21.2	1.9
EF19-14.26	237.7	5.8	2530	330	2.76	0.51	11.6	1	8.78	0.96
EF19-14.27	2808	96	352000	26000	62.1	4.1	2360	200	174	11
EF19-14.28	7900	1500	19400	1400	18	2.1	191	14	278	21
EF19-14.29	1580	250	58800	4100	25.9	3.1	198	17	115.1	8.5
EF19-14.30	1857	49	16970	930	7.22	0.92	284	7.6	19.9	1.3
EF19-14.31	874	54	5990	710	4.86	0.9	47.4	5.4	68	12
EF19-14.32	4600	1000	288000	15000	29.5	2.2	1918	93	118.8	6
EF19-14.33	1786	60	59300	3100	43.5	2.9	637	22	27.8	2.1
EF19-14.34	2078	65	22240	520	11.5	0.98	199.6	4.8	157.9	6.9
EF19-14.35	1391	40	23850	730	10.96	0.94	84.2	3.4	94.6	5.7

Spot #	As (ppm)	Std. Dev (2σ)	Pd (ppm)	Std. Dev (2σ)	Ag (ppm)	Std. Dev (2σ)	Cd (ppm)	Std. Dev (2σ)	Sn (ppm)	Std. Dev (2σ)
EF19-14.01	864	76	0.41	0.13	123.9	8.3	0.4	0.22	7.48	0.69
EF19-14.02	2043	66	0.4	0.12	217.9	9.7	1.29	0.36	68.2	2.4
EF19-14.03	187	24	0.126	0.076	108.7	9.3	0.43	0.26	12.1	1.8
EF19-14.04	72	16	0.079	0.056	6.3	1.5	--	--	3.42	0.63
EF19-14.05	321	14	0.2	0.14	66.8	4.9	--	--	8.28	0.78
EF19-14.06	1095	30	0.36	0.17	191.5	5.1	--	--	24.1	1.6
EF19-14.07	1499	61	0.73	0.25	150.5	5.5	0.96	0.42	42.8	1.7
EF19-14.08	455	17	0.45	0.17	219.1	7.8	1.8	1.8	12.23	0.76
EF19-14.09	3540	140	0.28	0.14	9650	600	0.9	0.35	17.9	1.1
EF19-14.10	651	43	0.06	0.058	128	19	0.77	0.28	8.45	0.72
EF19-14.11	573	32	0.203	0.097	228	23	0.58	0.29	6.75	0.89
EF19-14.12	1014	32	0.22	0.12	95.6	3.8	0.49	0.31	16.6	2.7
EF19-14.13	51.5	2.6	--	--	80.3	2.8	--	--	0.9	0.18
EF19-14.14	2647	72	0.42	0.14	283	35	1.21	0.3	27.2	1.9
EF19-14.15	284	21	0.135	0.086	91.5	2.5	0.29	0.15	6.6	0.56
EF19-14.16	1700	180	0.11	0.071	49.3	8.3	0.68	0.31	16.7	2.1
EF19-14.17	172	14	0.54	0.2	221	23	1.77	0.96	19.8	1.1

Spot #	As (ppm)	Std. Dev (2σ)	Pd (ppm)	Std. Dev (2σ)	Ag (ppm)	Std. Dev (2σ)	Cd (ppm)	Std. Dev (2σ)	Sn (ppm)	Std. Dev (2σ)
EF19-14.18	3900	100	0.49	0.14	1353	93	0.55	0.32	19.14	0.77
EF19-14.19	4520	300	0.23	0.11	1630	150	22	12	47	16
EF19-14.20	2500	440	0.2	0.13	34.1	2.6	1.31	0.49	17.8	2.8
EF19-14.21	2380	200	0.4	0.16	69.6	3.4	1.45	0.43	18.2	2.8
EF19-14.22	983	20	0.34	0.15	188.6	7.4	0.98	0.4	10.01	0.55
EF19-14.23	10500	1100	0.37	0.15	289	22	4.6	1	51.3	4.7
EF19-14.24	1071	66	0	1	31.7	1.6	0.73	0.34	16.06	0.9
EF19-14.25	165	23	0.38	0.14	427.9	9.6	0.69	0.32	18.74	0.9
EF19-14.26	97	12	0.099	0.064	316	14	0.42	0.22	5.26	0.88
EF19-14.27	13160	940	1.14	0.23	219	35	4.79	0.88	66.8	4
EF19-14.28	4000	510	1.43	0.32	435	24	1.63	0.52	35.1	3
EF19-14.29	801	49	0.86	0.24	224	14	3.4	1	20.5	2.5
EF19-14.30	1333	45	0.113	0.078	226.8	5	1.1	0.38	14.2	0.7
EF19-14.31	355	45	0.42	0.16	68.6	7.5	3.8	1.7	9.4	0.58
EF19-14.32	9390	580	0.47	0.16	166.7	7.9	2.26	0.56	63.9	7.3
EF19-14.33	3560	210	0.18	0.11	6440	300	0.88	0.35	14.7	0.57
EF19-14.34	1469	35	0.8	0.2	127.3	5.7	1.85	0.52	26.6	1.2
EF19-14.35	1378	47	0.22	0.11	91.5	2.2	0.63	0.28	12.36	0.68

Spot #	Sb (ppm)	Std. Dev (2σ)	Pt (ppm)	Std. Dev (2σ)	Au (ppm)	Std. Dev (2σ)	Tl (ppm)	Std. Dev (2σ)	Pb (ppm)	Std. Dev (2σ)
EF19-14.01	238	17	--	--	48.2	4.4	14.2	1.1	97.2	7
EF19-14.02	1087	32	0.046	0.035	98.4	7.9	31.8	1.4	385	18
EF19-14.03	100	11	0.056	0.04	24.6	2.4	13.51	0.72	61	7.7
EF19-14.04	163.2	6.5	--	--	0.71	0.23	1.8	0.14	11.2	2.1
EF19-14.05	198.6	6.6	0.055	0.042	7.56	0.54	6.45	0.48	29	2.6
EF19-14.06	555	13	--	--	17.39	0.92	22.03	0.71	92.5	4.5
EF19-14.07	928	40	0.114	0.067	24.5	1	24.19	0.66	130	15
EF19-14.08	210	10	--	--	10.56	0.99	18.56	0.66	119	6.4
EF19-14.09	671	36	0.056	0.04	113.4	4.4	197	11	179.4	6.4
EF19-14.10	301	18	0.028	0.027	20.3	1.4	21.01	0.83	153	14
EF19-14.11	142.4	8.3	0.021	0.024	21.7	2	27.5	2.6	59.2	8
EF19-14.12	256.1	8	0.064	0.042	27.5	1.7	16.54	0.69	91.7	3.3
EF19-14.13	68.3	1.6	--	--	1.66	0.21	0.543	0.066	2.47	0.43
EF19-14.14	439	14	0.097	0.056	129.6	4.8	12.36	0.48	177.3	5.1
EF19-14.15	76.2	3.7	0.047	0.033	8.71	0.85	9.79	0.29	23.6	1.5
EF19-14.16	236	24	--	--	4.24	0.65	18.36	0.91	562	94
EF19-14.17	74.8	2.6	0.067	0.044	1.39	0.23	19.11	0.52	82.1	3.3

Spot #	Sb (ppm)	Std. Dev (2σ)	Pt (ppm)	Std. Dev (2σ)	Au (ppm)	Std. Dev (2σ)	Tl (ppm)	Std. Dev (2σ)	Pb (ppm)	Std. Dev (2σ)
EF19-14.18	602	17	0.11	0.066	97.6	2	97.3	3.7	344	10
EF19-14.19	682	47	0.056	0.039	124.9	8.5	199	14	520	140
EF19-14.20	322	44	--	--	1.58	0.58	13.25	0.72	191	26
EF19-14.21	301	22	0.093	0.058	1.95	0.7	14.14	0.72	182	10
EF19-14.22	163	3	0.054	0.038	20.31	0.79	11.69	0.37	219.8	8.1
EF19-14.23	2180	170	0.071	0.046	30.6	4.6	16.98	0.54	3320	410
EF19-14.24	479	26	0	1	0.51	0.19	21.95	0.74	85.1	7.1
EF19-14.25	108.7	1.9	0.13	0.051	1.17	0.29	1.53	0.11	56.8	7.6
EF19-14.26	56.4	2.8	0.05	0.035	1.72	0.32	8.12	0.62	20.7	1.4
EF19-14.27	1230	75	0.122	0.061	115	43	15.13	0.4	1660	150
EF19-14.28	387	47	0.147	0.075	37.9	4.1	11.88	0.7	423	52
EF19-14.29	662	37	--	--	2.16	0.42	47.1	2.8	132	13
EF19-14.30	154.1	5.8	0.035	0.03	37.8	2	13.4	0.42	119.2	5.3
EF19-14.31	88.1	4.9	0.55	0.21	2.67	0.38	3.49	0.33	63.2	6
EF19-14.32	982	40	0.146	0.074	51.4	2.6	19.73	0.9	468	27
EF19-14.33	615	32	--	--	121.1	6.4	194.4	8.3	171.2	9
EF19-14.34	365	11	0.047	0.036	39.1	1.6	16.41	0.41	139.9	3.5
EF19-14.35	349	14	--	--	34.2	2.1	23.49	0.51	191.7	4.5

Spot #	Bi (ppm)	Std. Dev (2σ)	Th (ppm)	Std. Dev (2σ)	U (ppm)	Std. Dev (2σ)
EF19-14.01	0.364	0.075	21.5	2.2	6.1	1.2
EF19-14.02	1.87	0.13	69.9	2.7	18.46	0.82
EF19-14.03	0.9	0.16	27.7	4	9.5	2.5
EF19-14.04	0.181	0.048	14.3	1.4	3.01	0.33
EF19-14.05	0.302	0.049	49	2.3	15.16	0.91
EF19-14.06	1.13	0.41	92.5	2.8	26.3	0.82
EF19-14.07	1.168	0.084	144.6	9.9	55.3	5.9
EF19-14.08	0.58	0.31	40.9	2.4	11.99	0.9
EF19-14.09	2.13	0.12	57.9	4.8	19.5	3.2
EF19-14.10	0.86	0.41	23	1.6	5.86	0.45
EF19-14.11	0.283	0.046	15.3	1.7	4.75	0.58
EF19-14.12	0.591	0.08	38.5	3.5	7.78	0.56
EF19-14.13	0.062	0.025	0.433	0.063	0.236	0.043
EF19-14.14	1.78	0.13	75.4	1.9	21.64	0.55
EF19-14.15	0.236	0.032	23.97	0.9	5.96	0.28
EF19-14.16	3.07	0.54	51	4.3	22.6	3.7
EF19-14.17	0.84	0.11	103.7	2.9	25.27	0.98

Spot #	Bi (ppm)	Std. Dev (2σ)	Th (ppm)	Std. Dev (2σ)	U (ppm)	Std. Dev (2σ)
EF19-14.18	3.23	0.19	74.8	1.4	24.53	0.38
EF19-14.19	3.3	0.29	76.6	2.8	24.11	0.7
EF19-14.20	1.3	0.34	29.6	3.9	12.3	1.3
EF19-14.21	0.83	0.11	54.7	9.9	21.2	3.2
EF19-14.22	0.86	0.24	35.95	0.78	12.7	3.7
EF19-14.23	11.5	1.2	72.1	3.7	20.2	1.4
EF19-14.24	--	--	14	1	6.13	0.37
EF19-14.25	0.769	0.095	30.9	1.9	13.1	1
EF19-14.26	0.238	0.052	16.97	0.7	3.72	0.21
EF19-14.27	18	1.2	133.7	4.8	39.5	2.9
EF19-14.28	2.18	0.25	197	23	55.2	7.8
EF19-14.29	2.09	0.23	40.3	3.9	19.7	1.8
EF19-14.30	1.281	0.084	53.9	1.3	14.47	0.39
EF19-14.31	0.77	0.12	540	180	295	97
EF19-14.32	12.8	1.1	123.2	6.4	52.5	4
EF19-14.33	2.05	0.16	42.3	2.2	12.38	0.41
EF19-14.34	0.85	0.1	76.6	4.5	19.5	1.3
EF19-14.35	1.108	0.094	35.5	1.4	10.57	0.38

Spot #	**Si (cps)**	**Std. Dev (2σ)**	**S (cps)**	**Std. Dev (2σ)**	**Se (cps)**	**Std. Dev (2σ)**	**Te (cps)**	**Std. Dev (2σ)**	**Hg (cps)**	**Std. Dev (2σ)**
EF19-20										
EF19-20.01	3.47E+07	780000	174600	8300	68	35	69	35	63900	3500
EF19-20.02	2.77E+07	1.00E+06	76500	7200	150	57	71	57	11400	1200
EF19-20.03	2.73E+07	720000	137000	13000	50	31	40	26	8270	510
EF19-20.04	2.66E+07	660000	156000	13000	67	34	74	67	5280	700
EF19-20.05	2.73E+07	540000	104500	5400	98	34	14	11	8060	470
EF19-20.06	2.78E+07	940000	132900	6600	75	34	44	30	3050	480
EF19-20.07	2.75E+07	480000	105900	6800	79	35	14	17	4450	390
EF19-20.08	2.38E+07	480000	236800	8700	247	56	1560	370	112600	9500
EF19-20.09	2.59E+07	590000	1.05E+06	230000	156	49	12	12	11000	1500
EF19-20.10	2.80E+07	1.10E+06	59600	4400	18	22	14	11	9040	570
EF19-20.11	1.86E+07	570000	34400	2500	20	25	16	11	5430	510
EF19-20.12	2.54E+07	770000	64500	9100	59	35	12	12	13000	1400

Spot #	Si (cps)	Std. Dev (2σ)	S (cps)	Std. Dev (2σ)	Se (cps)	Std. Dev (2σ)	Te (cps)	Std. Dev (2σ)	Hg (cps)	Std. Dev (2σ)
EF19-20.13	2.66E+07	960000	42500	3700	107	41	24	19	6730	470
EF19-20.14	2.80E+07	1.10E+06	219000	86000	70	28	0	1	4600	580
EF19-20.15	3.38E+07	1.10E+06	307000	20000	1410	150	11.6	9.9	33900	1800
EF19-20.16	2.61E+07	930000	78300	7800	278	87	40	37	22400	1400
EF19-20.17	2.57E+07	890000	140000	17000	51	34	14	11	4920	440
EF19-20.18	2.67E+07	710000	73900	5200	135	54	12	10	13200	2200
EF19-20.19	2.43E+07	650000	272000	44000	357	89	2.4	4.8	79900	7400
EF19-20.20	2.12E+07	840000	42100	3800	49	30	26	26	4150	580
EF19-20.21	2.79E+07	1.20E+06	60200	3400	4	20	0	1	5000	460
EF19-20.22	2.80E+07	1.10E+06	92000	14000	49	28	0	1	8500	690
EF19-20.23	2.61E+07	1.20E+06	160000	46000	299	89	230	130	123000	23000
EF19-20.24	2.46E+07	1.00E+06	197000	30000	570	100	53	27	153000	18000
EF19-20.25	3.07E+07	1.10E+06	156000	22000	103	36	4.8	6.7	4860	650

Spot #	Na (ppm)	Std. Dev (2σ)	Al (ppm)	Std. Dev (2σ)	Cl (ppm)	Std. Dev (2σ)	K (ppm)	Std. Dev (2σ)	Ti (ppm)	Std. Dev (2σ)
EF19-20.01	3170	530	26400	4800	791	49	977	58	666	34
EF19-20.02	4100	2200	5170	890	914	65	1440	180	133	17
EF19-20.03	3190	310	14440	430	929	52	4080	130	109.7	7.3
EF19-20.04	4300	1500	22780	380	974	62	6490	160	192.7	9.2
EF19-20.05	4450	970	24490	470	1038	57	5210	77	253	13
EF19-20.06	4500	1800	17360	250	909	60	5324	91	261	14
EF19-20.07	3910	840	18140	260	971	61	5572	90	286	18
EF19-20.08	11300	1500	240000	63000	981	78	16160	830	2070	140
EF19-20.09	2136	87	8700	220	939	56	2205	69	218	12
EF19-20.10	1320	160	7480	320	870	60	1956	76	106	5.3
EF19-20.11	11.9	7.8	1196	91	1013	94	8.6	3.2	26.7	2.8
EF19-20.12	2500	370	18140	850	1022	54	4710	320	625	72

Spot #	Na (ppm)	Std. Dev (2σ)	Al (ppm)	Std. Dev (2σ)	Cl (ppm)	Std. Dev (2σ)	K (ppm)	Std. Dev (2σ)	Ti (ppm)	Std. Dev (2σ)
EF19-20.13	2296	44	22460	400	1093	73	5430	170	1023	68
EF19-20.14	3450	120	42540	540	1005	61	9450	180	167	13
EF19-20.15	2460	100	8330	400	996	64	1545	35	1760	220
EF19-20.16	3300	2600	16200	1100	1025	73	3140	300	1119	39
EF19-20.17	1349	91	4390	190	1116	79	896	11	121.8	4.7
EF19-20.18	1350	160	5750	220	1157	73	1180	59	130	14
EF19-20.19	295	42	1850	210	1141	77	209	11	827	57
EF19-20.20	209	38	3789	80	1144	91	219.6	8.3	35.4	3.9
EF19-20.21	2610	340	12640	410	1012	61	4084	67	594	30
EF19-20.22	2060	230	15120	470	982	66	3180	100	112	24
EF19-20.23	8700	2900	264000	31000	1280	290	3800	1100	352	74
EF19-20.24	8800	1900	640000	140000	1110	80	4640	750	1260	220
EF19-20.25	1990	110	11080	890	952	56	2630	140	90	8.7

Spot #	Ti (ppm)	Std. Dev (2σ)	Fe (ppm)	Std. Dev (2σ)	Ni (ppm)	Std. Dev (2σ)	Cu (ppm)	Std. Dev (2σ)	Zn (ppm)	Std. Dev (2σ)
EF19-20.01	69.9	3.5	5330	360	4.6	0.93	59.5	4.6	232	17
EF19-20.02	14.1	1.9	10200	1400	4.9	4.4	7.1	1.1	20.5	5.2
EF19-20.03	45.3	5.5	1870	290	7.9	6.8	29.5	4.7	13.4	2.3
EF19-20.04	24.79	0.62	1230	260	3.27	0.62	9.4	1.1	12.7	2.3
EF19-20.05	90.1	2.1	4600	110	2.7	1.1	11.3	1.6	143.5	9.6
EF19-20.06	65.1	3.3	1430	350	9.8	5	--	--	14.6	1.5
EF19-20.07	121.6	4.1	2277	77	1.21	0.36	4	1.1	48.2	4.7
EF19-20.08	226	18	27600	3900	71	11	461	24	695	82
EF19-20.09	22.8	0.69	9700	2500	2.16	0.64	3.8	1.1	5.3	1.1
EF19-20.10	8.99	0.43	297	24	1.44	0.52	2.3	0.37	4.6	1.2
EF19-20.11	0.171	0.044	19.4	6.8	--	--	--	--	1.55	0.69
EF19-20.12	62.6	7.5	720	220	1.39	0.95	0.96	0.33	3.3	1

Spot #	Ti (ppm)	Std. Dev (2σ)	Fe (ppm)	Std. Dev (2σ)	Ni (ppm)	Std. Dev (2σ)	Cu (ppm)	Std. Dev (2σ)	Zn (ppm)	Std. Dev (2σ)
EF19-20.13	112.9	6.7	824	64	--	--	1.12	0.32	2.4	0.47
EF19-20.14	16.5	1.6	1620	600	1.02	0.38	4.32	0.49	7.7	1.3
EF19-20.15	181	23	27800	2900	3.38	0.83	14.5	1.2	20.9	1.9
EF19-20.16	108.7	2.9	5520	550	4.4	2.2	8.9	4	31.7	4
EF19-20.17	10.23	0.42	560	140	0.91	0.57	1.45	0.71	2.1	1.2
EF19-20.18	12.2	1.3	3300	1200	4.9	4.1	2.73	0.33	6.4	1.2
EF19-20.19	80.6	6.1	4780	490	1.21	0.38	10.6	0.94	27	3.3
EF19-20.20	1.51	0.24	111	28	0.61	0.34	0.39	0.31	5.3	1.1
EF19-20.21	57.8	2.4	572	44	1.32	0.38	1.35	0.54	3.4	0.89
EF19-20.22	8.22	0.99	870	280	1.76	0.68	1.56	0.48	2.34	0.86
EF19-20.23	55	25	8500	1600	256	68	133	27	473	71
EF19-20.24	148	29	22300	5400	430	140	177	30	970	190
EF19-20.25	10	1.1	2590	660	1.17	0.59	1.91	0.55	4.92	0.97

Spot #	As (ppm)	Std. Dev (2σ)	Pd (ppm)	Std. Dev (2σ)	Ag (ppm)	Std. Dev (2σ)	Cd (ppm)	Std. Dev (2σ)	Sn (ppm)	Std. Dev (2σ)
EF19-20.01	32.9	4.6	0.042	0.041	5.23	0.77	2.2	1.2	6.8	1.4
EF19-20.02	145	17	0.097	0.063	4.1	3.7	5.2	4	4.2	2.8
EF19-20.03	11.8	1.8	0.155	0.081	4.2	3.7	5.2	3.1	1.71	0.77
EF19-20.04	13.8	3.2	0.053	0.051	--	--	0.76	0.54	7.5	7.8
EF19-20.05	--	--	0.35	0.12	--	--	1.14	0.41	1.54	0.37
EF19-20.06	10.7	3	0.136	0.088	0.61	0.46	1.3	1.2	2.1	1.4
EF19-20.07	5.8	1.8	0.39	0.14	2.9	2.5	1.16	0.38	3.2	2.1
EF19-20.08	57.1	3.5	0.147	0.091	22.4	1.6	1.41	0.49	244	16
EF19-20.09	95	24	--	--	0.24	0.21	0.69	0.47	1.32	0.75
EF19-20.10	4.55	0.95	0	1	0.9	0.78	--	--	1.1	0.25
EF19-20.11	4.4	1.5	0	1	--	--	--	--	0.82	0.23
EF19-20.12	9.4	2.4	--	--	0.46	0.3	--	--	1.57	0.49

Spot #	As (ppm)	Std. Dev (2σ)	Pd (ppm)	Std. Dev (2σ)	Ag (ppm)	Std. Dev (2σ)	Cd (ppm)	Std. Dev (2σ)	Sn (ppm)	Std. Dev (2σ)
EF19-20.13	7.11	0.75	0.091	0.064	--	--	--	--	1.94	0.35
EF19-20.14	5.7	1.3	--	--	--	--	--	--	1.31	0.29
EF19-20.15	410	64	0.056	0.048	0.239	0.096	0.47	0.24	1.68	0.23
EF19-20.16	70.5	8.5	--	--	0.99	1.16	4.9	5.1	4.1	3
EF19-20.17	10	2.6	--	--	--	--	0.56	0.37	1.06	0.27
EF19-20.18	47	16	0.011	0.023	0.38	0.19	0.55	0.5	1.03	0.22
EF19-20.19	120	21	0.108	0.07	--	--	--	--	2.61	0.39
EF19-20.20	4.3	1.1	0	1	--	--	--	--	0.89	0.2
EF19-20.21	5.6	1.2	0	1	0.87	0.6	--	--	1.76	0.23
EF19-20.22	8.3	2.4	--	--	0.46	0.39	--	--	1.03	0.25
EF19-20.23	43.3	8.7	0.067	0.057	17.8	6	7.9	5.9	44.6	6.8
EF19-20.24	124	21	0.046	0.052	15	3.3	1.67	0.91	44	10
EF19-20.25	18.5	4.4	0	1	0.32	0.16	0.53	0.27	1	0.24

Spot #	Sb (ppm)	Std. Dev (2σ)	Pt (ppm)	Std. Dev (2σ)	Au (ppm)	Std. Dev (2σ)	Tl (ppm)	Std. Dev (2σ)	Pb (ppm)	Std. Dev (2σ)
EF19-20.01	568	16	0.033	0.034	0.38	0.14	0.5	0.34	5.25	0.74
EF19-20.02	214	16	0.039	0.039	0.7	0.33	0.34	0.2	5.1	2
EF19-20.03	106.7	3.6	0.087	0.061	0.26	0.23	0.38	0.31	1.63	0.97
EF19-20.04	110.3	2.6	0	1	--	--	0.292	0.081	1.29	0.35
EF19-20.05	209.4	3.6	0.016	0.022	--	--	0.41	0.23	3.05	0.86
EF19-20.06	182.3	5.8	--	--	0.39	0.35	0.62	0.32	4	3
EF19-20.07	180.3	4.9	0.037	0.032	--	--	0.29	0.15	2.24	0.85
EF19-20.08	196.1	4.8	--	--	3.05	0.33	0.964	0.09	29.7	3.4
EF19-20.09	206	27	--	--	0.58	0.21	3.81	0.74	2.87	0.62
EF19-20.10	109.3	2.9	--	--	--	--	0.227	0.065	0.22	0.083
EF19-20.11	12.42	0.7	0	1	--	--	--	--	0.112	0.095
EF19-20.12	116	17	--	--	--	--	0.334	0.071	1.35	0.31

Spot #	Sb (ppm)	Std. Dev (2σ)	Pt (ppm)	Std. Dev (2σ)	Au (ppm)	Std. Dev (2σ)	Tl (ppm)	Std. Dev (2σ)	Pb (ppm)	Std. Dev (2σ)
EF19-20.13	119.6	4	0.033	0.032	--	--	0.352	0.053	6.1	1
EF19-20.14	51.8	2.5	--	--	--	--	0.98	0.24	1.68	0.52
EF19-20.15	1264	80	--	--	0.32	0.12	0.64	0.16	11.3	1.4
EF19-20.16	200	30	0.062	0.068	--	--	0.31	0.12	8.4	2.9
EF19-20.17	149.4	3.8	--	--	--	--	0.48	0.25	0.45	0.24
EF19-20.18	351	80	--	--	--	--	0.09	0.05	1.17	0.4
EF19-20.19	298	30	0	1	--	--	0.169	0.048	2.9	0.48
EF19-20.20	23	1.1	--	--	--	--	--	--	0.09	0.085
EF19-20.21	92.6	3.4	--	--	--	--	0.122	0.049	0.59	0.33
EF19-20.22	92.2	3.2	--	--	--	--	0.223	0.071	0.64	0.41
EF19-20.23	68	6.6	0.3	0.14	2.41	0.85	1.87	0.92	27	11
EF19-20.24	166	22	--	--	4.42	0.9	1.2	0.23	32.6	5.5
EF19-20.25	114.1	5.4	--	--	--	--	0.218	0.082	0.69	0.2

Spot #	Bi (ppm)	Std. Dev (2σ)	Th (ppm)	Std. Dev (2σ)	U (ppm)	Std. Dev (2σ)
EF19-20.01	1.32	0.72	10.82	0.59	9.4	6.3
EF19-20.02	1.9	1.9	0.64	0.35	4.8	3.7
EF19-20.03	4.8	6.5	2.35	0.81	3.5	2.1
EF19-20.04	1.5	1.7	1.37	0.15	0.87	0.24
EF19-20.05	0.199	0.084	2.74	0.27	8.3	3.9
EF19-20.06	0.65	0.45	2.19	0.21	1.64	0.16
EF19-20.07	0.139	0.053	1.5	0.14	3.65	0.32
EF19-20.08	1.67	0.35	11.39	0.98	14.7	1
EF19-20.09	0.25	0.14	1.045	0.095	0.27	0.06
EF19-20.10	0.078	0.034	0.92	0.53	0.155	0.04
EF19-20.11	0.107	0.037	0.13	0.2	0.23	0.41
EF19-20.12	1.3	2.2	4.53	0.6	1.41	0.4

Spot #	Bi (ppm)	Std. Dev (2σ)	Th (ppm)	Std. Dev (2σ)	U (ppm)	Std. Dev (2σ)
EF19-20.13	0.065	0.027	16.3	1.1	1.4	0.15
EF19-20.14	0.3	0.28	1.35	0.11	0.308	0.045
EF19-20.15	0.563	0.083	1.098	0.089	1.82	0.4
EF19-20.16	0.87	1.28	4.35	0.29	3.1	2.3
EF19-20.17	0.29	0.25	4	6.7	0.52	0.32
EF19-20.18	0.116	0.085	0.73	0.42	0.7	0.38
EF19-20.19	0.159	0.052	5.52	0.41	1.05	0.11
EF19-20.20	0.12	0.17	2.7	3.4	0.08	0.11
EF19-20.21	0.078	0.059	4.97	0.32	1.35	0.16
EF19-20.22	0.2	0.12	2.3	1.7	1.1	1.1
EF19-20.23	10.6	6	4.1	1.4	38	27
EF19-20.24	8.5	2	8.3	1.7	5.7	2.8
EF19-20.25	0.087	0.031	0.8	0.13	0.75	0.32

Spot #	Si (cps)	Std. Dev (2σ)	S (cps)	Std. Dev (2σ)	Se (cps)	Std. Dev (2σ)	Te (cps)	Std. Dev (2σ)	Hg (cps)	Std. Dev (2σ)
EF19-24										
EF19-24.01	3.75E+07	810000	134100	5000	21	19	28	18	6480	460
EF19-24.02	3.56E+07	1.10E+06	119200	4800	38	29	7.1	8	2540	450
EF19-24.03	4.13E+07	640000	174100	2800	39	26	2.4	4.8	520	360
EF19-24.04	3.11E+07	450000	70000	2800	21	21	2.4	4.8	350	400
EF19-24.05	3.51E+07	670000	102700	3900	30	24	0	1	-1360	400
EF19-24.06	3.79E+07	420000	94900	3100	55	29	43	47	3650	410
EF19-24.07	3.89E+07	650000	92300	3000	48	28	17	15	51700	3200
EF19-24.08	3.24E+07	820000	68200	3800	29	25	9.5	9.2	1290	420
EF19-24.09	2.79E+07	520000	68400	3500	25	24	0	1	2250	420
EF19-24.10	2.63E+07	820000	47700	3500	24	21	0	1	6040	590
EF19-24.11	2.80E+07	970000	45300	3300	-4	13	4.8	6.7	850	390
EF19-24.12	2.39E+07	830000	45700	2900	-12	12	0	1	1790	450
EF19-24.13	2.90E+07	720000	61700	3000	33	18	7.1	8	3070	500
EF19-24.14	2.11E+07	550000	35700	2300	37	23	0	1	4660	480

Spot #	Si (cps)	Std. Dev (2σ)	S (cps)	Std. Dev (2σ)	Se (cps)	Std. Dev (2σ)	Te (cps)	Std. Dev (2σ)	Hg (cps)	Std. Dev (2σ)
EF19-24.15	2.32E+07	820000	45900	3100	34	23	0	1	4580	460
EF19-24.16	2.78E+07	740000	58100	3200	13	19	0	1	1030	380
EF19-24.17	2.68E+07	900000	60800	2500	26	22	0	1	1130	420
EF19-24.18	2.97E+07	1.30E+06	61200	3800	33	25	2.4	4.8	890	350
EF19-24.19	2.92E+07	710000	64100	2900	47	24	0	1	750	420
EF19-24.20	2.96E+07	1.10E+06	60700	2700	37	22	0	1	-2290	370
EF19-24.21	2.79E+07	940000	72800	4700	52	31	12	10	1830	420
EF19-24.22	3.24E+07	690000	89600	3500	22	24	19	12	960	430
EF19-24.23	3.11E+07	1.10E+06	77000	3800	43	24	10	12	160	450
EF19-24.24	2.70E+07	990000	50500	2600	50	30	4.8	6.7	510	400
EF19-24.25	3.19E+07	710000	80100	4500	31	19	31	53	1380	500
EF19-24.26	3.47E+07	1.00E+06	73300	3900	24	18	0	1	1550	390
EF19-24.27	2.37E+07	820000	38300	2400	36	21	0	1	480	340
EF19-24.28	3.12E+07	980000	74700	4100	35	19	0	1	650	340
EF19-24.29	3.15E+07	370000	69300	3100	32	20	0	1	740	280

Spot #	Na (ppm)	Std. Dev (2σ)	Al (ppm)	Std. Dev (2σ)	Cl (ppm)	Std. Dev (2σ)	K (ppm)	Std. Dev (2σ)	Ti (ppm)	Std. Dev (2σ)
EF19-24.01	3520	120	13300	800	947	52	815	30	57.6	4.6
EF19-24.02	2820	190	63400	3600	1049	43	985	35	350	220
EF19-24.03	1250	40	5180	390	923	55	804	21	480	100
EF19-24.04	660	100	4100	230	972	56	703	16	42.6	7.7
EF19-24.05	2060	75	7390	150	903	57	635	17	142	53
EF19-24.06	1580	350	9660	340	867	57	2006	63	356	52
EF19-24.07	2440	170	7390	290	905	44	1022	35	42.2	2.8
EF19-24.08	1070	250	5840	160	985	50	1143	98	480	190
EF19-24.09	1150	110	30550	640	951	57	3523	71	151	19
EF19-24.10	423	23	10200	1400	891	70	877	35	810	490
EF19-24.11	701	25	6300	130	975	65	979	41	30.5	4.1
EF19-24.12	603.1	9.9	15370	330	1055	77	1479	33	27.3	3
EF19-24.13	884	36	5570	170	927	56	1133	28	48.9	4.6
EF19-24.14	215	17	24220	730	907	94	206.6	7.7	34.8	2.8

Spot #	Na (ppm)	Std. Dev (2σ)	Al (ppm)	Std. Dev (2σ)	Cl (ppm)	Std. Dev (2σ)	K (ppm)	Std. Dev (2σ)	Ti (ppm)	Std. Dev (2σ)
EF19-24.15	943	16	18910	430	976	71	1551	33	299	63
EF19-24.16	753	31	4718	40	1043	57	1023	13	27.1	3
EF19-24.17	883	31	5845	55	975	65	1164	16	30.9	2.6
EF19-24.18	946	19	6317	85	951	45	1547	34	56	27
EF19-24.19	860	13	5080	210	901	64	1109	18	26.2	1.9
EF19-24.20	966	20	14360	370	931	58	2463	78	107	34
EF19-24.21	1070	130	5090	290	997	58	1283	13	82	27
EF19-24.22	1550	240	3520	310	884	58	1136	29	28.4	2.6
EF19-24.23	--	--	--	--	819	56	1007	73	308	67
EF19-24.24	810	110	4530	190	933	63	1077	35	36.9	7.5
EF19-24.25	1230	180	5890	120	912	66	1515	33	80	13
EF19-24.26	893	24	3530	100	909	62	896	15	26	2.8
EF19-24.27	411	24	41000	1600	994	65	768	56	42.1	4.6
EF19-24.28	1292	26	6950	95	915	62	1757	39	70	16
EF19-24.29	1299	24	7033	79	993	54	1684	25	104	14

Spot #	Ti (ppm)	Std. Dev (2σ)	Fe (ppm)	Std. Dev (2σ)	Ni (ppm)	Std. Dev (2σ)	Cu (ppm)	Std. Dev (2σ)	Zn (ppm)	Std. Dev (2σ)
EF19-24.01	6.8	0.27	1745	47	5.59	0.73	51.4	1.8	280.5	7.7
EF19-24.02	34	21	1630	250	3.63	0.62	25.1	1	148.4	7.1
EF19-24.03	48.1	9.7	3920	570	2.72	0.41	16.61	0.96	34.3	3.2
EF19-24.04	2.22	0.56	26.9	5	0.89	0.38	2.09	0.32	6.1	0.73
EF19-24.05	11.1	3.6	847	22	2.43	0.48	22.37	0.89	36.1	2.9
EF19-24.06	35.2	5.1	194	15	3.9	1.1	9.86	0.81	10.6	1.3
EF19-24.07	3.46	0.43	399	48	2.35	0.45	12.1	1.6	58.5	4.5
EF19-24.08	47	18	527	98	2.52	0.52	11.2	1.3	5.84	0.82
EF19-24.09	13.6	1.7	1602	51	1.23	0.34	4.28	0.47	33.9	2.1
EF19-24.10	85	55	128	23	0.41	0.28	0.95	0.33	10.9	3.8
EF19-24.11	0.93	0.15	59.9	6.6	0.52	0.29	2.1	1.2	1.12	0.43
EF19-24.12	1.27	0.23	96.3	6.5	--	--	0.68	0.27	5.6	1.6
EF19-24.13	4.47	0.44	89.5	9.9	0.77	0.3	18.18	0.87	2.69	0.54
EF19-24.14	1.257	0.075	29	12	--	--	--	--	1.52	0.75

Spot #	Ti (ppm)	Std. Dev (2σ)	Fe (ppm)	Std. Dev (2σ)	Ni (ppm)	Std. Dev (2σ)	Cu (ppm)	Std. Dev (2σ)	Zn (ppm)	Std. Dev (2σ)
EF19-24.15	27.6	6.3	863	90	0.49	0.23	22.5	2.1	11	1.4
EF19-24.16	1.21	0.2	497	44	2.5	3.6	1.55	0.23	3.64	0.7
EF19-24.17	1.52	0.11	54.1	7	0.6	0.29	1.46	0.28	1.56	0.43
EF19-24.18	3.1	1.9	110	19	0.87	0.38	2.24	0.34	3.86	0.66
EF19-24.19	1.018	0.08	37.1	5.1	1.39	0.33	0.9	0.19	4.64	0.6
EF19-24.20	7.7	2.6	10260	420	1.25	0.33	14	0.66	46	2.9
EF19-24.21	8	2.7	302	43	1.58	0.59	7.5	1.4	8.8	2.3
EF19-24.22	28.9	3	900	270	1.85	0.38	6.5	1.4	13.5	2.6
EF19-24.23	31.5	6	392	20	--	--	--	--	9.1	1.2
EF19-24.24	2.26	0.56	1020	120	1.37	0.45	2.72	0.37	4.09	0.87
EF19-24.25	7	1.3	976	97	1.68	0.82	2.67	0.43	8	4.3
EF19-24.26	1.19	0.35	78.1	6.2	2.2	0.38	1.46	0.26	2.27	0.41
EF19-24.27	2.1	0.19	46	15	0.48	0.29	0.42	0.19	1.15	0.49
EF19-24.28	7.1	2	564	41	1.15	0.43	3.51	0.4	5.33	0.78
EF19-24.29	9.1	1.5	203	19	1.09	0.3	2.87	0.31	2.78	0.57

Spot #	As (ppm)	Std. Dev (2σ)	Pd (ppm)	Std. Dev (2σ)	Ag (ppm)	Std. Dev (2σ)	Cd (ppm)	Std. Dev (2σ)	Sn (ppm)	Std. Dev (2σ)
EF19-24.01	8.84	0.98	0.123	0.073	10.49	0.69	1.2	0.36	16	1.2
EF19-24.02	4.22	0.86	0.019	0.026	2.14	0.35	--	--	4.98	0.47
EF19-24.03	46.3	5.4	0	1	4.48	0.26	0.5	0.24	0.88	0.15
EF19-24.04	2.48	0.7	0.013	0.025	1.17	0.3	--	--	1.9	1.7
EF19-24.05	5.28	0.87	--	--	1.95	0.19	0.36	0.19	1.03	0.18
EF19-24.06	7.2	1.7	0	1	8.69	0.77	1.05	0.44	1.33	0.5
EF19-24.07	4.57	0.79	0	1	4.68	0.27	--	--	2.02	0.43
EF19-24.08	8.1	1.7	0.048	0.046	10.04	0.64	0.52	0.22	1	0.21
EF19-24.09	9.4	1.2	0.084	0.064	3	1.4	--	--	1.34	0.15
EF19-24.10	2.94	0.85	0	1	0.85	0.27	--	--	1.47	0.41
EF19-24.11	2.2	0.73	--	--	16.7	1.5	--	--	0.84	0.19
EF19-24.12	2.31	0.95	0	1	0.39	0.13	--	--	0.67	0.16
EF19-24.13	--	--	--	--	30.3	1.5	0.65	0.28	1.04	0.17
EF19-24.14	--	--	--	--	--	--	--	--	0.74	0.22

Spot #	As (ppm)	Std. Dev (2σ)	Pd (ppm)	Std. Dev (2σ)	Ag (ppm)	Std. Dev (2σ)	Cd (ppm)	Std. Dev (2σ)	Sn (ppm)	Std. Dev (2σ)
EF19-24.15	9.7	1.3	--	--	1.09	0.45	--	--	2.13	0.56
EF19-24.16	12.3	1.2	0	1	1.93	0.21	--	--	0.92	0.14
EF19-24.17	2.09	0.63	--	--	3.13	0.38	--	--	0.95	0.22
EF19-24.18	3.8	0.98	--	--	2.19	0.89	--	--	0.87	0.16
EF19-24.19	2.06	0.65	0	1	0.62	0.11	--	--	--	--
EF19-24.20	78.9	4.6	0	1	1.98	0.24	--	--	0.84	0.16
EF19-24.21	16.3	2.6	0.11	0.11	4.81	0.49	0.41	0.22	2.11	0.74
EF19-24.22	12.2	3.5	0.132	0.069	7.08	0.38	0.65	0.36	0.9	0.22
EF19-24.23	--	--	0.15	0.1	--	--	--	--	2.15	0.94
EF19-24.24	20.6	2.6	0	1	1.06	0.6	--	--	1.24	0.39
EF19-24.25	11.6	1.4	--	--	11.77	0.67	0.86	0.9	1.04	0.25
EF19-24.26	3.37	0.89	0.009	0.019	0.66	0.15	--	--	0.78	0.16
EF19-24.27	2.52	0.87	0	1	--	--	0.26	0.21	0.74	0.2
EF19-24.28	8.3	1.1	--	--	4.65	0.34	0.39	0.19	0.77	0.15
EF19-24.29	3.56	0.76	--	--	2.91	0.33	--	--	0.9	0.19

Spot #	Sb (ppm)	Std. Dev (2σ)	Pt (ppm)	Std. Dev (2σ)	Au (ppm)	Std. Dev (2σ)	Tl (ppm)	Std. Dev (2σ)	Pb (ppm)	Std. Dev (2σ)
EF19-24.01	108.3	2	--	--	0.31	0.1	0.127	0.03	1.83	0.64
EF19-24.02	85.6	2.2	--	--	--	--	0.088	0.035	1.64	0.31
EF19-24.03	110.3	5.4	--	--	--	--	0.175	0.043	0.95	0.15
EF19-24.04	63	1.6	--	--	--	--	0.043	0.02	0.102	0.047
EF19-24.05	70.1	1.3	--	--	--	--	0.121	0.03	1.69	0.28
EF19-24.06	34.3	3.6	0.018	0.02	--	--	0.332	0.087	2.18	0.67
EF19-24.07	117.1	4.7	--	--	--	--	0.071	0.033	1.04	0.5
EF19-24.08	43.8	1.5	0.021	0.024	--	--	0.149	0.063	1.5	0.55
EF19-24.09	162.8	3.1	--	--	--	--	0.242	0.05	2.79	0.32
EF19-24.10	179.1	5.3	0	1	--	--	0.092	0.033	0.308	0.097
EF19-24.11	102.7	2.7	0	1	--	--	0.094	0.036	0.93	0.16
EF19-24.12	160.2	4.1	0	1	--	--	0.09	0.041	--	--
EF19-24.13	63.6	1.3	0	1	--	--	0.165	0.045	1.82	0.24
EF19-24.14	35.5	2.3	0	1	--	--	--	--	--	--

Spot #	Sb (ppm)	Std. Dev (2σ)	Pt (ppm)	Std. Dev (2σ)	Au (ppm)	Std. Dev (2σ)	Tl (ppm)	Std. Dev (2σ)	Pb (ppm)	Std. Dev (2σ)
EF19-24.15	127.2	2.5	0	1	--	--	0.159	0.07	1.14	0.16
EF19-24.16	68.4	1.5	0	1	--	--	--	--	0.281	0.092
EF19-24.17	213.1	3.3	--	--	--	--	0.205	0.056	0.139	0.051
EF19-24.18	81.2	1.7	--	--	--	--	0.093	0.032	0.151	0.053
EF19-24.19	105.8	2.5	--	--	--	--	--	--	0.117	0.086
EF19-24.20	110.7	3.8	--	--	--	--	0.199	0.046	0.77	0.13
EF19-24.21	60.8	1.9	--	--	--	--	0.42	0.12	0.59	0.26
EF19-24.22	51.3	6.4	0	1	--	--	0.103	0.04	3.1	2.2
EF19-24.23	88.7	1.7	--	--	--	--	--	--	--	--
EF19-24.24	67	2.5	0	1	--	--	0.081	0.03	0.37	0.15
EF19-24.25	63.2	1.6	--	--	--	--	0.38	0.14	1.9	1.3
EF19-24.26	61.9	1.6	--	--	--	--	0.092	0.052	0.32	0.31
EF19-24.27	27.5	1.1	--	--	--	--	0.076	0.034	--	--
EF19-24.28	80.4	1.7	0	1	--	--	0.232	0.052	0.224	0.072
EF19-24.29	105.9	2.7	--	--	--	--	0.161	0.037	0.327	0.089

Spot #	Bi (ppm)	Std. Dev (2σ)	Th (ppm)	Std. Dev (2σ)	U (ppm)	Std. Dev (2σ)
EF19-24.01	0.08	0.019	2.53	0.29	1.46	0.21
EF19-24.02	0.238	0.061	2.63	0.39	1.07	0.19
EF19-24.03	0.082	0.017	0.86	0.11	0.507	0.063
EF19-24.04	0.078	0.071	0.141	0.049	0.124	0.043
EF19-24.05	0.06	0.023	1.28	0.11	0.72	0.11
EF19-24.06	0.7	0.42	1.16	0.16	0.99	0.44
EF19-24.07	0.24	0.23	0.69	0.19	0.91	0.54
EF19-24.08	0.24	0.24	0.87	0.25	0.78	0.54
EF19-24.09	0.121	0.053	3.69	0.23	1.35	0.32
EF19-24.10	0.04	0.022	0.169	0.074	1.7	2.9
EF19-24.11	0.079	0.039	0.03	0.019	0.034	0.018
EF19-24.12	--	--	0.91	0.94	0.279	0.044
EF19-24.13	--	--	0.197	0.057	0.18	0.1
EF19-24.14	0.08	0.12	3.2	3.7	0.0019	0.0037

Spot #	Bi (ppm)	Std. Dev (2σ)	Th (ppm)	Std. Dev (2σ)	U (ppm)	Std. Dev (2σ)
EF19-24.15	0.044	0.019	3.9	1.3	1.67	0.61
EF19-24.16	0.064	0.046	0.044	0.026	0.12	0.12
EF19-24.17	--	--	0.063	0.04	0.026	0.015
EF19-24.18	0.045	0.042	0.076	0.021	0.092	0.059
EF19-24.19	--	--	0.022	0.011	0.107	0.079
EF19-24.20	0.071	0.028	0.142	0.034	0.249	0.036
EF19-24.21	0.19	0.14	0.44	0.26	0.47	0.38
EF19-24.22	0.18	0.1	0.37	0.17	1.2	1
EF19-24.23	--	--	--	--	--	--
EF19-24.24	0.05	0.037	0.14	0.16	0.11	0.13
EF19-24.25	0.19	0.14	0.214	0.049	0.48	0.33
EF19-24.26	0.063	0.023	0.14	0.045	0.163	0.069
EF19-24.27	0.035	0.021	3.7	5.7	0.036	0.05
EF19-24.28	0.18	0.3	0.109	0.024	0.26	0.38
EF19-24.29	--	--	0.21	0.12	0.086	0.028

Spot #	Si (cps)	Std. Dev (2σ)	S (cps)	Std. Dev (2σ)	Se (cps)	Std. Dev (2σ)	Te (cps)	Std. Dev (2σ)	Hg (cps)	Std. Dev (2σ)
EF19-25										
EF19-25.01	4.18E+07	1.00E+06	77500	3500	27	20	0	1	2450	380
EF19-25.02	3.74E+07	690000	59400	3100	38	18	0	1	3540	750
EF19-25.03	3.82E+07	890000	62800	2700	33	21	0	1	1140	360
EF19-25.04	4.03E+07	990000	54800	3000	54	27	0	1	2240	480
EF19-25.05	3.79E+07	520000	55200	2800	35	28	0	1	120	380
EF19-25.06	3.90E+07	520000	67700	3700	28	24	0	1	-800	420
EF19-25.07	3.01E+07	630000	42300	4000	34	30	10	11	1170	390
EF19-25.08	2.63E+07	1.10E+06	31000	2600	26	22	0	1	150	360
EF19-25.09	2.66E+07	830000	43100	2800	25	25	4.8	6.7	1300	410
EF19-25.10	3.01E+07	680000	51300	2900	15	18	0	1	1450	490
EF19-25.11	3.15E+07	640000	104600	3000	960	100	14	11	12480	720
EF19-25.12	3.53E+07	410000	70000	14000	128	43	18	16	9300	1400
EF19-25.13	2.10E+07	1.30E+06	349000	61000	45	26	43	26	6800	1000
EF19-25.14	3.67E+07	1.00E+06	63900	3200	20	22	11.6	9.9	14200	4400
EF19-25.15	2.35E+07	860000	51200	3300	26	20	0	1	3670	480

Spot #	Si (cps)	Std. Dev (2σ)	S (cps)	Std. Dev (2σ)	Se (cps)	Std. Dev (2σ)	Te (cps)	Std. Dev (2σ)	Hg (cps)	Std. Dev (2σ)
EF19-25.16	3.35E+07	990000	64900	3000	67	28	9.8	9.4	11600	2800
EF19-25.17	3.48E+07	600000	74800	3200	141	37	0	1	7480	640
EF19-25.18	3.64E+07	650000	90300	6300	1800	890	0	1	247000	85000
EF19-25.19	2.50E+07	710000	42700	2700	82	26	0	1	48100	3900
EF19-25.20	3.42E+07	920000	71200	3100	59	33	0	1	31400	2300
EF19-25.21	1.93E+07	450000	159000	40000	20	26	0	1	800	530
EF19-25.22	3.34E+07	1.40E+06	78000	5800	409	92	14	11	43200	9100
EF19-25.23	3.05E+07	830000	98200	3700	2970	290	52	27	65000	6200
EF19-25.24	3.26E+07	930000	50900	2800	20	30	0	1	2410	430
EF19-25.25	2.64E+07	570000	45100	2600	21	29	0	1	2050	420
EF19-25.26	2.40E+07	860000	45300	2900	12	19	0	1	3150	480
EF19-25.27	3.51E+07	1.20E+06	66200	3700	15	20	0	1	770	330
EF19-25.28	2.73E+07	1.20E+06	49300	3000	15	20	0	1	780	370
EF19-25.29	3.19E+07	1.20E+06	65800	3300	25	19	7	11	1450	310
EF19-25.30	1.69E+07	1.70E+06	1.53E+06	72000	165	40	174	37	5010	490
EF19-25.31	3.08E+07	1.20E+06	20400	3600	29	25	0	1	-50	380

Spot #	Na (ppm)	Std. Dev (2σ)	Al (ppm)	Std. Dev (2σ)	Cl (ppm)	Std. Dev (2σ)	K (ppm)	Std. Dev (2σ)	Ti (ppm)	Std. Dev (2σ)
EF19-25.01	961	14	1650	170	825	45	659.5	9.1	51.4	3.2
EF19-25.02	1790	62	3950	690	890	52	1303	56	80	4.4
EF19-25.03	1040	35	3300	1000	802	47	619	20	49.2	3.6
EF19-25.04	1281	32	4080	110	779	38	1468	47	106	16
EF19-25.05	1776	37	6156	56	867	46	2460	50	47.2	5.9
EF19-25.06	1843	41	5909	64	796	51	2657	43	48.7	3.2
EF19-25.07	3980	150	25150	480	937	60	7364	91	46.9	3.8
EF19-25.08	2190	350	15070	320	975	82	3783	86	47.4	3.3
EF19-25.09	817	61	9120	370	864	62	1377	79	32.8	2.7
EF19-25.10	2520	100	19400	580	959	53	5110	240	60.3	7.1
EF19-25.11	1444	42	9970	140	1033	52	1520	100	31630	760
EF19-25.12	1940	120	9110	180	811	43	2699	44	2220	180
EF19-25.13	36500	2000	--	--	1240	100	5090	320	390	30
EF19-25.14	2070	170	36600	7600	802	50	2490	120	77.5	6.3
EF19-25.15	784	86	10500	1400	990	75	1225	92	70.6	6.5

Spot #	Na (ppm)	Std. Dev (2σ)	Al (ppm)	Std. Dev (2σ)	Cl (ppm)	Std. Dev (2σ)	K (ppm)	Std. Dev (2σ)	Ti (ppm)	Std. Dev (2σ)
EF19-25.16	2468	79	15760	640	836	53	4000	70	57.2	3.8
EF19-25.17	2080	56	9650	270	881	61	3052	66	1091	54
EF19-25.18	2183	82	12500	300	856	50	3155	85	16600	650
EF19-25.19	1179	70	12310	460	924	78	1890	130	253	37
EF19-25.20	1706	67	7020	230	797	63	1879	83	200	35
EF19-25.21	2860	970	40000	13000	1084	83	2840	770	199	78
EF19-25.22	2560	230	15880	470	944	65	3540	160	61.8	5.3
EF19-25.23	2520	160	24600	2000	1044	62	3480	280	41600	1500
EF19-25.24	3608	83	29330	580	948	56	7047	99	71.4	5.2
EF19-25.25	1121	52	12280	740	1066	84	1791	81	42	3.8
EF19-25.26	884	77	12640	920	1001	86	1400	140	33.7	2.9
EF19-25.27	3950	130	25320	540	911	47	6300	150	50.9	4
EF19-25.28	1144	55	4250	110	943	73	1367	46	85.7	6.5
EF19-25.29	870	44	1527	92	849	65	621	16	77.7	4.9
EF19-25.30	121000	11000	--	--	3280	460	14100	1200	1870	260
EF19-25.31	3568	66	25900	1700	877	65	5247	92	51.6	4.1

Spot #	Ti (ppm)	Std. Dev (2σ)	Fe (ppm)	Std. Dev (2σ)	Ni (ppm)	Std. Dev (2σ)	Cu (ppm)	Std. Dev (2σ)	Zn (ppm)	Std. Dev (2σ)
EF19-25.01	3.54	0.13	318	10	1.62	0.4	28.6	1.2	96	13
EF19-25.02	6.06	0.26	220	22	2.03	0.33	55	2.4	12.2	3.8
EF19-25.03	3.044	0.088	375	11	1.36	0.39	36.6	1.5	19.5	3.5
EF19-25.04	8.3	1.5	168	23	1.08	0.29	2.1	0.26	7.5	3.1
EF19-25.05	2.39	0.21	188.1	8.9	1.42	0.33	3.21	0.28	27.1	5.8
EF19-25.06	2.92	0.15	230	11	2.36	0.41	1.08	0.21	46.9	9
EF19-25.07	2.8	0.13	414	15	1.35	0.58	2.12	0.38	6.6	1.9
EF19-25.08	2.545	0.071	122	12	0.64	0.26	0.53	0.21	1.48	0.47
EF19-25.09	1.37	0.12	687	81	--	--		--	**--** 11.4	1.4
EF19-25.10	3.82	0.35	1840	150	1.83	0.66	7.96	0.62	5.9	1.2
EF19-25.11	3486	79	228600	3700	14.1	2	757	13	441	28
EF19-25.12	219	18	19100	1300	3.4	1.4	74.2	4.9	85.7	7.3
EF19-25.13	42.3	3	5950	620	76.5	9.4	53.2	7.1	1970	380
EF19-25.14	5.17	0.5	8300	1000	5.7	2.1	6.74	0.77	64.3	7.8
EF19-25.15	4.62	0.43	460	140	45	49	2.79	0.59	14.8	3.7

Spot #	**Ti (ppm)**	**Std. Dev (2σ)**	**Fe (ppm)**	**Std. Dev (2σ)**	**Ni (ppm)**	**Std. Dev (2σ)**	**Cu (ppm)**	**Std. Dev (2σ)**	**Zn (ppm)**	**Std. Dev (2σ)**
EF19-25.16	3.58	0.2	15800	1200	2.88	0.58	7.75	0.71	36.5	6.2
EF19-25.17	101.4	4.3	13200	960	3.5	0.48	39.3	3	106.1	8.8
EF19-25.18	1823	72	81000	15000	6.8	1.3	250	51	251	35
EF19-25.19	22.1	3.2	11600	3200	1.44	0.45	43	13	18.2	4.7
EF19-25.20	16.9	3.4	2700	460	3.1	0.52	8.1	1.6	105	11
EF19-25.21	16.3	6.9	31000	13000	66	30	121	60	141	55
EF19-25.22	4.56	0.42	22800	5000	3.6	1.2	101	20	70	11
EF19-25.23	4290	120	254000	20000	5.89	0.74	969	78	292	23
EF19-25.24	5.3	0.29	930	180	1.06	0.32	2.39	0.51	25.2	5.1
EF19-25.25	2.32	0.18	42.6	6.9	0.77	0.33	0.41	0.18	1.89	0.67
EF19-25.26	1.33	0.077	117	15	0.59	0.26	0.62	0.2	5.6	1.3
EF19-25.27	3.46	0.16	2220	210	1.66	0.42	1.63	0.41	18.8	4.6
EF19-25.28	6.15	0.34	4890	230	3.4	1.9	2.37	0.48	9.5	2
EF19-25.29	5.59	0.19	322	17	6	2.5	1.96	0.47	11.2	1.6
EF19-25.30	233	34	115000	10000	301	26	1280	110	5430	640
EF19-25.31	2.92	0.16	760	130	1.2	0.35	2.89	0.38	8.9	2.1

Spot #	As (ppm)	Std. Dev (2σ)	Pd (ppm)	Std. Dev (2σ)	Ag (ppm)	Std. Dev (2σ)	Cd (ppm)	Std. Dev (2σ)	Sn (ppm)	Std. Dev (2σ)
EF19-25.01	2.89	0.48	0	1	0.325	0.095	0.25	0.17	0.72	0.14
EF19-25.02	3.61	0.76	0.029	0.033	1.46	0.28	0.27	0.2	0.88	0.15
EF19-25.03	3.57	0.66	0	1	--	--	0.28	0.16	0.91	0.16
EF19-25.04	5.15	0.82	0	1	0.219	0.095	--	--	0.73	0.13
EF19-25.05	4.17	0.61	--	--	--	--	--	--	0.78	0.15
EF19-25.06	4.31	0.72	0	1	--	--	--	--	0.64	0.12
EF19-25.07	9.6	1.6	0.059	0.05	--	--	--	--	1.14	0.25
EF19-25.08	4	1.2	0	1	0.2	0.45	0.42	0.21	0.91	0.22
EF19-25.09	8.6	1.4	0	1	--	--	--	--	--	--
EF19-25.10	17	2.1	--	--	1.02	0.45	--	--	1.31	0.31
EF19-25.11	1466	41	0.071	0.054	4.7	1.1	1.49	0.48	37.3	1.1
EF19-25.12	141.2	9.7	0.063	0.057	1.74	0.62	0.46	0.38	3.4	0.44
EF19-25.13	12.3	2.4	0	1	4.99	0.74	1.02	0.5	19.9	2.4
EF19-25.14	52.3	6.8	0	1	0.48	0.19	--	--	1.27	0.19
EF19-25.15	6.8	1.5	0	1	7.4	3.2	--	--	1.34	0.3

Spot #	As (ppm)	Std. Dev (2σ)	Pd (ppm)	Std. Dev (2σ)	Ag (ppm)	Std. Dev (2σ)	Cd (ppm)	Std. Dev (2σ)	Sn (ppm)	Std. Dev (2σ)
EF19-25.16	123.5	8.3	--	--	--	--	0.81	0.32	0.71	0.15
EF19-25.17	124	12	0.044	0.042	0.7	0.21	0.89	0.35	1.32	0.22
EF19-25.18	880	190	0.25	0.1	1.7	0.34	2.03	0.98	13.55	0.72
EF19-25.19	121	32	--	--	0.38	0.17	0.38	0.2	1.08	0.19
EF19-25.20	30.6	7.3	0	1	0.31	0.1	0.22	0.17	0.81	0.13
EF19-25.21	24.6	8.1	--	--	3.9	1.6			9.1	4.1
EF19-25.22	399	77	0.033	0.037	1.65	0.26	0.7	0.5	1.52	0.47
EF19-25.23	3000	240	1.32	0.24	8.6	1.2	1.89	0.42	42.7	1.9
EF19-25.24	9.8	1.4	--	--	0.19	0.1	0.37	0.21	0.78	0.13
EF19-25.25	2.87	0.94	0	1	--	--	--	--	0.77	0.19
EF19-25.26	3.95	0.91	0	1	--	--	--	--	0.79	0.22
EF19-25.27	16.5	1.9	0	1	--	--	0.39	0.17	0.85	0.18
EF19-25.28	32.3	2.2	0	1	0.25	0.11	--	--	0.67	0.18
EF19-25.29	4.89	0.95	0	1	1.23	0.2	0.25	0.17	0.84	0.23
EF19-25.30	77.4	6.8	0.072	0.069	54.6	7.4	2.48	0.86	153	19
EF19-25.31	6.7	1.2	0	1	--	--	0.19	0.13	0.82	0.15

Spot #	Sb (ppm)	Std. Dev (2σ)	Pt (ppm)	Std. Dev (2σ)	Au (ppm)	Std. Dev (2σ)	Tl (ppm)	Std. Dev (2σ)	Pb (ppm)	Std. Dev (2σ)
EF19-25.01	662	11	--	--	--	--	0.03	0.015	2.73	0.2
EF19-25.02	292.3	4.7	0.021	0.021	0.24	0.14	0.071	0.022	2.21	0.28
EF19-25.03	420.9	7.8	--	--	--	--	--	--	2.93	0.26
EF19-25.04	234.2	4.6	--	--	--	--	--	--	0.79	0.17
EF19-25.05	143.8	4.7	0	1	--	--	0.056	0.025	0.7	0.11
EF19-25.06	131.2	3.8	0	1	--	--	0.051	0.022	0.52	0.14
EF19-25.07	63.4	2.2	--	--	--	--	0.191	0.065	0.56	0.19
EF19-25.08	93.3	1.9	--	--	--	--	0.096	0.037	0.09	0.062
EF19-25.09	46.6	1.3	--	--	--	--	--	--	0.55	0.19
EF19-25.10	44.2	1.3	--	--	--	--	0.108	0.034	0.62	0.14
EF19-25.11	1473	36	0.035	0.03	--	--	0.137	0.038	138.2	5
EF19-25.12	184	10	--	--	--	--	0.068	0.038	12.4	2.7
EF19-25.13	62.8	2	--	--	--	--	0.19	0.057	8.6	1.7
EF19-25.14	153	16	--	--	--	--	0.041	0.023	9.4	1.6
EF19-25.15	60.7	2.4	--	--	--	--	0.082	0.039	0.36	0.14

Spot #	Sb (ppm)	Std. Dev (2σ)	Pt (ppm)	Std. Dev (2σ)	Au (ppm)	Std. Dev (2σ)	Tl (ppm)	Std. Dev (2σ)	Pb (ppm)	Std. Dev (2σ)
EF19-25.16	222	13	0	1	--	--	0.07	0.04	21.2	2.1
EF19-25.17	125.3	3.7	--	--	--	--	0.084	0.031	5.96	0.37
EF19-25.18	556	52	--	--	--	--	0.14	0.032	84.2	6.3
EF19-25.19	120	12	--	--	0.45	0.21	0.086	0.059	4.4	1.2
EF19-25.20	72.7	2.1	0	1	--	--	0.04	0.022	1.8	0.36
EF19-25.21	45.5	3.1	--	--	0.64	0.24	0.126	0.051	11.6	1.6
EF19-25.22	120	12	--	--	--	--	0.2	0.098	8	2.1
EF19-25.23	1250	75	--	--	0.53	0.16	0.197	0.05	221.8	8.8
EF19-25.24	58.1	1.5	0	1	--	--	0.171	0.041	0.47	0.11
EF19-25.25	80.6	2.5	0	1	--	--	--	--	0.106	0.059
EF19-25.26	53.7	2	0	1	--	--	--	--	1.1	0.37
EF19-25.27	96.7	2.2	--	--	--	--	0.155	0.034	1.51	0.22
EF19-25.28	230.5	5.9	--	--	--	--	--	--	3.3	0.34
EF19-25.29	460.1	8.9	0	1	--	--	--	--	0.36	0.19
EF19-25.30	74.5	4.1	--	--	0.59	0.36	0.8	0.14	46.1	4.9
EF19-25.31	89.6	1.7	--	--	--	--	0.106	0.02	0.27	0.1

Spot #	Bi (ppm)	Std. Dev (2σ)	Th (ppm)	Std. Dev (2σ)	U (ppm)	Std. Dev (2σ)
EF19-25.01	0.083	0.032	1.75	0.12	3.31	0.1
EF19-25.02	0.052	0.025	4.75	0.14	3.68	0.18
EF19-25.03	0.085	0.089	0.529	0.087	3.44	0.15
EF19-25.04	0.059	0.045	0.621	0.095	2.07	0.12
EF19-25.05	0.133	0.067	0.078	0.027	1.84	0.21
EF19-25.06	0.17	0.14	0.073	0.028	1.344	0.089
EF19-25.07	0.43	0.44	0.21	0.15	0.485	0.081
EF19-25.08	0.05	0.027	0.3	0.44	0.214	0.038
EF19-25.09	--	--	1.6	2.2	0.373	0.099
EF19-25.10	0.111	0.07	0.155	0.033	0.443	0.048
EF19-25.11	9.62	0.43	115.2	2.1	86.5	1.7
EF19-25.12	0.99	0.15	8.35	0.77	10.11	0.57
EF19-25.13	13.7	3.6	0.94	0.1	2.02	0.28
EF19-25.14	0.21	0.053	0.171	0.029	0.98	0.18
EF19-25.15	0.095	0.059	59	68	0.154	0.045

Spot #	Bi (ppm)	Std. Dev (2σ)	Th (ppm)	Std. Dev (2σ)	U (ppm)	Std. Dev (2σ)
EF19-25.16	0.477	0.072	0.164	0.036	0.976	0.095
EF19-25.17	0.376	0.052	8.24	0.45	7.12	0.25
EF19-25.18	2.36	0.24	55.4	2.3	50.6	1.5
EF19-25.19	0.261	0.067	0.69	0.14	2.72	0.71
EF19-25.20	0.075	0.023	0.421	0.091	2.03	0.21
EF19-25.21	0.27	0.11	0.53	0.15	0.81	0.21
EF19-25.22	0.67	0.18	1.64	0.34	6.4	1
EF19-25.23	15.27	0.86	159.1	5.8	154	5.4
EF19-25.24	0.079	0.044	0.084	0.025	0.52	0.068
EF19-25.25	--	--	13	22	0.097	0.025
EF19-25.26	0.04	0.026	0.23	0.38	0.085	0.023
EF19-25.27	0.055	0.025	0.27	0.23	0.665	0.067
EF19-25.28	0.26	0.39	0.161	0.036	1.147	0.092
EF19-25.29	0.053	0.02	0.152	0.03	0.907	0.073
EF19-25.30	94	17	4.63	0.8	16	2.4
EF19-25.31	0.044	0.023	0.056	0.016	0.442	0.054